

# Faculty of Engineering of the University of Porto



June 19, 2017

Faculty of Engineering of the University of Porto



# Mechanical Characterization of the Human Atria Based on Patient-Specific FEM Models

Boris Nii Ako Sowah

Dissertation carried out under  
Masters in Biomedical Engineering

Supervisor: Prof. João Manuel R. S. Tavares

Co-supervisor: Dr Marco Lages Parente

June 19, 2017

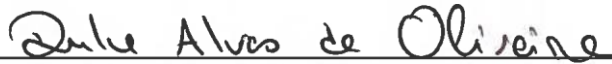
A Dissertação intitulada

“Mechanical Characterization of the Human Atria Based on Patient-specific FEM Models”

foi aprovada em provas realizadas em 27-06-2017

o júri

  
Presidente Prof. Doutor Miguel Fernando Paiva Velhote Correia  
Professor Auxiliar do Departamento de Engenharia Eletrotécnica e de Computadores da FEUP  
- U.Porto

  
Doutora Dulce Alves de Oliveira  
Investigadora do Instituto de Ciência e Inovação em Engenharia Mecânica e Engenharia Industrial da U. Porto

  
Prof. Doutor João Manuel Ribeiro da Silva Tavares  
Professor Associado c/ Agregação do Departamento de Engenharia Mecânica da FEUP - U. Porto

O autor declara que a presente dissertação (ou relatório de projeto) é da sua exclusiva autoria e foi escrita sem qualquer apoio externo não explicitamente autorizado. Os resultados, ideias, parágrafos, ou outros extratos tomados de ou inspirados em trabalhos de outros autores, e demais referências bibliográficas usadas, são corretamente citados.

  
Autor - Boris Nii Ako Sowah



## Summary

The left atrium (LA) of the heart serves vital roles that exerts profound effect on the left ventricle (LV) filling and subsequently the overall performance of the cardiovascular process. There are common diseases such as atrial fibrillation (AF) and atrial stunning (AS) that alters the effective functioning of the atria. In view of this, access to the LA is very vital to perform several minimally invasive cardiac interventions of the left heart to rectify these abnormalities. Transseptal puncture technique (TSP) is the commonest minimally invasive technique that involves the puncturing of the atrial septum by the use of a catheter inserted in the right atrium (RA) through the venous system under a bi-dimensional fluoroscopic guidance. There are associated complications; possibility of multiple puncturing and procedural failures using this technique even though it has been in existence for several years and the success rate basically depends on the experience of the physician.

To resolve these complications, the exact location at which the septum requires to be traversed needs to be simulated. The objective of this project is to develop technologies to help the physicians when performing TSP technique using the finite element method (FEM) software (Abaqus) based on FEM models. There will be a complete study of the mechanical properties of the human atrium, specifically the interatrial septal wall as well as the simulation of the needle insertion into soft tissues to aid in the effective optimization of the TSP technique.



# Abstract

*Atrial fibrillation (AF) is the most common cardiac arrhythmia in the world affecting more than 9 million of person per year in Europe. AF is described by a dysfunction of the electric conduction system of the cardiac atria. The traditional treatment requires an ablation of the dysfunctional tissues at the atria using a minimally invasive cardiac intervention, called radio-frequency ablation therapy. The success of this procedure is dependent of the experience of the operator, which could be sub-optimal in abnormal anatomy situations.*

*During this project, I intend to develop FEM models of the atrium to simulate the needle insertion procedure. Secondly, a strategy will be developed and used to generate the meshes for the FEM models and needle designed for this dissertation. The Coupled Eulerian-Lagrangian (CEL) FEM analysis technique will be used during the simulation of the needle insertion into the developed FEM models. The mechanical properties of the tissue will be obtained from literature review and related works. Three sets of simulation results will be studied and discussed after the simulation process and the simulation results include: the needle insertion forces, the effect of varying the dimensions of the FEM model and finally the Mises stress distribution.*

*Keywords: Biomedical Engineering, Cardiovascular diseases, Coupled Eulerian-Lagrangian, Finite Element Method, Biomechanics.*





# Appreciations

All praise and honour be to the Almighty God for the gift of life, good health and also the opportunity to pursue my master's program in this noble institution. Indeed, to everything there is a season and a time to every purpose under the heaven (Ecclesiastes 3:1).

A special appreciation goes to my parents and siblings for their continues support, guidance, understanding and prayers that has brought me this far. I say a very big thank you and I pray for God's blessings in all you do in order to achieve your heart desires and aspirations.

Also, I am indebted to DREAM partnership within the Erasmus Mundus Action 2 represented by University of Porto as the coordinating institution for giving me this great privilege and opportunity to pursue my full master degree program in Portugal for a period of 22 months and also providing me with the needed financial support to successfully achieve my dreams and aspirations.

Furthermore, I am most grateful to my supervisors Prof. João Manuel R. S. Tavares and Dr. Marco Lages Parente for their guidance, patience, directions, contributions and support throughout this dissertation. I have acquired enormous wealth of knowledge while working with you and it was certainly a pleasure working with and learning from you. I say "obrigado" and I promise to make you proud by effectively implementing the acquired knowledge in all my endeavors.

I am grateful to all the lecturers and technicians I encountered during my brief but lovely period here. I acknowledge the efforts you made to teach in English as well as getting me the course documents in English.

Finally, a very big thank you to all my colleagues of the Biomedical Engineering Master program. The journey has been relatively long, interesting and bumpy but I could not ask for anything else because of your understanding, assistance, support and friendship I have been able to make it this far. To all my friends I say thank you for being there for me and helping me through this journey.



*I returned, and saw under the sun, that the race is not to the swift, nor the battle to the strong, neither yet bread to the wise, nor yet riches to men of understanding, nor yet favour to men of skill; but time and chance happeneth to them all (Ecclesiastes 9:11 KJV) and indeed, He hath made every thing beautiful in his time (Ecclesiastes 3:11a KJV).*



# Contents

Chapter 1 .....	1
Introduction.....	1
1.1 - Motivation.....	2
1.2 - Objectives.....	3
1.3 - Document structure .....	3
1.4 - Principal contributions.....	4
Chapter 2.....	7
Fundamentals.....	7
2.1 - Structure of the heart .....	7
2.2 - Physiological functions of the heart.....	9
2.3 - Physiological structure of the atrium .....	9
2.4 - Common diseases associated with the heart .....	11
2.5 - Existing treatment techniques of atrial associated diseases.....	12
2.6 - Accessing the left atrium.....	13
2.7 - Transseptal puncture technique .....	14
2.8 - Finite element method review .....	15
2.9 - Strong and weak form in one dimension .....	16
2.10 - Shape functions and Gauss integration .....	20
2.11 - Discretization of the equilibrium equation into a FEM .....	24
2.12 - Coupled Eulerian-Lagrangian (CEL) method .....	25
Chapter 3.....	29
Biomechanical Simulation and Related Works .....	29
3.1 - Biomechanical simulation .....	29
3.2 - Patient-specific anatomical cardiac models .....	30
3.3 - Image-fusion and catheter tracking techniques.....	34
3.4 - Simulation of the atrium .....	38
3.5 - Simulation of needle insertion .....	43
Chapter 4.....	47
Simulation Methodology .....	47
4.1 - Mechanical properties of the human atria .....	47
4.2 - Needle geometry and modelling .....	53

4.3 - Tissue geometry and modelling .....	55
4.4 - Simulation of needle insertion .....	56
Chapter 5.....	61
Simulation Results and Discussion .....	61
5.1 - Results of needle insertion forces .....	61
5.2 - Results of varying the size of the patch .....	65
5.3 - Results of the von Mises stress distribution .....	71
5.4 - Discussion .....	78
5.5 - Limitations .....	82
Chapter 6.....	83
Conclusion and Future Perspectives .....	83
6.1 - Conclusions .....	83
6.2 - Future works.....	84
References .....	85

# List of figures

Figure 2.1 - Cross-section of the heart showing the chambers and direction of flow of blood .... 8

Figure 2.2 - Ventricular pressure-volume relationship ..... 10

Figure 2.3 - Heart anatomy showing the atria ..... 11

Figure 2.4 - Schematic of transaortic route (a) and transseptal puncture technique (b) (adapted by Pedro André Gonçalves Morais et al) ..... 13

Figure 2.5 - Pressure tracing from transseptal needle during TSP ..... 15

Figure 2.6 - TSP technique. (a) A dilator and sheath placed into the SVC using the guidewire; (b) A needle is inserted into the dilator until (c) the SVC; the needle is pulled down and two movements are detected: (d) entrance into the RA and (e) entrance into the FO; (f) after the FO identification, the puncture is performed ..... 15

Figure 2.7 - Applications in predictive medicine: (a) Overlying mesh of a hand model near the wound. (b) Cross-section of a heart model. (c) Portion of hip replacement showing the physical object and the FEM model ..... 16

Figure 2.8 - A one-dimensional analysis of an axially loaded elastic bar ..... 17

Figure 2.9 - A one-dimensional element with m nodes ..... 21

Figure 2.10 - Mapping of the one-dimensional domain from the parent domain  $[-1,1]$  to the physical domain  $[a,b]$  ..... 23

Figure 2.11 - Finite element in 2D with domain  $\Omega$  and boundary  $\Gamma$  ..... 24

Figure 2.12 - Lagrangian mesh ..... 26

Figure 2.13 - Eulerian mesh.....	26
Figure 2.14 - Lagrangian description (a) against Eulerian description (b) .....	27
Figure 3.1 - Overview of the proposed technique by Zheng <i>et al.</i> .....	32
Figure 3.2 - Schematic used by atlas-based approaches to segment MR images. It uses an affine registration (1) to roughly align the unseen image with the atlas. The obtained transformations are then posteriorly used to map the label images (2) into the unseen image and generate a region-of-interest through a majority vote strategy (3). Using only this region, a non- rigid registration (4) is used to align the different datasets. The resulting deformation fields are used to transform the labels and generate the final contour (5).....	33
Figure 3.3 - Ecabert et al. methodology: a) A rough contour is initially estimated through a generalized Hough transform approach. In (b) and (c) a global and local adaptation of the model is performed, respectively. Finally, in (d) a deformable model strategy is used to refine the contour .....	33
Figure 3.4 - (a) Calibration cage used to align ultrasound world with probe position and (b) radiopaque markers to fuse X-ray and ultrasound world .....	35
Figure 3.5 - Workflow used to align MRI or CT, X-ray and ultrasound images. Pre-procedure phase; a CT or MRI image is acquired, automatically segmented and converted to a surface model. The esophagus centreline is manually segmented. During the procedure, an ultrasound volume is first acquired and registered to X-ray space via the TEE probe. The pre-procedure surface model is then manually positioned in the X-ray view before being automatically registered via the ultrasound image. The experiments in this paper evaluate intra-procedure stage 2 .....	36
Figure 3.6 - Geometry of the LA model at a pressure of 15 mmHg. (a) The four PVs denoted as right superior PV (RSPV), right inferior PV (RIPV), left superior PV (LSPV) and left inferior PV (LIPV). (b) FEM mesh with 30,000 elements. (c) Different orientations of the model rotated in 90° .....	39
Figure 3.7 - 3D model of the human atria. (A) denotes the frontal whiles (B) depicts the views respectively .....	40
Figure 3.8 - Block structure and low-density mesh views of the various components (from “a” to “g”) as well as the mesh of the entire model (centre) .....	42
Figure 3.9 - Block diagram of needle insertion procedure .....	44



Figure 4.1 - Extra-atrial MDCT view. The right inferior ostium is denoted by the dotted lines whereas the straight arrow denotes the region of the AV groove. \* represents the sharp angulation in the vein. SA is the region where branches of separate veins have direct spatial contiguity. LI is LIPV, LS is LSPV, RI is RIPV and RS is RSPV ..... 48

Figure 4.2 - Intra-atrial views of the posterior LA and PV regions. (A) Right superior (RS), right inferior (RI), right middle (RM) vein ostia. RI' is the ostial branch of the RIPV. S and S' denotes intervenous and intravenous saddles respectively. Dotted lines denote the AV junction. (B) Left superior (LS), left inferior (LI) vein ostia, ostium of the appendage (LAA) and a section of the posterior MV leaflet. It also shows the ridge between the vein inflow region and the appendage ostium (R) as well as LI ostium represented by the dotted lines. (C) Electrograms recorded from the area in B with the corresponding number ..... 48

Figure 4.3 - An endocast from a normal heart showing the arrangement of components of the atria as observed from (A) the front, (B) the right and (C) the left ..... 51

Figure 4.4 - The generation, projection and optimization of the mesh. (a) the 16-element static spherical mesh (red) (b) projections along the fitted radius onto the surface (gray lines) (c) optimization of mesh parameters..... 52

Figure 4.5 - Optimized lancet needle geometry ..... 54

Figure 4.6 - (a) The cylindrical model of the needle. (b) The front view of the needle tube after grinding at an angle of 12.4°. (c) The side view of the needle tube after grinding at an angle of 12.4°. (d) Front view of the needle tube after the first and second lancet ..... 54

Figure 4.7 - Developed needle tip and needle for the needle simulation ..... 55

Figure 4.8 - An extruded cube representing the slice or layer of soft tissue or cardiac muscle 55

Figure 4.9 - Assembly of the soft tissue or cardiac muscle and the needle ..... 56

Figure 4.10 - The (A) Front, (B) Back, (C) Left and (D) Right views of the assembly..... 56

Figure 4.11 - The generated mesh of the soft tissue or cardiac muscle ..... 57

Figure 4.12 - The generated mesh of the needle ..... 57

Figure 4.13 - The generated mesh of the entire assembly (Tissue and needle) ..... 57

Figure 4.14 - (A) 15°, (B) 30°, (C) 45°, (D) 60° and (E) 0° angle of rotation of the needle about the Z-axis..... 58

Figure 4.15 - (A) 15°, (B) 30°, (C) 45°, (D) 60° and (E) 0° angle of rotation of the needle about the X-axis..... 59

Figure 5.1 - Graphical representation of all rotations of the needle about the Z-axis during the needle insertion into the soft tissue patch ..... 62

Figure 5.2 - Graphical representation of all rotations of the needle about the X-axis during the needle insertion into the soft tissue patch ..... 63

Figure 5.3 - Graphical representation of all rotations of the needle about the Z-axis during the needle insertion into the cardiac muscle patch..... 64

Figure 5.4 - Graphical representation of all rotations of the needle about the X-axis during the needle insertion into the cardiac muscle patch..... 65

Figure 5.5 - Graphical representation of a 30° rotation of the needle about the Z-axis during the needle insertion into the soft tissue patch for both the initial and modified dimensions of the soft tissue patch..... 66

Figure 5.6 - Graphical representation of a 30° rotation of the needle about the X-axis during the needle insertion into the soft tissue patch for both the initial and modified dimensions of the soft tissue patch..... 66

Figure 5.7 - Graphical representation of a 45° rotation of the needle about the Z-axis during the needle insertion into the soft tissue patch for both the initial and modified dimensions of the soft tissue patch ..... 67

Figure 5.8 - Graphical representation of a 45° rotation of the needle about the X-axis during the needle insertion into the soft tissue patch for both the initial and modified dimensions of the soft tissue patch ..... 67

Figure 5.9 - Graphical representation of a 0° rotation of the needle about the Z-axis during the needle insertion into the soft tissue patch for both the initial and modified dimensions of the soft tissue patch..... 68

Figure 5.10 - Graphical representation of a 30° rotation of the needle about the Z-axis during the needle insertion into the cardiac muscle for both the initial and new dimensions of the cardiac muscle patch ..... 68

Figure 5.11 - Graphical representation of a 30° rotation of the needle about the X-axis during the needle insertion into the cardiac muscle for both the initial and new dimensions of the cardiac muscle patch ..... 69

Figure 5.12 - Graphical representation of a 45° rotation of the needle about the Z-axis during the needle insertion into the cardiac muscle for both the initial and new dimensions of the cardiac muscle patch .....	69
Figure 5.13 - Graphical representation of a 45° rotation of the needle about the X-axis during the needle insertion into the cardiac muscle for both the initial and new dimensions of the cardiac muscle patch .....	70
Figure 5.14 - Graphical representation of a 0° rotation of the needle about the X-axis during the needle insertion into the cardiac muscle for both the initial and new dimensions of the cardiac muscle patch .....	70
Figure 5.15 - Mises stress distribution of the tender tissue at 15° rotation of the needle about the Z-axis during the needle insertion into the soft tissue patch.....	71
Figure 5.16 - Mises stress distribution of the soft tissue at 15° rotation of the needle about the Z-axis during the needle insertion into the soft tissue patch .....	71
Figure 5.17 - Mises stress distribution of the tender tissue at 15° rotation of the needle about the X-axis during the needle insertion into the soft tissue patch.....	72
Figure 5.18 - Mises stress distribution of the soft tissue at 15° rotation of the needle about the X-axis during the needle insertion into the soft tissue patch .....	72
Figure 5.19 - Mises stress distribution of the tender tissue at 15° rotation of the needle about the Z-axis during the needle insertion into the cardiac muscle patch.....	72
Figure 5.20 - Mises stress distribution of the cardiac muscle at 15° rotation of the needle about the Z-axis during the needle insertion into the cardiac muscle patch.....	73
Figure 5.21 - Mises stress distribution of the tender tissue at 15° rotation of the needle about the X-axis during the needle insertion into the cardiac muscle patch.....	73
Figure 5.22 - Mises stress distribution of the cardiac muscle at 15° rotation of the needle about the X-axis during the needle insertion into the cardiac muscle patch.....	73
Figure 5.23 - Mises stress distribution of the tender tissue at 45° rotation of the needle about the Z-axis during the needle insertion into the soft tissue patch.....	74
Figure 5.24 - Mises stress distribution of the soft tissue at 45° rotation of the needle about the Z-axis during the needle insertion into the soft tissue patch .....	74

Figure 5.25 - Mises stress distribution of the tender tissue at 45° rotation of the needle about the X-axis during the needle insertion into the soft tissue patch..... 74

Figure 5.26 - Mises stress distribution of the soft tissue at 45° rotation of the needle about the X-axis during the needle insertion into the soft tissue patch ..... 75

Figure 5.27 - Mises stress distribution of the tender tissue at 45° rotation of the needle about the Z-axis during the needle insertion into the cardiac muscle patch..... 75

Figure 5.28 - Mises stress distribution of the cardiac muscle at 45° rotation of the needle about the Z-axis during the needle insertion into the cardiac muscle patch..... 75

Figure 5.29 - Mises stress distribution of the tender tissue at 45° rotation of the needle about the X-axis during the needle insertion into the cardiac muscle patch..... 76

Figure 5.30 - Mises stress distribution of the cardiac muscle at 45° rotation of the needle about the X-axis during the needle insertion into the cardiac muscle patch..... 76

Figure 5.31 - Mises stress distribution of the tender tissue at 0° rotation (perpendicular) of the needle during the needle insertion into the soft tissue patch..... 76

Figure 5.32 - Mises stress distribution of the soft tissue at 0° rotation (perpendicular) of the needle during the needle insertion into the soft tissue patch..... 77

Figure 5.33 - Mises stress distribution of the tender tissue at 0° rotation (perpendicular) of the needle during the needle insertion into the cardiac muscle patch..... 77

Figure 5.34 - Mises stress distribution of the cardiac muscle at 0° rotation (perpendicular) of the needle during the needle insertion into the cardiac muscle patch..... 77

## List of tables

Table 2.1 - Heart values and their functions .....	10
Table 4.1 - Thickness of the LA walls as measured in 26 hearts showing the median $\pm$ standard deviation in millimeters .....	50
Table 4.2 - Displacement co-ordinates for the X and Y axes for the rotation about the Z-axis.	58
Table 4.3 - Displacement co-ordinates for the X and Y axes for the rotation about the X-axis.	59



# Abbreviations and symbols

## List of abbreviations

<i>2D</i>	<i>Bi-dimensional</i>
<i>3D</i>	<i>Three-dimensional</i>
<i>AF</i>	<i>Atrial fibrillation</i>
<i>AFER</i>	<i>Atrial fibrillation induced electrical remodelling</i>
<i>AP</i>	<i>Action potential</i>
<i>APG</i>	<i>Appendage</i>
<i>AS</i>	<i>Atrial stunning</i>
<i>ASM</i>	<i>Active shape models</i>
<i>AV</i>	<i>Atrioventricular</i>
<i>AVR</i>	<i>Atrioventricular ring</i>
<i>BB</i>	<i>Bachmann's bundle</i>
<i>BEAS</i>	<i>B-spline Explicit Active Surface</i>
<i>CEL</i>	<i>Coupled Eulerian-Lagrangian</i>
<i>CHD</i>	<i>Coronary heart disease</i>
<i>CS</i>	<i>Coronary sinus</i>
<i>CT</i>	<i>Computer tomography</i>
<i>CTA</i>	<i>Computer tomography angiography</i>
<i>CVD</i>	<i>Cardiovascular disease</i>
<i>ECG</i>	<i>Electrocardiogram</i>
<i>ECM</i>	<i>Extracellular matrix</i>
<i>EGM</i>	<i>Electrogram</i>
<i>EM</i>	<i>Electromagnetic</i>
<i>EVF</i>	<i>Eulerian volume fraction</i>
<i>FEA</i>	<i>Finite element analysis</i>
<i>FEM</i>	<i>Finite element method</i>
<i>FO</i>	<i>Fossa ovalis</i>
<i>FOV</i>	<i>Field-of-view</i>
<i>GPU</i>	<i>Graphics processing unit</i>
<i>IAS</i>	<i>Interatrial septal wall</i>

ICP	<i>Iterative closest point</i>
ICV	<i>Inferior caval vein</i>
IVC	<i>Inferior vena cava</i>
LA	<i>Left atrium</i>
LAPG	<i>Left appendages</i>
LIPV	<i>Left inferior pulmonary vein</i>
LPV	<i>Left pulmonary vein</i>
LSPV	<i>Left superior pulmonary vein</i>
LV	<i>Left ventricle</i>
MDCT	<i>Multidetector helical computed tomography</i>
MNS	<i>Magnetic navigation system</i>
MR	<i>Magnetic resonance</i>
MRI	<i>Magnetic resonance imaging</i>
MV	<i>Mitral valve</i>
PCI	<i>Percutaneous cardiac interventions</i>
PM	<i>Pecinate muscle</i>
PV	<i>Pulmonary vein</i>
RA	<i>Right atrium</i>
RAO	<i>Right anterior oblique</i>
RAPG	<i>Right appendages</i>
RF	<i>Radiofrequency</i>
RIPV	<i>Right inferior pulmonary vein</i>
RMSE	<i>Root mean square error</i>
ROI	<i>Region of interest</i>
RPV	<i>Right pulmonary vein</i>
RSPV	<i>Right superior pulmonary vein</i>
RV	<i>Right ventricle</i>
SAV	<i>Stenotic aortic valve</i>
SCV	<i>Superior caval vein</i>
SVC	<i>Superior vena cava</i>
TA	<i>Transaortic</i>
TEE	<i>Transesophageal echocardiography</i>
TPS	<i>Thin-plate spline</i>
TSP	<i>Transseptal puncture</i>
VIC	<i>Valve interstitial cells</i>







# Chapter 1

## Introduction

The human heart is an essential organ of the human body parts that is primarily responsible for pumping blood throughout the body. The human heart is a muscular organ which has four chambers, hollow and cone-shaped situated towards the left of the midline of the thoracic cavity. It is about 14 cm long and 9 cm wide and it is approximately the size of a closed fist of a man. The atria are the upper two chambers divided by a wall-like structure called interatrial septum while the ventricles consist of the two lower chambers also divided by the interventricular septum. There are valves between each atrium and ventricle which allows blood flow in only one direction.

The right atrium (RA) has a larger volume coupled with thinner walls (approximately 2 mm) compared with the left atrium (LA). The RA is both anterior and to the right of the LA and extends inferior to it. The walls of the RA forms the right superior surface, the convex right (pulmonary) surface and little of the right side of the anatomical base.

Globally, the most common cause of death is cardiovascular disease (CVD). In Europe, it is responsible for about 45% of all deaths which amounts to over four (4) million death per year with coronary heart disease (CHD) being the most common single cause of death forming about 19% and 20% of deaths in men and women respectively far more than all deaths associated with cancer [1]. There are several diseases associated with the human heart and since the four (4) chambers of the heart are independent, they thus have different associated cardiac diseases. Some of the commonest heart diseases are inflammatory heart disease, ischemic heart disease, hypertensive heart disease, atrial fibrillation, atrial stunning just to mention but a few.

The initial means of measuring the LA pressure such as transbronchial and supraclavicular [2] were developed in the 1950s and are mainly direct means of accessing the LA. Despite the acceptable feasibility and safety of these methods, they were replaced by the indirect measurements of the LA pressure with the Swan-Ganz catheter [3]. Percutaneous access to the LA is mostly required in various minimally invasive procedures which includes catheter ablation for AF, percutaneous mitral valve replacement as well as left atrial appendage closure [3], [4].

## 1.1 - Motivation

A number of modern clinical procedures requires percutaneous diagnosis as well as local therapies. Most recent clinical interventions require percutaneous diagnosis where a thin tubular device such as catheter, needles, tissue ablation probes just to mention but a few are inserted into the soft and inhomogeneous tissue to access the desired target in this research, through the FO into the LA [5]. Biopsies, regional (local) anesthesia, blood sampling [6], brachytherapy [7] and neurosurgery [8] are examples of the several applications of percutaneous needle insertion. The success of the entire procedure is dependent on the accuracy of the percutaneous insertion [9] since research has shown that insertions with less needle misplacements have resulted in more successful treatments [10]. The success or desired performance of the procedure also depends on its complexity and the needle insertion placement accuracy ranges from micro-millimeters to some few millimeters [5] depending on the complexity of the procedure. The main causes of needle misplacements have been identified to be image misalignments, target uncertainty, movement of the target due to tissue deformation, needle deflection, imaging limitations and human errors [11]-[15].

Evaluation of most heart diseases are done by the measurement of the LA pressure hence the need to be able to get access to the LA. Open chest surgery was initially used but it required a longer operational period and a long surgical cut in the chest organ hence the rapid rise of minimally invasive procedures which requires only a small puncture through the skin to access the vascular system and subsequently the LA. Minimally invasive technique has a less post-operative pain, its faster, involves less blood loss, is less expensive and has a fewer procedural complications [16]. The two main minimally invasive techniques usually employed in accessing the LA are; transaortic (TA) and transseptal puncture (TSP). Due to the more direct pathway access the TSP provides to the LA compared to the TA procedure, it is the frequently used. In as much as this technique has been used for several years, it is still associated with a number of serious complications and/or failures due to the irregular anatomical structure of the atrium of certain patients as well as complex circumstances such as perforating large vessels [17].

TSP have had little modifications since the initial procedure was proposed in 1959 [18] and due to the introduction of new procedures for percutaneous structural heart disease therapy [3] and atria fibrillation ablation [19], there is the need for modifications. In recent years, the need for a more reliable, safe, efficient and patient-specific TSP procedure is inevitable. Despite the overall complications associated with TSP being less than 1% (<1%) according to research [2], [20], [21], its success rate basically depends on the experience of the physician to be able to puncture the optimal location (Fossa ovalis) of the septum to be able to access the LA [17]. If the right spot is not punctured, serious complications such as aortic root puncture, arterial air embolism, pericardial tamponade, right or left atrial wall puncture, transient ST-segment elevation, pleuritic chest pain, persistence of atrial septal defect and even death can be caused by this procedure (TSP) [17], [22]-[28].

Also, an inexperienced surgeon or physician performing this procedure have a higher rate of failure about 20%. They usually require a longer procedural time as well [29], [30].

Due to complexities associated with successfully puncturing of the FO, a second puncturing is highly possible and a research conducted between the first and repeated TSP procedure showed a greater level of failure rate and/or complications during the repeated

(second) TSP procedure compared with the first TSP procedure [31] hence the need for a more reliable procedure to puncture the FO during the first process.

Also, the human anatomy is not constant but mostly varies from patient to patient in terms of orientation and position. Some patients have abnormal atrium anatomy which requires a unique puncture position and orientation. It must be noted that the target might be in the millimeter neighbourhood of another organ, vessel or nerve indicating the need for an extra care to be taken in order to avoid damages to other organs and/or vessels hence the need for a patient-specific mechanical atria using finite element methods (FEM) to optimize the TSP procedure.

Efforts have been made to improve the efficiency of puncturing the target location through the use of RF needles [22], [25], [32], use of high resolution bidimensional X-ray images for pre-planning of the procedure [33], [34], use of robots [5], electroanatomic mapping [35]-[37] and intra-procedural 3D image acquisition using transesophageal [38]-[40] just to mention but a few. These efforts have not been too successful because there is no universally agreed strategy and equipment to be used to optimize the process hence each expert uses the one that best suites him/her making the process less reliable and universal.

## 1.2- Objectives

Computational models represent a novel framework for understanding the mechanisms behind a given phenomena and then provide a pathway for personalizing and optimizing the process or phenomena. The objectives of this dissertation is firstly to study the quantification of the mechanical properties of the tissues of the human atrium. Secondly, it is to study the puncturing of the human atria using a needle during a TSP procedure to:

- ✓ Help improve the efficiency of TSP procedure
- ✓ Make the procedure planning more accurate
- ✓ Make the TSP procedure more reliable
- ✓ Enhance the safety of the TSP procedure
- ✓ Help in the training of new physicians and surgeons in order to reduce the failure rate associated with inexperienced surgeons using this process or procedure
- ✓ Be able to predict the outcome of complex procedures
- ✓ Help in practicing of new procedures

These above mentioned objectives can be achieved by simulating the puncturing of a needle through the human heart using patient-specific FEM models.

## 1.3- Document structure

This document has six (6) chapters and below is a brief summary of the diverse chapters addressed by this document:

- ✓ **Chapter 1 - Introduction:** It gives an overview of the project as well as outlining the motivation and objectives of the dissertation. It also emphasizes the principal contributions of this work to the existing approaches.

✓ **Chapter 2 - Fundamentals:** This chapter deals with the anatomy and physiology of the human heart, it also discusses the anatomy of the human atrium, commonly associated diseases of the heart, means of accessing the human atrium as well as the existing treatment techniques employed in treating atrial diseases or disorders. It also reviews the finite element method (FEM) including the shape functions, weak and strong forms in one dimension as well as the coupled Eulerian-Lagrangian (CEL) method.

✓ **Chapter 3 - Biomechanical Simulation and Related Works:** With regards to the related works, an overview of the state-of-the-art of patient-specific anatomical cardiac models, biomechanical simulations, simulations of the atrium and needle insertion as well as the image-fusion and catheter tracking approaches were addressed.

✓ **Chapter 4 - Simulation Methodology:** Gives an in-depth knowledge about the procedures used in the modelling of the needle and tissue using FEM. It also throws more light on how the simulation of the needle insertion was performed. The needle and tissue geometry as well as the mechanical properties used for the simulation are presented in this chapter.

✓ **Chapter 5 - Simulation Results and Discussion:** The results from the simulation of the needle insertion, the discussions and challenges encountered during the simulation are presented in this chapter.

✓ **Chapter 6 - Conclusion and Future Perspectives:** The concluding remarks of the work done, limitations and proposed enhancements with respect to future works are presented in this chapter.

## 1.4 Principal contributions

An optimized needle was accurately modelled using the results obtained from the research performed by Wang *et al.* [41] in “optimal needle design for minimal insertion force and bevel length”. The optimized needle has a smaller bevel length compared to the commercial ones making it a preferred choice for procedures that involve vessel access. Also, it has a reduced needle insertion force thereby reducing the degree of deformation of the tissue.

Furthermore, since the CEL approach was used, there is no need to generate an algorithm to regenerate the mesh after significant distortions of the original mesh.

Almost all research works done in relation to this field used a single set of mechanical properties to denote the tissue patch being simulated but this research work however uses two sets of mechanical properties during the simulation process. The tissue being simulated was considered to be composed of two different types (the tender and soft tissues) since the human heart in reality has many tissues of different mechanical properties.

In addition, two sets of simulations were performed in this research; one representing the simulation of the soft tissues and the other simulation of the cardiac muscles to acquire an in-depth knowledge about the effects of the mechanical properties on the simulation results.

The effect of the size of the patch being simulated was analyzed by varying the size of the tissue patch being simulated and the corresponding results have been presented and

discussed. Also, the needle insertion forces during the needle insertion simulations were also evaluated in this project.

Also, the literature review provides adequate and relevant theoretical background to the reader which ranges from the anatomical and physiological properties of the heart and atrium, detailed review of the various ground-breaking researches done with respect to the simulation of the atrium and needle insertion. The reader is also enlightened on the fundamentals of the used computational methods through the review of the FEM.





# Chapter 2

## Fundamentals

This chapter gives a detailed structure and functions of the human heart. It also provides the reader with the details of the structure of the atrium, the associated diseases of the heart, currently existing treatment techniques of atrial diseases, the means of getting access to the left atrium as well as a vivid account of the TSP technique.

Access to the LA using the TSP technique was initially proposed in 1959 and has ever since been the standard approach for several left heart interventions [3], [38]. Due to the use of a transcatheter, non-invasive image acquisition of the patient anatomy is very vital coupled with pre-procedural planning based on high-resolution imaging techniques to assist in having a safe puncture site and define the best puncture route.

It also provides the reader with an in-depth knowledge of FEM and CEL method.

### 2.1 - Structure of the heart

The anterior portion of the heart is close to the sternum while the posterior border is nearer to the vertebral column. The wall of the heart has three main layers: the outer Pericardium, the middle Myocardium and the Inner Endocardium as shown in figure 2.1. The inner heart layers are protected by the connective tissues and adipose tissues that constitute the **epicardium**. They (connective and adipose tissues) also produce pericardial fluids that help to reduce friction between the pericardial membranes. The **myocardium** is composed predominantly of cardiac muscle tissues and they are organized in planes. It also has a lot of blood capillaries, lymph capillaries and nerve fibers. The **endocardium** consists of blood vessels and specialized cardiac muscle fibers called Purkinje Fibers, epithelium and connective tissue with elastic and collagen fibers.

Within the heart are four hollow chambers with two on both the left and right. The left atria and the left ventricle is separated from the right atria and right ventricle by the septum (solid wall-like structure). The septum prevents the blood from each chamber from mixing. The mature heart valves are composed of highly organized extracellular matrix (ECM) as well as valve interstitial cells (VIC) which are surrounded by endothelial cell layer. The distinct biomedical properties of the leaflets and supporting structures are provided by the ECM of the valves which are stratified into Elastin-rich, proteoglycan-rich and collagen-rich layer [42].

The atrioventricular valve (AV Valve) consists of the mitral valve which is located on the left and tricuspid valve which is on the right. These valves ensure the flow of blood in one direction between the atria and the ventricle. The AV valve is so called because they lie between the atria and the ventricle. The superior vena cava and the inferior vena cava as well as a smaller vein (coronary sinus) supplies the right atrium with blood. The tricuspid valve has cusps which are projections and are located between the right atrium and ventricle. The cusps of the tricuspid valve are attached to the chordae tendineae which are strong fibers that originates from the papillary muscles. The tricuspid valve allows blood to flow only from the right atrium into the right ventricle. The muscular wall of the right ventricle which pumps blood to the lungs is thinner compared to the left ventricle which is responsible for pumping blood to all parts of the body. The right ventricle encounters little resistance during its blood flow compared to the left ventricle. At the trunk's base is a pulmonary valve with three (3) cusps which only allows blood flow through the right ventricle.

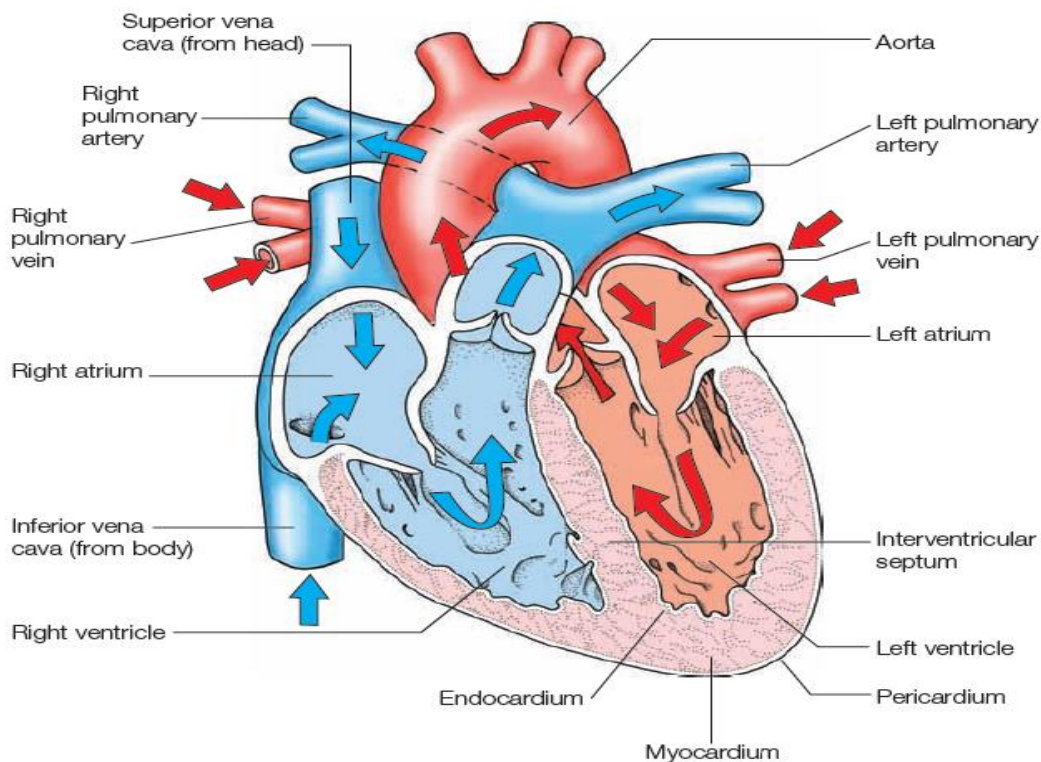


**Figure 2.1** - Cross-section of the heart showing the chambers and the direction of flow of blood [43]

The left atrium receives blood from four (4) pulmonary veins. Blood flows from the left atrium into the left ventricle through the mitral valve which also prevents backflow of blood. The mitral valve directs blood into the aorta by passively closing when the left ventricle contracts. The aortic valve is located at the base of the aorta. The aortic valve opens to allow the flow of blood from the left ventricle during contraction. The valve closes when the left ventricle relaxes, the valve closes to prevent blood from backing up into ventricle. The pulmonary valve and the aortic valve have “Half-Moon” shapes hence they are known as the semilunar valves.

The right atrium receives deoxygenated (low-oxygen) blood from the vena cava and coronary sinus. During the contraction of the right atrium, the blood passes through the tricuspid valve into the right ventricle. The contraction of the right ventricle causes the tricuspid

valves to close causing blood to move through the pulmonary valve into the pulmonary trunk and pulmonary arteries and further entering the capillaries of the alveoli of the lungs for gas exchange to take place.

The oxygenated blood enters the heart through the pulmonary veins into the left atrium and as the left atrium contracts, blood moves through the mitral valve into the left ventricle. The mitral valve closes when the left ventricle contracts causing blood to move through the aortic valve into the aorta and its branches.

The cardiac muscle fibers have a similar function as the skeletal muscle fibers but these cardiac muscles are connected in branched networks. In view of this, when any part of the network is stimulated, impulses are generated and sent throughout the heart causing it to contract as a single unit.

## 2.2 - Physiological functions of the heart

The heart is responsible for the circulation of blood to all parts of the body through two pathways: the pulmonary and systemic circuits.

One heartbeat or cardiac cycle involves the atria contraction (atrial systole) during which the ventricle relaxes (ventricular diastole) followed by contraction of the ventricles (ventricular systole) during which the atrial relaxes (atrial diastole). After this, there is a brief period of relaxation of both the atria and the ventricles. This process is well coordinated to ensure that the various actions by the chambers of the heart are effective.

The main parameters responsible for the closure and opening of the valves and the flow of blood through the heart chambers during one cardiac cycle are the changes in the pressure and volume in the heart chamber. A single heartbeat makes a double thumping sound which is heard during the use of the stethoscope. This sound is heard due to the vibrations of the heart tissues related to the closure of the Valves. The first sound is heard when the ventricle contracts when the AV valve closes and the second sound is heard when the ventricle relaxes when the pulmonary and aortic valve closes as shown in the figure 2.2 below. Table 2.1 is a summary of the heart valves and their functions.

## 2.3 - Physiological structure of the atrium

The superior RA is composed of the superior vena cava (SVC) and the right atrial appendages which are extensive muscular pouch which projects anteriorly to overlap the right portion of the aorta as shown in figure 2.3 below. The inferior surface of the RA can be divided into three (3) regions: the smooth-walled venous component, tricuspid valve and the appendage. The SVC receives blood from the superior portions of the body (head, neck and upper limbs), chest walls and the oesophagus. The inferior vena cava (IVC) however drains blood from all structures below (inferior) including the diaphragm into the lowest part of the atrium near the septum. The IVC is larger than the SVC. Blood circulation between the RA and the right ventricle (RV) is controlled by the tricuspid valve. The coronary sinus (CS) opens into the venous atrial component between the orifice of the IVC, the fossa ovalis and the vestibule. CS is a collection of vessels that receives blood the myocardium is draining into the RA [44].

Table 2.1 - Heart valves and their functions [43]

Heart Valve	Location	Action
Tricuspid valve	Between right atrium and right ventricle	During ventricular contraction, it prevents blood from moving from right ventricle into the right atrium
Pulmonary valve	At entrance to pulmonary trunk	During ventricular relaxation, it prevents blood from moving from pulmonary trunk into right ventricle
Mitral (bicuspid) valve	Between left atrium and left ventricle	During ventricular contraction, it prevents blood from moving from left ventricle into left atrium
Aortic valve	At entrance to aorta	During ventricular relaxation, it prevents blood from moving from aorta into the left ventricle

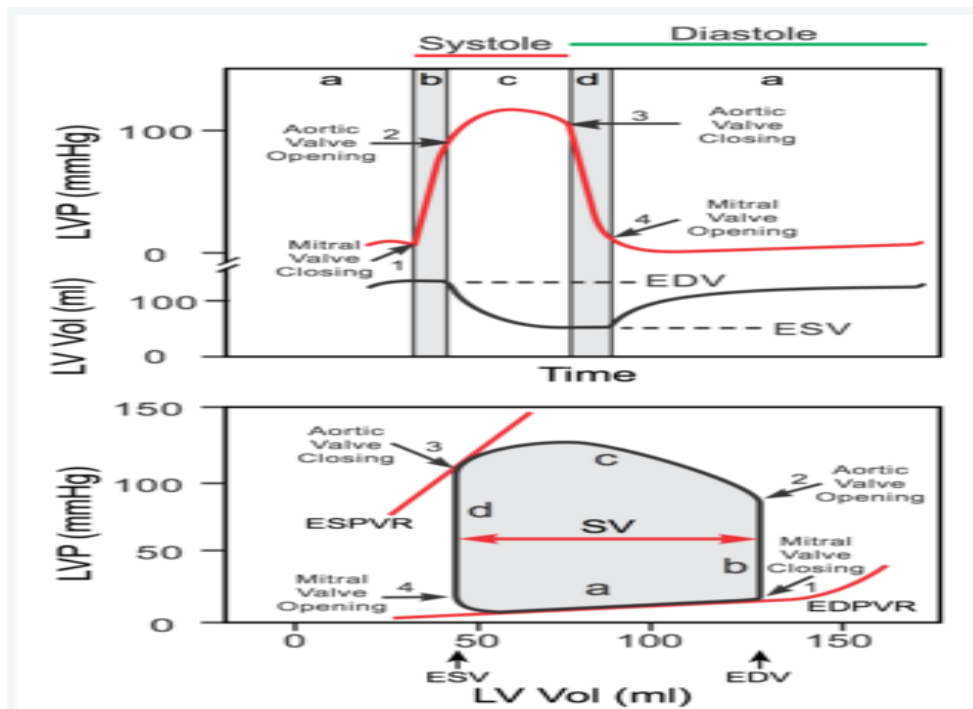


Figure 2.2 - Ventricular pressure-volume relationship [45]

The LA serves three main roles that exerts profound effect on the left ventricle (LV) filling as well as the overall cardiovascular performance. It is a contractile chamber that actively empties immediately before the onset of LV systole and establishes final LV end-diastolic volume [46]. LA is also a reservoir that stores pulmonary venous returns during LV contraction and isovolumic relaxation after the closure and before the opening of the mitral valve [47]. Finally, it is a conduit that empties its contents into the LV down a pressure gradient after the opening of the mitral valve [48] and also passively transferring pulmonary

venous blood flow during LV diastasis. LA has thicker walls (approximately 3 cm) hence smaller with respect to the RA. LA is cuboidal in shape with four (4) pulmonary veins and atrial appendage at the superior as shown in figure 2.3. At the inferior, the mitral valve is associated with controlling the blood circulation to the left heart [49]. It must also be noted that the aorta artery and the pulmonary artery cover externally the LA and the thin fibrous pericardium separates the LA from the oesophagus [50].

The interatrial septal wall (IAS) is a muscular structure found between the LA and the RA. It is composed of the fusion of the septum primum (LA septum) and the septum secundum (RA septum) [16]. The region where they fuse is known as the limbus (the area of fusion of the muscular septum secundum and the thin portion of the septum primum) which is the thickest region which has a depression called fossa ovalis (FO) in its middle. Both septae extend from the roof of the atria toward the endocardial cushions. The septum primum, which is the LA septum is absorbed superiorly leaving the septum secundum or the RA septum to cover this superior defect and separate the atria [51]. FO is oval or circular shaped that can only be identified from the RA. It has an average area of 1.5 to 2.4 cm<sup>2</sup> located posteriorly at the junction of the mid and lower third of the RA precisely between the IVC and CS [16]. It is also composed of thin fibrous tissues and it is the thinnest region of the IAS [52]. With regards to patients with dilated aorta and those with mitral valve disease and a bulging LA, the FO can be located more superiorly or inferiorly respectively [3].

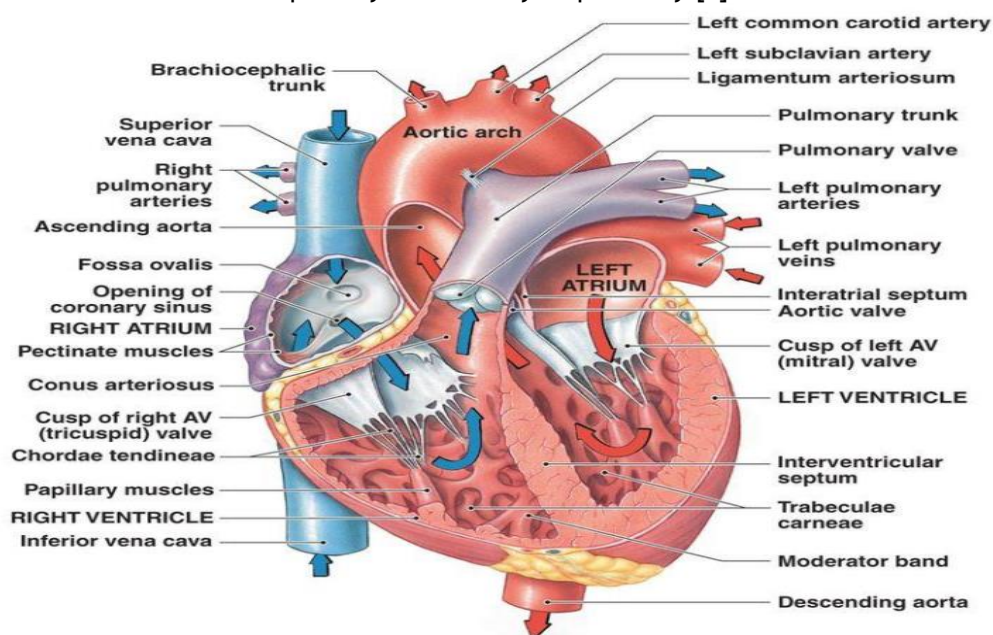


Figure 2.3 - Heart anatomy showing the atria [53]

## 2.4 - Common diseases associated with the heart

It is noteworthy that CVDs causes about 40% and 49% of all death among men and women respectively in Europe. The death ratio of CVDs increases with age and less common in younger age groups. CHDs is the type of cardiac disease in which a waxy substance referred to as plaque builds up gradually within the coronary arteries (responsible for

supplying oxygenated blood to the heart muscles) and with time ruptures or hardens reducing the flow of blood through the arteries [54].

In this work, I shall dwell on the diseases associated with the atrium in accordance with my motivation, the existing procedures to correct or cure these diseases as well as the deficiencies of the existing corrective procedures. Valve disease (Stenosis or regurgitation) is a significant public health problem which results in approximately 20000 deaths annually [55].

Atrial fibrillation (AF) is the type of arrhythmia where the atria beats irregularly and usually with no co-ordination with respect to the ventricles [56]. AF is the commonest acquired cardiac arrhythmia [57], [58] and the possibility of acquiring this disease increases with age precisely each decade of adult life [59], [60]. There are several plausible causes of AF which can either be cardiac or non-cardiac diseases which may cause abnormalities in cardiac electrophysiology thus serving as a substrate for the development of arrhythmia [61].

Another atrial disease is the atrial stunning (AS) which is basically the loss of mechanical atrial contraction following a successful cardioversion which usually take up to about six (6) weeks to regain normal atrial contraction [62]. A longer period of AS may result in an increased rate or risk of thromboembolism. The duration of the atrial fibrillation, atrial pressures and size as well as the presence of structural heart diseases are the main factors delaying the return of the normal atrial mechanical functioning according to research. The main mechanisms generating the impaired atrial mechanics in AS are however unknown [63], [64].

The intrinsic electrophysiological attributes of the atria are transformed during chronic AF due to the atrial fibrillation induced electrical remodelling (AFER) [65]-[69]. According to research, various clinical electrophysiological and experimental studies, the electrical remodelling is categorised by an abbreviated atrial action potential (AP) morphology which is usually associated with the underlying changes to density as well as kinetics of some membrane ionic currents [66]-[68], [70]-[72].

## **2.5 - Existing treatment techniques of atrial associated diseases**

Rate and rhythm control drugs are the first means of controlling atrial diseases such as AF and AS but when this is ineffective [56], then access to the left atrium is required to resolve the defect.

Percutaneous cardiac interventions (PCI) covers the minimally invasive procedures to access the left atrium done with the help of the blood circulation system. The open chest which was initially used required a longer time frame, a long surgical cut in the chest organ whereas the minimally invasive procedures require only a small puncture through the skin to have access to the vascular system and then to the portion of interest (LA). Minimally invasive technique has a less post-operative pain, it is faster, involves less blood loss, it is less expensive and has a fewer procedure complications [55].

It is however impossible to have a direct visualization of the target when employing the PCI due to the use of the vascular access and manipulating the surgical instrument is sometimes awkward. In view of this, special transcatheter surgical tools and imaging modalities such as ultrasound, fluoroscopy and computer tomography (CT) have been adopted to ensure a safe medical procedure and also to ease the difficulty and complexities of manipulating the surgical instruments.



## 2.6 - Accessing the left atrium

Evaluation of heart diseases are mostly done by the measurement of the LA pressure hence the need to be able to get access to the LA. Two main techniques are usually employed in accessing the LA namely; transaortic (TA) and transeptal puncture (TSP). A research performed to compare the two main techniques using a magnetic navigation system (MNS) in the USA revealed that they are relatively equal in success rate and procedure time using the MNS for the left-sided AP ablation [73].

When using the TA technique, a catheter inserted in the femoral artery is retrogradely advanced towards the left ventricle through the aortic valve. The catheter is then rotated about an angle of  $180^\circ$  and moved through the mitral valve (MV) into the LA chamber as shown in the figure 2.4 (a). Due to the  $180^\circ$  rotation associated with this technique, it becomes very difficult to manipulate the catheter thus hindering the effective performance of this procedure. This has therefore led to the frequent use of the TSP in recent times [17].

TSP however requires a catheter being inserted into the right atrium (RA) through the venous system. A needle is then moved through it (RA) to puncture the interatrial septum (IAS) and ultimately to get access to the LA. For ease of accessing the LA using the TSP, it is advisable to perform the puncture through the thinnest region of the IAS wall known as the fossa ovalis (FO).

In view of this, the TSP technique is noted to give a more direct access pathway to the LA compared to the TA technique [54] (figure 2.4 (b)). In as much as this technique has been used for several years, it is still associated with a number of serious complications and/or failures mainly due to abnormal anatomy structure of certain patient's atrium coupled with complex circumstances such as perforating large vessels [17].

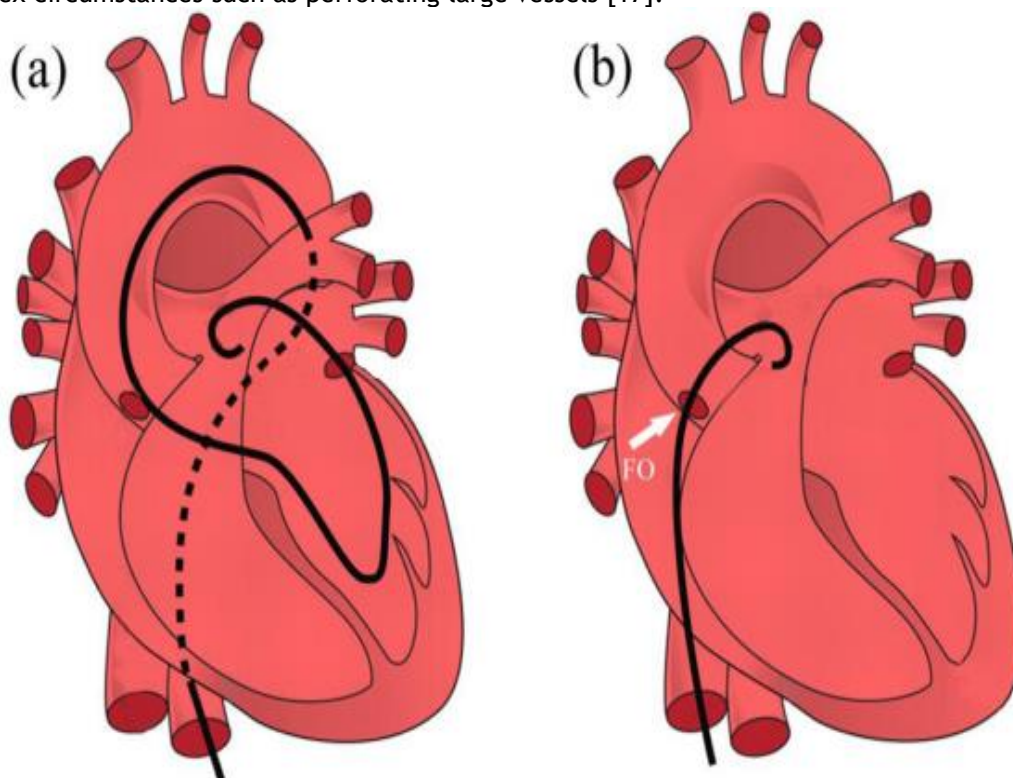


**Figure 2.4** - Schematic of transaortic route (a) and transeptal puncture technique (b) (adapted by Pedro André Gonçalves Morais et al from [74])

## 2.7 - Transseptal Puncture Technique

The introduction of new procedures for percutaneous structural heart disease therapy [3], [75] and atrial fibrillation ablation [19] in the last five (5) years has necessitated the need for enhancing TSP procedure. There has been only little modifications of the existing procedure since the initially proposed one in 1959 [76]. In this procedure, a needle is inserted into a catheter and the catheter is thus guided into the LA through a transseptal puncture from the RA septum through the FO. It is worth noting that the transseptal puncture limits the manoeuvrability of the catheter making it difficult in reaching the desired location of the left atrium [56]. As stated earlier, the FO is the thinnest portion of the IAS, it is the best route for the transseptal access to the LA. A thorough understanding of the anatomy of the FO and the surrounding landmarks play a vital role in having a successful procedure. Localization of the FO for TSP has traditionally been done or guided using the bi-dimensional fluoroscopy imaging. Auxilliary catheters are sometimes used to prevent puncture of vital structures and the time duration of this practice usually lasts about fifteen (15) minutes [22], [77], [78].

TSP begins with an insertion of the needle delivery catheter (guidewire) (0.81-0.89 mm) and dilator to the level of the SVC through the right common femoral vein with the help of the imaging techniques mentioned earlier. The guidewire is to define a safe route from the femoral vein to the SVC and also to position the dilator and sheath. The needle is then inserted into the dilator and allowed to freely rotate as it is advanced. Fluoroscopy is used to visualize the needle as it is advanced up to the tip of the dilator within the sheath to avoid unintentional passage out of the dilator and the sheath. Passage of the needle is easier if the sheath and dilator is introduced from the right other than the left femoral vein due to tortuosity (many twists).

Brockenbrough needle is the commonly used needle (Medtronic) [3] and it is an 18-gauge hollow tube that tapers distally to 21-gauge. Its proximal end has a flange with an arrow that points to the position of the tip of the needle. Now that the needle tip has been inserted into the dilator as shown in figure 2.6, the entire assembly (needle, dilator, sheath) is rotated such that the needle points to a 4 o'clock orientation (the ceiling of the room is classified as 12 o'clock orientation where as the floor is a 6 o'clock orientation) and withdrawn into the mid RA. With the help of the fluoroscopic projections (right anterior oblique (RAO)), the dilator is then advanced to meet the limbus of the FO (echocardiographic guidance is employed for patients without prominent limbus). The entire assembly is then advanced as a unit to tent the fossa ovalis. Two movements are usually detected; the first one indicates the entrance of the assembly into the RA and the second indicates the puncture into the FO region which is less perceptible. The needle is then rotated to 3 o'clock to avoid posterior puncture and then fully advanced. Due to the high risk of vital structures being perforated and the limitations in the maneuverability of the catheter in the LA. If the puncture is done outside the FO region, it requires that a comprehensive confirmation of the needle position should be considered [50] not forgetting the aorta, CS and His Bundle positions in order to have a safe route for the puncture. Pressure transduction through the needle is an indication that the needle has been able to puncture the LA as shown in figure 2.5.



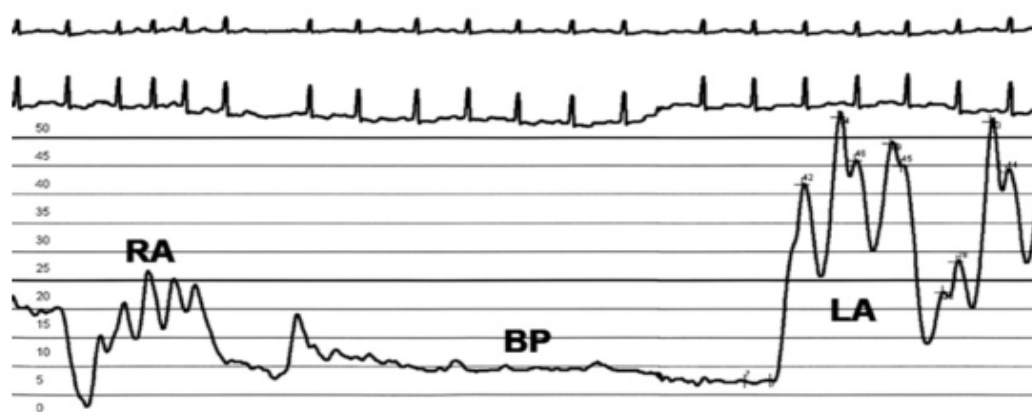


**Figure 2.5** - Pressure tracing from transeptal needle during TSP [3]

In about 20% to 25% of adult patients, the FO is probe patent and may not require needle puncture [51], [79]. In about two-thirds (2/3) of patients, the FO is paper thin and the catheter can be passed into the LA with just a gentle pressure and rotation of the dilator [51]. Generally speaking, the overall serious complications associated with TSP are  $\leq 1\%$  [2], [20], [21]. Physicians should note that: aortic root puncture, arterial air embolism, pericardial tamponade, right or left atrial wall puncture, transient ST-segment elevation, pleuritic chest pain, persistence of atrial septal defect and death are possible complications that can be caused by this procedure [17], [22]-[28]. After a successful puncture of the atrial septum, the patient should be anticoagulated immediately to minimize the risk of thromboembolism.

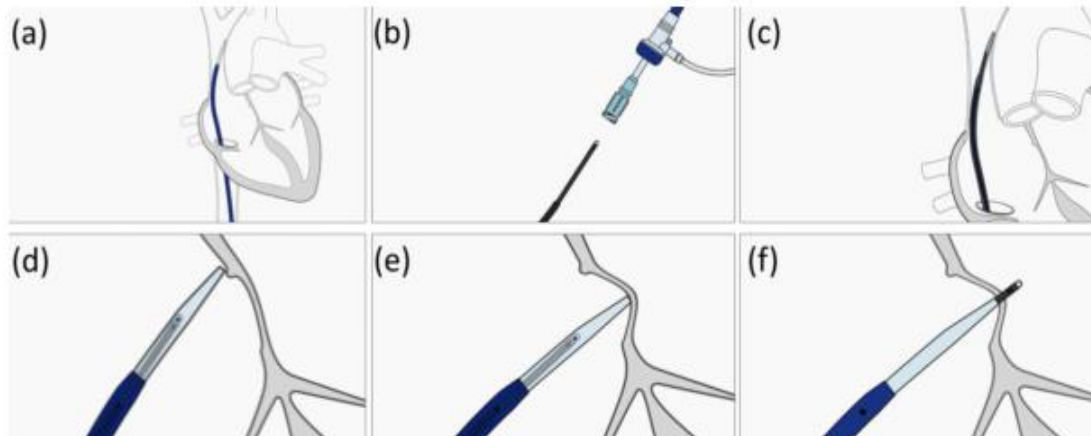


**Figure 2.6** - TSP technique. (a) A dilator and sheath placed into the SVC using the guidewire; (b) A needle is inserted into the dilator until (c) the SVC; the needle is pulled down and two movements are detected: (d) entrance into the RA and (e) entrance into the FO; (f) after the FO identification, the puncture is performed (adapted from: <http://www.baylismedical.com/physicians/nrg-rf-transeptal-needle/> (23/05/2016 )

## 2.8 - Finite element method review

The FEM is a numerical approach by which many physical, engineering and scientific phenomena described in terms of partial differential equations are solved approximately [80].

FEM has been employed in solving numerous engineering problems with complicated geometries, material properties and loadings such as heat transfer, fluid flow and stress analysis using computer simulations. It has also been used to predict the structural, mechanical, electrical, chemical and thermal behaviours of systems for performance and design analyses. FEM database is a key component of product development because it is used for several different analyses by using a tailored mesh [80].

FEM can be perceived to basically divide the physical phenomena into finite elements (smaller bodies) which are connected together by nodes and this is known as discretization. FEM has a systematic methodology to generate the required solution using a computer software. Generally, the number of nodes determine the number of unknowns to be computed by the computer software. The higher the number of elements and nodes, the more accurate the solution which are usually represented as computer visualization. FEM consists of five basic steps which are:

- 1) Preprocessing which involves the process of subdividing the problem domain into finite elements
- 2) Formulation of the elements by development of equations for the elements
- 3) Assembly which is basically acquiring equations for the entire system from the equations of the individual elements
- 4) Solving the equations
- 5) Postprocessing which involves the determination of the quantities of interest

There are numerous FEM programmes which includes; NASTRAN, ANSYS, LS-DYNA and ABAQUS. ABAQUS will be used in this dissertation because of its ability to allow users to program new material models and elements.

FEM has numerous applications such as analysis of surgical procedures, seismic analysis, crash analysis, fluid flow analysis as well as thermal and stress analyses. It also has the capabilities of predictive patient-specific medicine with the help of medical imaging and monitoring data to construct the model of the body part of interest [80] as in figure 2.7 below.

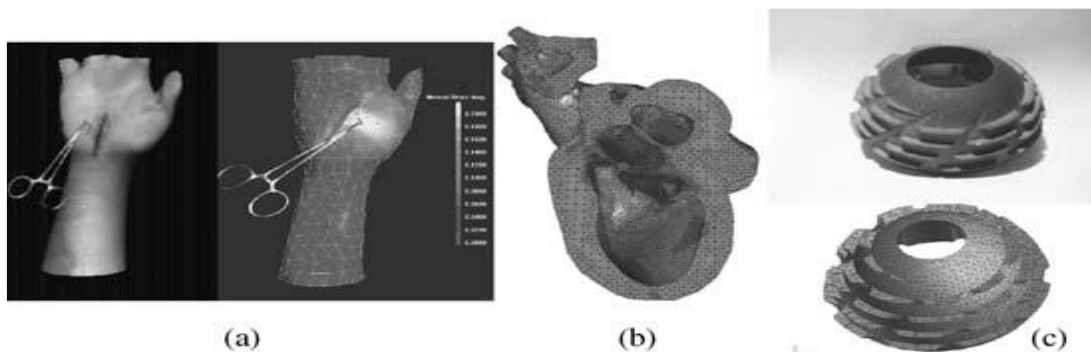


**Figure 2.7** - Applications in predictive medicine: (a) Overlying mesh of a hand model near the wound. (b) Cross-section of a heart model. (c) Portion of hip replacement showing the physical object and the FEM model [80].

## 2.9 - Strong and weak form in one dimension

The strong form consists of the governing equations as well as the boundary conditions for the physical system. The governing equations are usually partial differential equations

but for one-dimensional systems, they are just ordinary differential equations. The weak form is basically the integral form of these partial equations needed to formulate the FEM and it is the most challenging part in the development of finite elements [80].

Three distinct constituents or components are required to generate the discrete equation or system of equations. The constituents are;

- 1) The Strong form
- 2) The weak form
- 3) The approximation functions

To determine the strong form for an elastic bar of length  $l$  with an internal force  $p(x)$  shown in figure 2.8 loaded axially, the stress distribution ( $\sigma(x)$ ) in the bar will result from the deformation of the body characterized by the displacements of points in the body,  $u(x)$ . Assuming a body force  $b(x)$  is applied on the bar and the strain  $\epsilon(x)$  is obtained from the displacements.

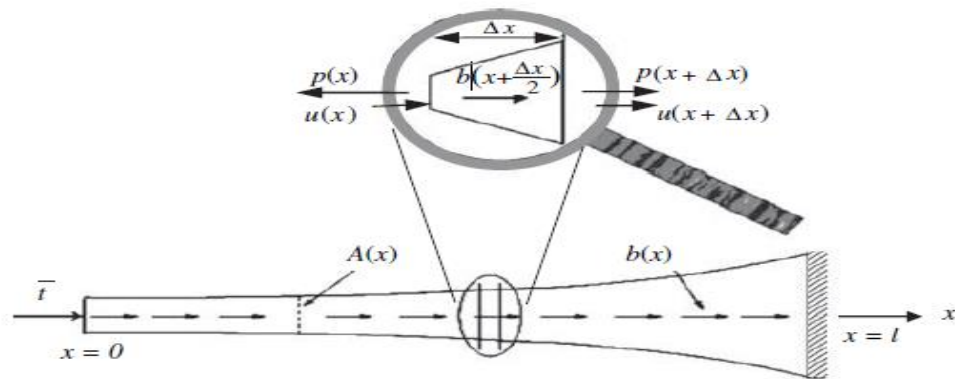


**Figure 2.8** - A one-dimensional analysis of an axially loaded elastic bar [80]

To determine the partial differential equation for the bar, the bar must meet the following conditions:

- 1) It must satisfy the Hooke's law:  $\sigma(x) = E(x) * \epsilon(x)$
- 2) It must be in equilibrium
- 3) It must satisfy the strain-displacement equation
- 4) The displacement field must be compatible

Summation of the forces in the x-axis of the zoomed region is given as:

$$-p(x) + b \left( x + \frac{\Delta x}{2} \right) \Delta x + p(x + \Delta x) = 0$$

By rearranging the above equation, we obtain

$$\frac{p(x + \Delta x) - p(x)}{\Delta x} + b \left( x + \frac{\Delta x}{2} \right) = 0$$

$$\text{As } \Delta x \rightarrow 0, \text{ we obtain } \frac{dp}{dx} + b(x) = 0 \quad (2.1)$$

Equation 2.1 is the equilibrium equation expressed in terms of the internal force  $p(x)$  and from the definition of stress as the force per unit cross-sectional area, the stress can be expressed as:

$$\sigma(x) = \frac{p(x)}{A(x)} \text{ and can be rewritten as } p(x) = \sigma(x) * A(x) \quad (2.2)$$

To determine the strain-displacement equation, we define the strain to be the ratio of the elongation to the original length mathematically expressed as:

$$\varepsilon(x) = \frac{\text{Elongation}}{\text{original length}}$$

$$\varepsilon(x) = \frac{u(x + \Delta x) - u(x)}{\Delta x}$$

$$\text{As } \Delta x \rightarrow 0, \text{ we obtain } \varepsilon(x) = \frac{du}{dx} \quad (2.3)$$

$$\text{Using Hooke's law, we obtain } \sigma(x) = E(x) * \varepsilon(x) \quad (2.4)$$

Where E is the Young's modulus of the material. By substituting equations (2.3) into (2.4) and then into (2.1), we obtain:

$$\frac{d}{dx} \left( A * E * \frac{du}{dx} \right) + b = 0, \quad \text{for } 0 < x < l \quad (2.5)$$

"U(x)" is the unknown function known as the dependent variable whereas x is the independent variable. Equation (2.1) applies to both linear and non-linear materials and equation (2.5) assumes linearity in the definition of strain as shown in equation (2.3) and stress-strain law in equation (2.4). The issue of compatibility is addressed by necessitating the displacement to be continuous [80].

The above differential equation is solved by setting the boundary conditions at the two ends of the element. Using the following specific boundary conditions: at x=l, there is a displacement of u(x=l) and at x=0, the stress denoted as t is prescribed. These conditions are thus written as:

$$\sigma(0) = \left( E \frac{du}{dx} \right) = \frac{P(0)}{A(0)} = -t$$

$$u(l) = \bar{u} \quad (2.6)$$

The strong form of the problem is the governing differential equation (2.5) along with the boundary conditions. The strong form is mathematically expressed to consist of the following equations:

$$\begin{aligned} \text{a) } & \frac{d}{dx} \left( A * E * \frac{du}{dx} \right) + b = 0, \quad \text{for } 0 < x < l \\ \text{b) } & \sigma(0) = \left( E \frac{du}{dx} \right) = \frac{P(0)}{A(0)} = -t \\ \text{c) } & u(x=l) = \bar{u} \end{aligned} \quad (2.7)$$

The weak form is obtained by restating the partial differential equations in an integral form. The weak form of the differential equation is equivalent to the governing equation and the boundary conditions (strong form). The weak form is sometimes called the principle of virtual work in stress analysis [80].

From the above developed strong form equations in (2.7), we can develop the weak form by firstly multiplying the governing equation (2.7a) and the traction boundary condition equation (2.7b) by an arbitrary function denoted as w(x) and integrating over the domains on which they are valid. In this case, the governing equation has a domain of [0,l] for the traction boundary condition, it has a cross-sectional area at A(0) where x=0. It is important to note that no integration is required at the traction boundary condition because the condition is valid at only a point where x=0 but the traction boundary condition is multiplied by the area (A). The obtained equations are mathematically expressed as:

$$\text{a) } \int_0^l w \left[ \frac{d}{dx} \left( AE \frac{du}{dx} \right) + b \right] dx = 0 \quad \forall w \quad (2.8)$$

$$b) \left( wA \left( E \frac{du}{dx} + t \right) \right) = 0 \quad \text{at } x = 0 \quad \forall w$$

The weight function denoted as  $w(x)$  is sometimes called the test function.  $\forall w$  is used in the above equations to indicate that  $w(x)$  is an arbitrary function meaning equation 2.8 must be valid for all functions of  $w(x)$ . The unpredictability of the weight function is very vital to make the weak form equivalent to the strong form. A better way of understanding the weight function is by viewing it as an enforcer as whatever it multiplies is enforced to be zero by its unpredictability. For convenience, all weight functions must satisfy the equation 2.9 below:

$$w(l) = 0 \quad (2.9)$$

Solving a weak form requires the use of admissible solutions  $u(x)$  that satisfies certain conditions and these solutions are either called the trial solutions or the candidate conditions. Very smooth trial solutions are required for higher derivatives hence it is not ideal to develop a FEM from equation 2.8 due to the second derivative of  $u(x)$ . Also, the resulting matrix would not be symmetric since the first integral is not symmetric in  $w(x)$  and  $u(x)$ . In view of these reasons, it is necessary to transform equation (2.8) into a form consisting of first derivatives shown in equation (2.10) in order to obtain a symmetric stiffness matrix efficient to use less smooth solutions thereby simplifying the treatment of the traction boundary condition.

$$\int_0^l w \frac{d}{dx} \left( AE \frac{du}{dx} \right) dx + \int_0^l wb dx = 0 \quad \forall w \quad (2.10)$$

Recalling the rule of taking the derivative of a product expressed below:

$$\frac{d}{dx} (wf) = w \frac{df}{dx} + f \frac{dw}{dx} \Rightarrow w \frac{df}{dx} = \frac{d}{dx} (wf) - f \frac{dw}{dx}$$

The above can be integrated over the domain  $[0, l]$  to obtain:

$$\int_0^l w \frac{df}{dx} dx = \int_0^l \frac{d}{dx} (wf) dx - \int_0^l f \frac{dw}{dx} dx$$

Using the fundamental theorem of calculus which states that the integral of a derivative of a function is the function itself and applying the integration by parts to the first integral of the right-hand side above with the domain  $[0, l]$ , we obtain:

$$\begin{aligned} a. \int_0^l w \frac{df}{dx} dx &= [wf]_0^l - \int_0^l f \frac{dw}{dx} dx \\ b. \int_0^l w \frac{df}{dx} dx &= [wf]_{x=l} - [wf]_{x=0} - \int_0^l f \frac{dw}{dx} dx \end{aligned} \quad (2.11)$$

Integration by parts is a very useful tool whenever we intend to relate strong forms to weak forms. Applying integration by parts to equation (2.10) by taken  $f = AE \left( \frac{du}{dx} \right)$ , equation (2.11a) can then be rewritten as:

$$\int_0^l w \frac{d}{dx} \left( AE \left( \frac{du}{dx} \right) \right) dx = \left[ wAE \frac{du}{dx} \right]_0^l - \int_0^l \frac{dw}{dx} AE \frac{du}{dx} dx \quad (2.12)$$

Substituting equation (2.12) into equation (2.10) we obtain the following equation with  $w(l) = 0$ :

$$\left[ wAE \frac{du}{dx} \right]_0^l - \int_0^l \frac{dw}{dx} AE \frac{du}{dx} dx + \int_0^l wb dx = 0 \quad \forall w \quad (2.13)$$

$$\text{But } \sigma = E \frac{du}{dx}$$

Hence equation (2.13) can be rewritten as with  $w(l) = 0$ :

$$[wA\sigma]_{x=l} - [wA\sigma]_{x=0} - \int_0^l \frac{dw}{dx} AE \frac{du}{dx} dx + \int_0^l wb dx = 0 \quad \forall w$$

From equation (2.9), it can be noticed that the first part of the equation above (i.e.  $[wA\sigma]_{x=l}$ ) goes to zero hence the need to develop weight functions that vanish on prescribed displacement boundaries to result in loss of symmetry in the final equations. Also, from equation (2.8b), it can be noticed that the second term of the above equation is equal to  $(wAt)$  at  $x=0$  hence the above equation can be simplified as:

$$\int_0^l \frac{dw}{dx} AE \frac{du}{dx} dx = [wAt]_{x=0} + \int_0^l wb dx = 0 \quad \forall w \quad \text{at } w(l) = 0 \quad (2.14)$$

Summarizing the work done so far in the weak form, the governing equation was multiplied with the traction boundary by an arbitrary, smooth weight function and integrated the products over the domains where they are valid. Furthermore, the expressions were added and transformed the integral to obtain lower order derivatives.

The crux of the development of the weak form is stated as: the trial solution  $u(x)$  that satisfies the above equation (2.14) for all smooth  $w(x)$  with  $w(l) = 0$  is the solution. The solution is thus calculated by finding  $u(x)$  among the smooth functions that satisfy  $u(l) = \bar{u}$  such that:

$$\int_0^l \frac{dw}{dx} AE \frac{du}{dx} dx = [wAt]_{x=0} + \int_0^l wb dx = 0 \quad \forall w \quad \text{with } w(l) = 0 \quad (2.15)$$

The above equation (2.15) is known as the weak form in that the solutions to the weak form does not need to be as smooth as solutions of the strong form (i.e. weak form have weaker continuity requirements). Satisfying the displacement boundary condition is very vital for the trial solutions and these boundary conditions are sometimes referred to as essential boundary conditions. Natural boundary conditions are the conditions of the derivative of the displacement “ $u(x)$ ”. The traction boundary conditions originate naturally from the weak form (2.15) so there is no need to generate trial solutions to satisfy the traction boundary conditions [80].

Admissible is the term used to represent trial solutions that are smooth and satisfies the essential boundary conditions as well as weight functions that are smooth and vanishes on essential boundaries. Using weak forms to solve a problem requires that the trial solutions and weight functions are admissible.

The advantage of the weak form is that it is a statement of equilibrium cast in the form of an integral over the volume of the body and approximations can be introduced using test functions [81].

## 2.10 - Shape functions and Gauss integration

Shape functions constitute the subset of element approximation functions and cannot be selected arbitrarily. For a one-dimensional element with  $m$  nodes shown in figure 2.9, the element approximation function for the field variable ( $\emptyset(x)$ ) is assumed to be a polynomial with  $(m-1)$  order [82] expressed mathematically as:

$$\emptyset^e(x) = \alpha_1 + \alpha_2 x + \alpha_3 x^2 + \alpha_4 x^3 + \dots + \alpha_{m-1} x^{m-2} + \alpha_m x^{m-1} \quad (2.16)$$

The above equation can be simplified as:

$$\emptyset^e(x) = g^T \alpha \quad (2.17)$$

Where  $g^T$  is composed of  $\{1 \ x \ x^2 \ x^3 \ \dots \ x^{m-1}\}$  and  $\alpha^T = \{\alpha_1 \ \alpha_2 \ \alpha_3 \ \dots \ \alpha_m\}$ . It is important to note that the number of generalized coordinates ( $\alpha_i$ , where  $i=1,2,3,4, \dots, m$ ) are equivalent to the number of nodes within the element.

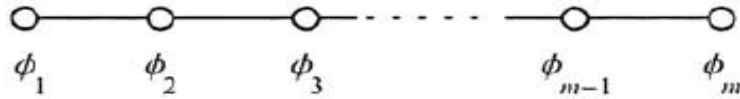


Figure 2.9 - A one-dimensional element with m nodes [82]

The field variable,  $\vartheta^e(x)$  can be expressed through the use of its nodal values  $\vartheta_i$  ( $i=1,m$ ) mathematically denoted as:

$$\vartheta^e(x) = N_1\vartheta_1 + N_2\vartheta_2 + N_3\vartheta_3 + N_4\vartheta_4 + \dots + N_{m-1}\vartheta_{m-1} + N_m\vartheta_m \quad (2.18)$$

The above equation can be simplified as:

$$\vartheta^e(x) = N^T \varphi \quad (2.19)$$

Where  $N^T$  is composed of  $\{N_1 \ N_2 \ N_3 \ \dots \ N^{m-1}\}$  and  $\varphi^T = \{\vartheta_1 \ \vartheta_2 \ \vartheta_3 \ \dots \ \vartheta_m\}$

$N_i$  is known as the shape function and are related with node “i” and must have a unit value at node “i” and a zero (0) value at all other nodes. Also, they must have the same degree of polynomial variation as indicated in the element approximation function [82].

The unambiguous form of the shape functions can be determined by solving for the generalized coordinates  $\alpha_i$  in terms of nodal coordinates  $x_i$  as well as nodal values  $\vartheta_i$  ( $i=1,2,3, 4,\dots, m$ ) using equation (2.16) to obtain equation 2.20 shown below:

$$\begin{aligned} \vartheta_1 &= \alpha_1 + \alpha_2 x_1 + \alpha_3 x_1^2 + \alpha_4 x_1^3 + \dots + \alpha_{m-1} x_1^{m-2} + \alpha_m x_1^{m-1} \\ \vartheta_2 &= \alpha_1 + \alpha_2 x_2 + \alpha_3 x_2^2 + \alpha_4 x_2^3 + \dots + \alpha_{m-1} x_2^{m-2} + \alpha_m x_2^{m-1} \\ &\vdots \\ \vartheta_m &= \alpha_1 + \alpha_2 x_m + \alpha_3 x_m^2 + \alpha_4 x_m^3 + \dots + \alpha_{m-1} x_m^{m-2} + \alpha_m x_m^{m-1} \end{aligned} \quad (2.20)$$

The above equation (3.20) can be represented in a matrix form as:

$$\begin{Bmatrix} \vartheta_1 \\ \vartheta_2 \\ \vartheta_3 \\ \vdots \\ \vartheta_m \end{Bmatrix} = \begin{bmatrix} 1 & x_1 & x_1^2 & \dots & x_1^{m-1} \\ 1 & x_2 & x_2^2 & \dots & x_2^{m-1} \\ 1 & x_3 & x_3^2 & \dots & x_3^{m-1} \\ \vdots & \vdots & \vdots & \ddots & \vdots \\ 1 & x_m & x_m^2 & \dots & x_m^{m-1} \end{bmatrix} \begin{Bmatrix} \alpha_1 \\ \alpha_2 \\ \alpha_3 \\ \vdots \\ \alpha_m \end{Bmatrix} \quad \text{or} \quad \varphi = A \alpha$$

From the above, the generalized coordinates ( $\alpha$ ) using the nodal coordinates ( $x$ ) and nodal values ( $\vartheta$ ), we obtain:

$$\alpha = A^{-1} \varphi \quad (2.21)$$

From the above, substituting the equation (2.21) into equation (2.17) we obtain:

$$\vartheta^e(x) = g^T A^{-1} \varphi \quad (2.22)$$

By equating equations (2.19) and (2.22), we obtain the equation (2.23) which gives the explicit form of the shape functions  $N_i$  as:

$$N^T = g^T A^{-1} \quad (2.23)$$

Shape functions are expected to possess these properties:

1)  $N_i = 1$  at node  $i$  and  $N_i = 0$  at all other nodes

2)  $\sum_{i=1}^m N_i = 1$

Shape functions of various orders and dimensions enable the FEM to solve problems of many types with fluctuating degrees of accuracy. Shape functions have a fundamental property known as the interpolation property. Interpolants are known as functions that exactly

pass through the data. Picturing the nodal values ( $\emptyset$ ) as data then the shape functions are interpolants of the nodal data and can subsequently be used to fit any data [80].

The shape functions in one dimension are usually called Lagrange interpolants and it plays a very important role in the construction of the interpolants of various orders such as quadratic or cubic functions. It is important to note that higher order elements usually provide more accuracy compared to linear elements [80].

From the above properties of shape functions, the shape function “i” must vanish at all nodes other than node “i” and be unity at node i [80]. By using this ideology, it is much easier to construct the shape function as shown below.

Considering a three-node element, the quadratic shape function is constructed by firstly developing the shape function at node 1. As the shape function  $N_1(x)$  is at most quadratic in  $x$ , it consists of a product of two linear monomials in “ $x$ ” expressed generally as:

$$N1(x) = \frac{(x-a)(x-b)}{c} \quad (2.24)$$

Where  $a$ ,  $b$  and  $c$  are constants that must satisfy the properties of the shape function. We expect  $N_1(x)$  to vanish at  $x_2$  and  $x_3$  and can be achieved by making  $a = x_2$  and  $b = x_3$  to satisfy the condition that it must vanish at nodes 2 and 3. This gives us:

$$N1(x) = \frac{(x-x_2)(x-x_3)}{c} \quad (2.25)$$

To satisfy the condition of  $N_1(x_1) = 1$ , we make the denominator ( $c$ ) being equal to the numerator evaluated at  $x_1$  represented as:

$$N1(x) = \frac{(x-x_2)(x-x_3)}{(x_1-x_2)(x_1-x_3)} \quad (2.26)$$

Similarly, the two other shape functions are derived and represented as:

$$N2(x) = \frac{(x-x_1)(x-x_3)}{(x_2-x_1)(x_2-x_3)} \quad (2.27)$$

$$N3(x) = \frac{(x-x_1)(x-x_2)}{(x_3-x_1)(x_3-x_2)} \quad (2.28)$$

Generally speaking, it is impossible to integrate the weak form in closed form hence the need for numerical integration. Gauss quadrature is one of the most efficient integration approach for functions that are polynomials or nearly polynomial and since FEM uses integrals that usually involve polynomials, Gauss quadrature is the ideal option. Gauss quadrature formulas are always given over a parent domain  $[-1,1]$ . Gauss quadrature provides the weights and integration points that yield a precise integral of a polynomial of a given order [80]. Gauss integration is mostly used with second-order isoparametric elements due to its efficiency and it is best suited to the polynomial product interpolations used in these elements. For the first-order elements, the single-point reduced-integration scheme which is based on uniform strain formulation (the strains are not obtained at the first-order Gauss point but rather analytically calculated as the average strain over the volume of the element) [81].

Given the integral:

$$I = \int_a^b f(x) dx = ? \quad (2.29)$$

It is possible to map the one-dimensional domain from the parent domain  $[-1,1]$  to the physical domain  $[a, b]$  using a linear mapping shown in figure 2.10 below at  $x = a$ ,  $\xi = -1$  and at  $x = b$ ,  $\xi = 1$ . Equation (2.30) relates  $x$  and  $\xi$  as shown below [80]:

$$x = \frac{1}{2} (a + b) + \frac{1}{2} \xi(b - a) \quad (2.30)$$



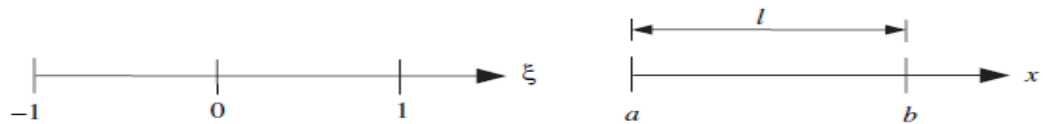


**Figure 2.10** - Mapping of the one-dimensional domain from the parent domain [-1,1] to the physical domain [a,b] [80].

From the above equation (2.30), it is possible to rewrite the equation directly in terms of the linear shape functions as shown below:

$$x = x_1 N_1(\xi) + x_2 N_2(\xi) = a \left( \frac{1-\xi}{2} \right) + b \left( \frac{\xi+1}{2} \right)$$

From equation (2.30) above, we arrive at:

$$dx = \frac{1}{2} (b - a) d\xi = \frac{l}{2} d\xi = J d\xi \tag{2.31}$$

Where J is known as the Jacobian and mathematically represented as  $J = (b-a)/2$ . Hence the initial integral in equation (2.29) can be rewritten as:

$$I = J \int_{-1}^1 f(\xi) d\xi = J \hat{I} \text{ and } \hat{I} = \int_{-1}^1 f(\xi) d\xi \tag{2.32}$$

In the above outlined Gauss integration procedure, the integral was approximated by the weights ( $W_i$ ) and points ( $\xi_i$ ) at which the integrand is evaluated as shown below in equation (2.33) where:

$$W^T = [W_1 \ W_2 \ W_3 \ \dots \ W_n] \text{ and } f = \begin{bmatrix} f(\xi_1) \\ f(\xi_2) \\ f(\xi_3) \\ \vdots \\ f(\xi_n) \end{bmatrix} \tag{80}$$

$$\hat{I} = W_1 f(\xi_1) + W_2 f(\xi_2) + W_3 f(\xi_3) + \dots + W_n f(\xi_n) = [W_1 \ W_2 \ W_3 \ \dots \ W_n] \begin{bmatrix} f(\xi_1) \\ f(\xi_2) \\ f(\xi_3) \\ \vdots \\ f(\xi_n) \end{bmatrix} \tag{2.33}$$

$= W^T f$

Gauss quadrature is basically aimed at choosing the weights and integration points to ensure that the highest possible polynomial is integrated precisely and to be able to achieve this, the function  $f(\xi)$  is approximated by a polynomial in equation (2.34) where:

$$p(\xi) = [1 \ \xi \ \xi^2 \ \xi^3 \ \dots \ \xi^n] \text{ and } \alpha = \begin{bmatrix} \alpha_1 \\ \alpha_2 \\ \alpha_3 \\ \vdots \\ \alpha_n \end{bmatrix} \tag{80}$$

$$p(\xi) = \alpha_1 + \alpha_2 \xi + \alpha_3 \xi^2 + \alpha_4 \xi^3 = [1 \ \xi \ \xi^2 \ \xi^3 \ \dots \ \xi^n] \begin{bmatrix} \alpha_1 \\ \alpha_2 \\ \alpha_3 \\ \vdots \\ \alpha_n \end{bmatrix} = p(\xi) \alpha \tag{2.34}$$

The values of the coefficient  $\alpha_i$  can be expressed in terms of the function  $f(\xi)$  at the integration points to obtain:

$$\begin{aligned} f(\xi_1) &= \alpha_1 + \alpha_2 \xi_1 + \alpha_3 \xi_1^2 + \dots + \alpha_{n-1} \xi_1^{n-1} \\ f(\xi_2) &= \alpha_1 + \alpha_2 \xi_2 + \alpha_3 \xi_2^2 + \dots + \alpha_{n-1} \xi_2^{n-1} \\ &\vdots \\ f(\xi_n) &= \alpha_1 + \alpha_2 \xi_n + \alpha_3 \xi_n^2 + \dots + \alpha_{n-1} \xi_n^{n-1} \end{aligned} \text{ or } \underbrace{\begin{bmatrix} f(\xi_1) \\ f(\xi_2) \\ \vdots \\ f(\xi_n) \end{bmatrix}}_f = \underbrace{\begin{bmatrix} 1 & \xi_1 & \xi_1^2 & \dots \\ 1 & \xi_2 & \xi_2^2 & \dots \\ \vdots & \vdots & \vdots & \vdots \\ 1 & \xi_n & \xi_n^2 & \dots \end{bmatrix}}_M \underbrace{\begin{bmatrix} \alpha_1 \\ \alpha_2 \\ \vdots \\ \alpha_n \end{bmatrix}}_\alpha \tag{2.35}$$

From equations (2.35) and (2.33), the integral  $\hat{I}$  can be expressed as:

$$\hat{I} = W^T M \alpha \tag{2.36}$$

In order to determine the appropriate weights and quadrature points to be used, there is the need to integrate the polynomial  $f(\xi)$  where  $[\xi \ \xi^2/2 \ \xi^3/3]_{-1}^1 = [2 \ 0 \ 2/3 \ 0 \ \dots]$ :

$$\hat{I} = \int_{-1}^1 f(\xi) d\xi = \int_{-1}^1 [1 \ \xi \ \xi \ \xi \ \dots] \begin{bmatrix} \alpha_1 \\ \alpha_2 \\ \alpha_3 \\ \vdots \\ \alpha_n \end{bmatrix} d\xi = [\xi \ \xi^2/2 \ \xi^3/3]_{-1}^1 \alpha = P \alpha \tag{2.37}$$

The weights and quadrature points are selected in a way that  $\hat{I}$  found in equation (2.36) is equal to that in equation (2.37) as shown below:

$$W^T M \alpha = P \alpha = M^T W = P^T \tag{2.38}$$

Equation (2.38) is a system of nonlinear algebraic equations for the unknown matrices  $M$  and  $W$ . For  $n_{gp}$  number of Gauss points, the polynomial of order  $q$  that can be integrated exactly is given in equation (2.39) because a polynomial of order  $q$  is denoted by  $q+1$  parameters. Since both the weights and integration points are adjustable, the  $n_{gp}$  point Gauss integration scheme has  $2n_{gp}$  parameters that can be evaluated to integrate the polynomial of  $q$ -order precisely. Hence, an  $n_{gp}$  point Gauss formula can integrate a polynomial of order  $(2n_{gp} - 1)$  precisely following the fact that the number of integration points required to precisely integrate a polynomial of order  $q$  is given by equation (2.40) [80].

$$q \leq 2n_{gp} - 1 \tag{2.39}$$

$$2n_{gp} \geq \frac{q+1}{2} \tag{2.40}$$

## 2.11 - Discretization of the equilibrium equation into a FEM

It is the process of obtaining a finite number of discrete equations from the weak form [80]. Given a beam area, to be able to discretize it effectively, we firstly need to select the element type, followed by the determining the thickness of the element and lastly, dividing the beam area into elements [83].

Given the domain  $\Omega$  as shown in figure 2.11 with boundary  $\Gamma$ , to discretize using 2D elements such as triangles or quadrilaterals, the total number of elements is denoted by  $n_{el}$ . In principle, different shape functions could be employed for each of the components ( $x, y$ ) but the  $x$  and  $y$  components of the displacement field “ $u$ ” is given as  $u = [u_x, u_y]^T$  generally approximated by the same shape functions [80].

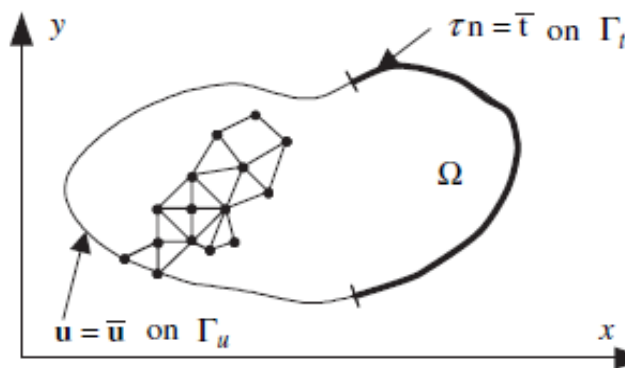


Figure 2.11 - Finite element in 2D with domain  $\Omega$  and boundary  $\Gamma$  [80].

Due to the two components (i.e. x and y), there are two degrees-of-freedom per each node and the nodal displacement (d) matrix is given as shown below where n is the number of nodes in the finite element mesh:

$$d = [ u_{x1} \ u_{y1} \ u_{x2} \ u_{y2} \ u_{x3} \ u_{y3} \ \dots \ u_{xn} \ u_{yn} ]^T$$

The displacement field can be written in terms of the shape functions hence depends on the type of the element and the number of nodes present. The finite element approximation of the trial solution and the weight function on each element can be expressed mathematically as:

$$\begin{aligned} u(x,y) &\approx u^e(x,y) = N^e(x,y) d^e \text{ where } (x,y) \in \Omega^e \\ w^T(x,y) &\approx w^{eT}(x,y) = w^{eT} N^e(x,y)^T \text{ where } (x,y) \in \Omega^e \end{aligned} \quad (2.41)$$

The element shape function matrix  $N^e$ , element nodal displacement  $d^e$  and the element weight function  $w^e$  in the above equation (2.41) are given as follows:

$$N^e = \begin{bmatrix} N1 & 0 & N2 & 0 & N3 & 0 & \dots & Nn & 0 \\ 0 & N1 & 0 & N2 & 0 & N3 & \dots & 0 & Nn \end{bmatrix}$$

$$d^e = [ u_{x1}^e \ u_{y1}^e \ u_{x2}^e \ u_{y2}^e \ u_{x3}^e \ u_{y3}^e \ \dots \ u_{xn}^e \ u_{yn}^e ]^T$$

$$w^e = [ w_{x1}^e \ w_{y1}^e \ w_{x2}^e \ w_{y2}^e \ w_{x3}^e \ w_{y3}^e \ \dots \ w_{xn}^e \ w_{yn}^e ]^T$$

The finite element approximation should be continuous (i.e. smooth over the element domains) but have kinks at the boundaries of the element [80]. The integral over the domain  $\Omega$  in the weak form denoted is calculated as the sum of integrals over the element domains  $\Omega^e$ .

The strains are thus expressed in terms of the element shape functions and the nodal displacements. The strain-displacement equation is expressed in relation to the symmetric gradient operator and mathematically expressed as:

$$\varepsilon = \begin{bmatrix} \varepsilon_{xx} \\ \varepsilon_{yy} \\ \varepsilon_{zz} \end{bmatrix} \approx \varepsilon^e = \nabla_s u^e = \nabla_s N^e d^e = B^e d^e \quad (2.42)$$

$B^e$  is known as the strain-displacement matrix and given as:

$$\begin{bmatrix} \frac{\partial N1}{\partial x} & 0 & \frac{\partial N2}{\partial x} & 0 & \frac{\partial N3}{\partial x} & 0 & \dots & \frac{\partial Nn}{\partial x} & 0 \\ 0 & \frac{\partial N1}{\partial y} & 0 & \frac{\partial N2}{\partial y} & 0 & \frac{\partial N3}{\partial y} & \dots & 0 & \frac{\partial Nn}{\partial y} \\ \frac{\partial N1}{\partial y} & \frac{\partial N1}{\partial x} & \frac{\partial N2}{\partial y} & \frac{\partial N2}{\partial x} & \frac{\partial N3}{\partial y} & \frac{\partial N3}{\partial x} & \dots & \frac{\partial Nn}{\partial y} & \frac{\partial Nn}{\partial x} \end{bmatrix} = B^e$$

## 2.12 - Coupled Eulerian-Lagrangian method

Given a continuum which deforms or flows, the position of the small volumetric elements changes with time and the changes in positions are described as functions of time basically in two main processes: Lagrangian and Eulerian descriptions [84].

During the Lagrangian description, the movement of the continuum is defined as a function of the material coordinates and time. It is mostly used in solid or structure mechanics where the nodes of the mesh move together with the material. In view of this, the interface between two parts is defined and tracked accurately. However, simulations with large deformations may result in a tangling mesh with relatively large element distortions [85] as

shown in figure 2.12 below. The tangling mesh results in a less accurate solution hence the need for remeshing to avoid the distortion of the mesh and thus an increase in computational time and computational power [86]. Lagrangian approach is more applicable and effective with materials with high elastic or Young's modulus which ideally have relatively smaller associated deformations [87].

During Lagrangian description, the spatial part of the domain is discretized by 1, 2 or 3 dimensional elements. Lagrangian elements are seen to be constant mass elements which deforms as the attached material begins to deform as shown in figure 2.12 [88].

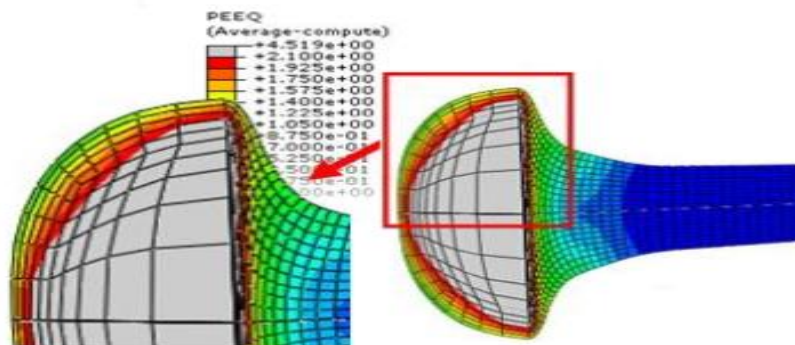


Figure 2.12 - Lagrangian mesh [87]

In the Eulerian description, the movement of the continuum is specified as a function of the spatial coordinate and time. It is mostly applied in fluid mechanics and requires a Eulerian reference mesh which remains unchanged or undistorted to trace the motion of the material in the Eulerian domain. The material has the ability to move freely through the Eulerian mesh. During this process, there is no associated element distortions but there is also the possibility of numerical diffusion in cases where two or more materials are present in the Eulerian domain [85]. The nodes are fixed while the material flows through the mesh instead of following each particle as described in the Lagrangian formulation above [86].

The frame of the Eulerian is fixed in space and the domain is divided into elements. The deformation and movement of the material is detected as the material flows through the elements. Fine meshes are required in areas with high gradients as shown in figure 2.13. It is also worth noting that large deformations do not necessarily increase the required computational time. Due to this advantage, it is mostly used in fluid mechanics even though it has the challenge of precisely tracking an interface [87].

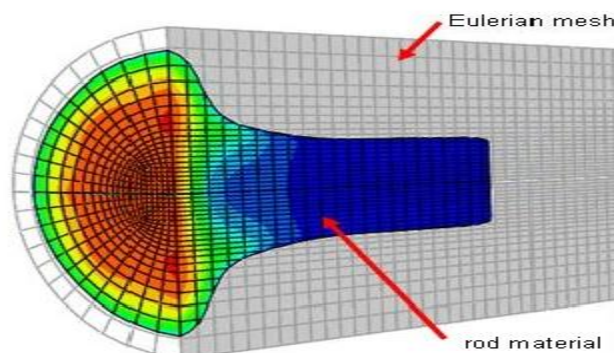


Figure 2.13 - Eulerian mesh [87]

During the Eulerian formulation, the spatial portion of the domain is discretized by volume elements. The Eulerian elements are constant volume elements where the grids are also constant. The material state at each point of the Eulerian domain is expressed by velocity, stress tensor, density and specific internal energy and they are related to each other through the conservation of energy, mass and momentum equations [88].

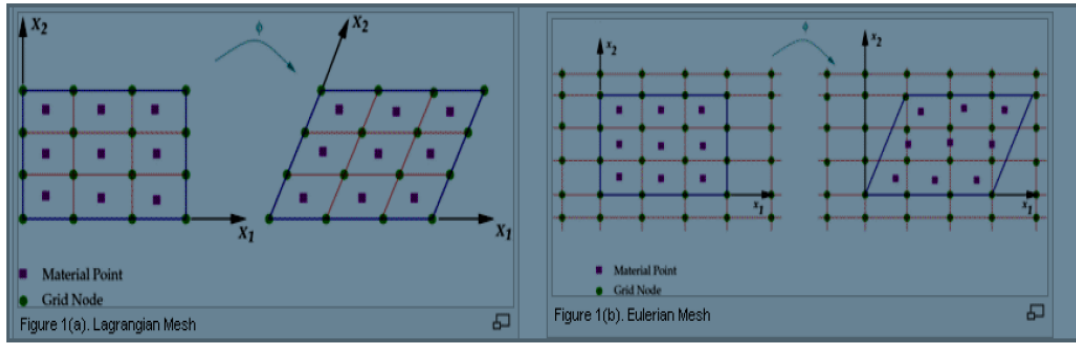


Figure 2.14 - Lagrangian description (a) against Eulerian description (b) [88]

Coupled Eulerian-Lagrangian (CEL) strives to combine the advantages of both the Lagrangian and Eulerian methods where the Eulerian material is tracked as it flows through the mesh by calculating the Eulerian volume fraction (EVF). The percentages assigned to each Eulerian element denotes the portion of that element filled with a material. For an Eulerian element with no material in it, it has EVF of zero (0) while a completely filled Eulerian material with materials has EVF of one (1) [85]. The method was initially developed to simulate the inflation of an airbag but was subsequently used for problems with impact loads and collisions. The CEL method involves mesh treatment, surface reconstruction as well as solving the coupled fluid and structure equations [87].

To establish the contact between Eulerian and Lagrangian materials, a general contact based on a penalty contact method is used. The penalty contact method is less severe compared to the kinematic contact method. To establish this contact, seeds are created on the Lagrangian element faces and edges while anchor points are created on the Eulerian material surface. The penalty contact method has the ability to approximate hard pressure-overclosure behaviour and also allows for small penetration of the Eulerian material into the Lagrangian domain. The contact force denoted by  $F_p$  which is enforced between the seeds and the anchor points is proportional to the penetration distance  $d_p$  in the expression shown in equation (2.43). Where  $K_p$  is the penalty stiffness which depends on the Lagrangian and Eulerian material properties. The Lagrangian elements can move freely through the Eulerian mesh without any restrictions until they encounter an Eulerian element filled with material [85].

$$F_p = K_p d_p \quad (2.43)$$

Generally, a Lagrangian frame is used to discretize the moving structure while the Eulerian frame is used to denote the fluid domain. The velocity of the Lagrangian boundary is used as the kinematic constraint in the Eulerian calculation by interface models [87].

CEL formulation can be used to efficiently model fluid structure interactions. The defined Lagrangian domain is responsible for the deformations of the structure parts while the Eulerian domain deals with the fluid part of the setup. It is possible to specify an all-inclusive surface or individual Eulerian surface in the contact domain with the Lagrangian surfaces.

However, contact interactions between Eulerian materials and interactions as a result of Eulerian material self contacts are naturally catered for by the Eulerian formulation [88].

To effectively use the CEL formulation, the following practices must be adhered to [88]:

- 1) The Bulk modulus (compressibility of the fluid) used should be very close to the actual value
- 2) The Eulerian mesh size to be used should be  $2/3$  times less than the minimum size of the Lagrangian mesh size. If the Eulerian mesh size is however equal to the minimum Lagrangian mesh size, the results obtained are altered infinitesimally.
- 3) During the creation of the discrete fields for the initial fluid fraction, the initial fluid core being modelled must represent exactly the initial fluid.

CEL is the only method capable of predicting accurately the resulting loads at limit states since the Eulerian mesh is not restricted by the mesh or element distortions. Also, CEL has the ability to simulate complex geotechnical problems that involves very large deformations [88].

## Chapter 3

# Biomechanical Simulation and Related Works

Due to the use of a transcatheter, non-invasive image acquisition of the patient anatomy is very vital coupled with pre-procedural planning based on high-resolution imaging techniques to assist in determining the safe puncture site and define the best puncture route.

This section is aimed at presenting an overview of the pre-planning procedure techniques mainly generation of patient-specific anatomical models as well as biomechanical simulation techniques. It also provides some work done with regards to simulations of the atrium and needle insertion.

### 3.1 - Biomechanical simulation

Novel computational or biomechanical models relevant to clinical practice has been achieved due to the recent advances in non-invasive high-resolution image acquisition techniques making it feasible to generate accurate patient-specific anatomical models.

Initially these novel image techniques were used to develop generic simulation models capable of providing useful anatomical information with respect to the atrial conduction system [89]-[92], motion pattern characterization [93], [94], study of different pathologies [95] and hemodynamics of the heart [96]. Since generic models were used without taking into account the individual information of each patient, the application of this proposed solution in clinical practice was limited. With time, a suggestion to develop complex methodologies resulting in the generation of accurate patient-specific models [97]-[101] was proposed. This model was aimed at effectively combining the above mentioned generic models with the patient-specific data acquired from either the multiple imaging techniques or clinical measurements.

Some notable instances are the proposed framework to simulate the procedure used to treat mitral valve (MV) regurgitation using a minimally invasive cardiac procedure as proposed by Mansi *et al* [101]. A patient-specific model of the MV was generated from an ultrasound image of which a finite element method was used to simulate the closure of the valve as well as the correction procedures. This patient-specific generated MV model was then tested on

eleven (11) patients and there was an average point-to-mesh error of  $1.47 \pm 0.27$  mm. The entire simulation framework was however tested on only one patient with results qualitatively very similar to the actual surgical outcome [101]. Furthermore, Stevanella *et al.* proposed a finite element model of the MV to predict the results of mitral annuloplasty procedures using an MRI data after which it was tested on two patients (one healthy patient and one sick patient) giving similar results compared with the real procedure being performed [102].

Soon, Wang *et al.* developed a patient-specific model to quantify and characterize the interaction between the trans-catheter stent and the stenotic aortic valve (SAV) [103]. The anatomic model of the patient-specific finite element model was generated from a computer tomography (CT) data applied as anisotropic hyperelastic material to simulate the tissue mechanical properties. An eight-node hexahedral was used to generate the solid element of the trans-catheter while a four-node quadrilateral element was employed to depict the balloon portion. This proposed method was implemented on one patient by simulating the entire valve-replacement procedure which was a success. The authors were able to prove by this that it was possible to use this approach to extract relevant pre-planning information and determining the stent position.

Furthermore, Morganti *et al.* also proposed a new framework to effectively simulate the trans-catheter aortic valve implantation [104]. A CT imaging technique was used to obtain the aortic model including the native structure of the valve (leaflets and calcific plaques). In the definition of the mechanical properties of the valve in the simulation programme, isotropic and homogeneous materials were used. Commercially available Edwards SAPIEN valve were used by the researchers to represent the prosthesis and generating its structure from a micro-CT image. Also, von Mises plasticity model with isotropic hardening was used to represent the mechanical parameters of the prosthesis being simulated. This was tested on two (2) patients and the obtained results suggested that; the proposed simulator could be used effectively for realistic minimal invasive procedure simulation, the associated risks of post-procedural complications mainly paravalvular leakage and the presentation of the patient-specific stress distribution of the aortic wall [104].

Lastly, Jayender *et al.* proposed an approach to estimate the optimal puncture location by successfully combining the pre-interventional models with a mechanical model of the catheter to be used for the LA intervention [56]. The pre-interventional models were obtained from CT image datasets through a semi-automatic strategy. The model of the catheter was pictured to be made of negligible rigid links along a backbone curve and in view of this, the optimal puncturing site could easily be predicted based on the thickness of the septal wall and the mechanical maneuverability of the catheter at all the positions of the LA. This model lacked exhaustive validation due to the fact that there are numerous types of catheters that can be used in this procedure (to puncture the septal wall) hence the need for different catheter models.

### 3.2 - Patient-specific anatomical models

Researchers have done so much to assist physicians throughout the pre-procedural planning by proposing automatic and semi-automatic strategies to generate patient-specific ana-



tomical models from imaging techniques such as CT, MRI and ultrasound. This section is aimed at investigating the patient-specific anatomical models of the atria.

Daoudi *et al.* presented a deformable model to segment the LA in 2D CT [105]. It begins with contrast enhancement based on adaptive histogram equalization followed by morphological operators and a region growing technique to generate a coarse contour to the LA chamber. Finally, a refining stage is done using gradient vector flow technique. Visual assessment of this method was tested on 20 CT datasets. It must also be noted that relevant clinical indicators were not extracted from these images due to the bi-dimensional segmentation performed.

Haak *et al.* also suggested a framework based on active shape models (ASM) for segmenting multiple heart chambers in 3D ultrasound imaging [106]. Ideally, ultrasound images show limited field-of-view (FOV) hence the wide-view ultrasound images were manually generated using several individual ultrasound records. These wide-view images were posteriorly semi-automatically segmented using the following steps: 1) estimation of the heart pose; 2) heart shape estimation; 3) refinement of the contours obtained in each chamber. Each step required a gamma mixture model to generate a blood-tissue probability map which was subsequently fitted with an ASM model of the heart chambers eventually generating the optimal contour. With regards to validation, the single ultrasound image and the wide-view ultrasound images were segmented using the abovementioned techniques which showed a reasonable improvement of Dice coefficient for the merged data.

Also, Almeida *et al.* proposed a semi-automatic strategy to define the LA chamber in the ultrasound image [107]. This framework was focused on the B-spline Explicit Active Surface (BEAS) which was initially proposed for the left ventricle (LV) segmentation in ultrasound and MRI data [108], [109] which resulted in a reduced computational time as well as an improved accuracy. Due to the LA not having a less regular shape compared with the LV an adaptation of the BEAS was required and implemented. This was then tested on twenty (20) volumetric sequences and the results proved that the LA functional parameters can be derived from the semi-automatic contours. It is worth noting that this technique has less validation.

Zheng *et al.* in a Siemens Corporate Research proposed a novel machine learning strategy to automatically segment the whole-heart in 3D CT volumes [110]. The proposed technique known as marginal space learning identifies the optimal heart pose through a classification approach. A 9-dimensional vector with position, orientation and scaling was used to train the classifier method and generate consequently a full parameter space with a large number of hypotheses as shown in Figure 3.1 below. During the testing stage, a multi-stage strategy was used to identify the optimal pose for each chamber. This technique starts with a restricted number of possibilities and increases the dimensionality of the problem in each stage. Finally, a mean shaped model of the heart was deformed until the estimated optimal heart pose was achieved and the final segmentation was generated as shown in figure 3.1. A total of 323 3D-CT volumes were used in the validation of the experiment presenting surface-to-surface errors lower than 1.6 mm for all the structures. A total of 2 seconds per volume were required with regards to the computational time [110].

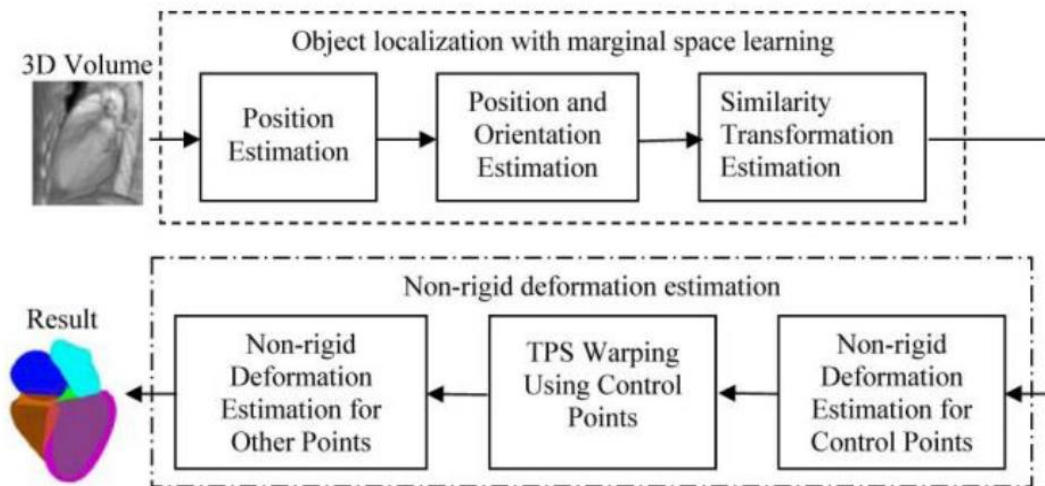
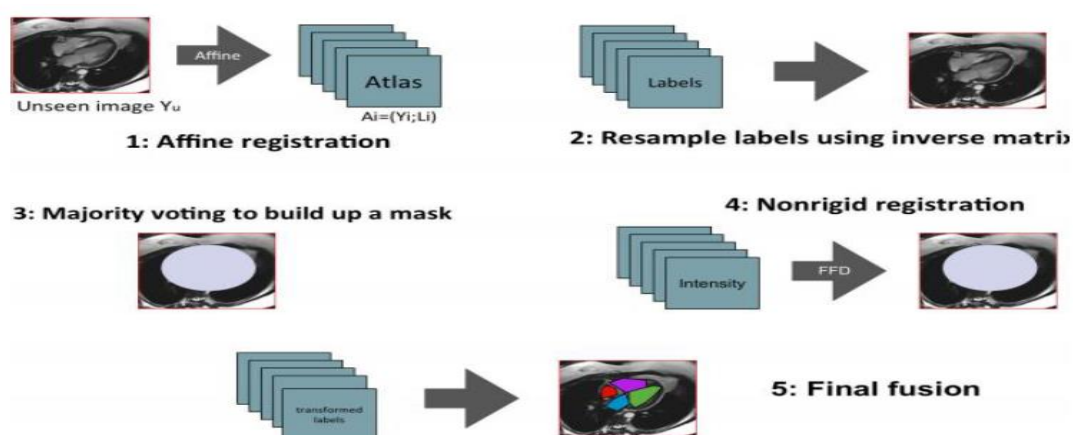


Figure 3.1 - Overview of the proposed technique by Zheng *et al.* [110]

Margeta *et al.* presented a supervised learning method for fully automatic left atrium segmentation from 3D cardiac MRI datasets based on machine learning techniques [111]. Blood-pool region extraction through a simple threshold commences this procedure but because intensity homogeneity was observed between the different chambers, multiple cardiac structures were detected. This technique was tested on 10 different databases using a leave-one-out approach and the results obtained showed an unsatisfactory dice coefficient lower than 70% indicating that this procedure was unable to delineate the entire cavity.

Zuluaga *et al.* focused on a multi-atlas approach to accurately segment the heart from 3D MRI and 3D computer tomography angiography (CTA) sequences [112] as shown in figure 3.2 below. The method uses two (2) steps; 1) localization of the region of interest (ROI) using affine alignment between the unseen image and the atlas as shown in (1) and (2) of figure 3.2. 2) The whole-heart segmentation based on non-rigid registration between the resulting ROI and the atlas as shown in (3-5) of figure 3.2 below. The obtained deformation fields were posteriorly combined to transform the labels from the atlas to the unknown image and consequently generate the final contour. This procedure requires a high computational time due to the set of non-rigid alignments required to delineate the final contour. It was tested on twenty-three (23) and eight (8) MRI and CTA datasets respectively and a resulting dice scores of 90.8% and 89% respectively for the whole-heart chambers were obtained making this procedure well valid. A total computational time of 30 and 60 minutes were required for the magnetic resonance (MR) and CTA datasets respectively.

Similarly, Kirisili *et al.* proposed a multi-atlas-based approach to segment the whole heart from CTA data. The current strategy was validated into a large-scale multicenter and multivendor study with a total of 1380 datasets [113]. A total of 8 labeled CTA datasets were used to generate the atlas. Evaluation of the results per the experts showed that 49% of the cases were very accurately segmented with an associated error below 1 mm while 29% were accurately segmented with an error between 2 and 3 mm. These results demonstrated the accuracy and robustness of this technique. Eight (8) fully segmented datasets were used to estimate the surface-to-surface error and the error obtained was lower than 1.5 mm for the various chambers even though a computational time of approximately 20 minutes per volume was used.



**Figure 3.2** - Schematic used by atlas-based approaches to segment MR images. It uses an affine registration (1) to roughly align the unseen image with the atlas. The obtained transformations are then posteriorly used to map the label images (2) into the unseen image and generate a region-of-interest through a majority vote strategy (3). Using only this region, a nonrigid registration (4) is used to align the different datasets. The resulting deformation fields are used to transform the labels and generate the final contour (5) [112].

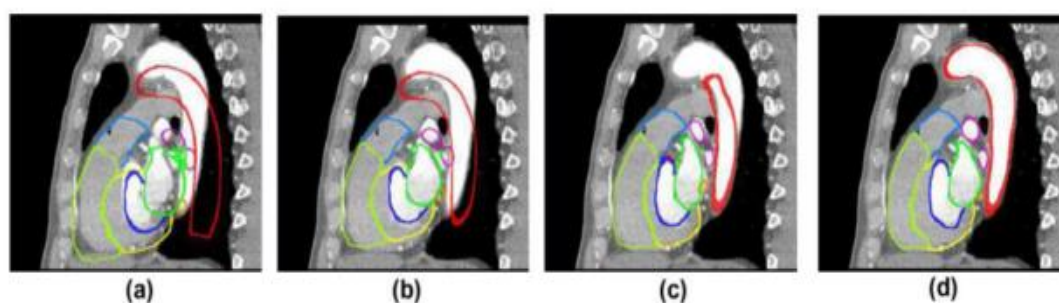


**Figure 3.3** - Ecabert et al. methodology: a) A rough contour is initially estimated through a generalized Hough transform approach. In (b) and (c) a global and local adaptation of the model is performed, respectively. Finally, in (d) a deformable model strategy is used to refine the contour [80].

Ecabert *et al.* presented a new strategy for fully segment the whole heart automatically in a 3D CT [114]. The proposed technique had two (2) main stages; 1) heart localization (figure 3.3 a); and 2) segmentation refinement using a deformable model (figure 3.3 b-d). The first phase which is the heart localization method was performed using an adapted 3D generalized Hough transform due to its high robustness and versatility to detect any arbitrary shape in the target image presented by using this procedure (figure 3.3 a). The second phase requires a shape-constrained deformable model being applied to refine the whole-heart mesh. Two alternating steps (parametric and deformable adaptation) were used to perform the refinement stage. Parametric adaptation starts with a global resizing (figure 3.3 b) of the mesh followed by a local adaptation of each contour (figure 3.3 c). The deformable adaptation was applied to basically guarantee optimal fit between the resulting mesh and the patient anatomy (figure 3.3 d). This approach was tested on 37 3D-CT datasets with a surface-to-surface errors less than 1 mm in all the cardiac structures and a computational time of about 22 seconds per dataset.

### 3.3 - Image-fusion and catheter tracking techniques

The pre-procedural planning data must be combined with the intra-procedural information such as image acquisition in order to safely guide the physician during the entire TSP procedure. This section gives an overview of image-fusion and catheter tracking techniques.

Cleary *et al.* in their research on image-guided interventions suggested the use of an external tracking hardware such as electromagnetic sensor or optical infrared systems [115]. These systems were coupled with the surgical catheter being used to combine the pre-procedural and intra-procedural data through series of markers. This procedure has a complex initial setup and the surrounding surgical equipment may generate electromagnetic interference.

Jeevan *et al.* also suggested the integration of electromagnetic (EM) sensors on the tip of the catheter based on the above described technique to assist and guide the TSP procedure [116]. The catheter was rigidly aligned with a patient-specific atria geometry obtained from a pre-interventional MRI. To validate this technique, it was tested on a phantom model and the results showed that it (procedure) reduces procedural time, it has no learning curve and also less complicated. It must however be noted that this testing was performed on static models without any real-time image acquisition such as x-ray or ultrasound imaging hence it can not be implemented in real life situations.

Also, Hatt *et al.* researched into an EM-tracking technique to effectively fuse X-ray, ultrasound and MRI images [117]. MRI is acquired during the planning stage whereas the X-ray and ultrasound are real-time imaging modalities that are required throughout the intervention. This proposed technique has two main pre-intervention calibrations which are firstly, the calibration between the EM and the ultrasound probe and secondly, the calibration between the EM world and X-ray image. In calibrating the EM and the ultrasound probe, two (2) EM sensors were coupled with the ultrasound probe and a surgical needle respectively. Ultrasound image acquisition of the surgical needle posteriorly was performed and the calibration was done using the difference in distance between the tool position into the ultrasound image and the actual distance measured by the EM sensor. The second calibration was done using two-custom-built phantoms with metal beads to calibrate the fluoroscopy image with the EM sensor. The difference between the metal beads measured through the fluoroscopy and EM sensor was used to determine the optimal transformation between these two systems. Fiducial markers were used to perform the intra-operative calibration of the MRI and EM system using a set of markers externally placed on the patient which are easily detected in the MRI image. The EM sensor was used to generate a 3D-world with the different position of these markers. The position differences measured through MRI and EM sensor were used to align the different worlds. This procedure was tested on a phantom and animal model with maximum accuracy error less than 5 mm [117].

Lang *et al.* proposed a new image strategy to register ultrasound, CT and fluoroscopy imaging without any tracking device in their research to assess accuracy [118]. This procedure involves: 1) alignment between the probe position and the transesophageal echocardiography (TEE) world using a calibration cage as shown in figure 3.4 (a) and 2) alignment between the probe position and the fluoroscopy world using a set of tracking beads coupled with ultrasound probe as shown in Figure 3.4 (b). This allowed a transformation that mapped the ultrasound world into the fluoroscopy world.

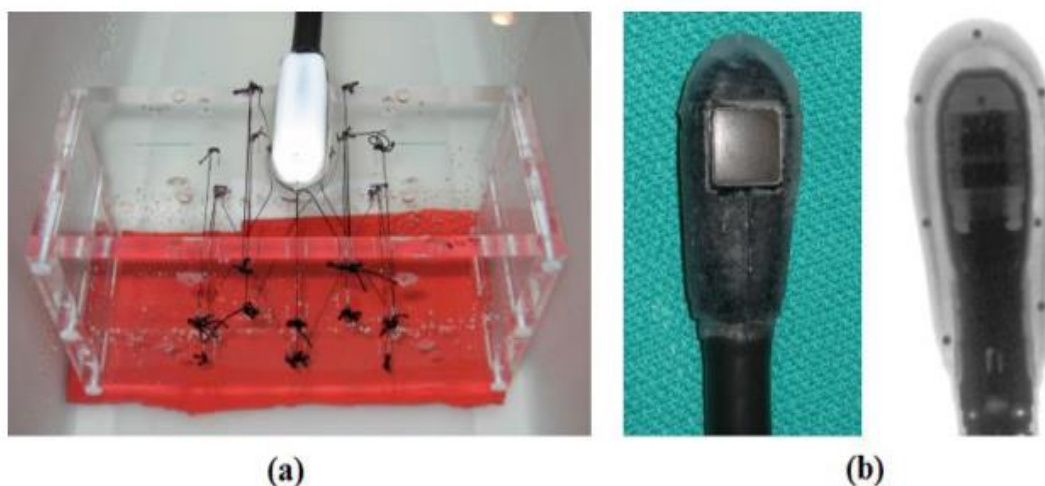


**Figure 3.4** - (a) Calibration cage used to align ultrasound world with probe position and (b) radiopaque markers to fuse X-ray and ultrasound world [118].

A semi-automatic segmentation is applied to delineate the relevant structure from the 3D CT data. Using an iterative closest point approach, a set of manual landmarks were used to register the obtained mesh. Since a transformation between the ultrasound and fluoroscopy worlds were obtained during the calibration stage, the patient-specific data acquired from the CT can be also transferred for the fluoroscopy world [118]. It was tested on excised porcine hearts datasets with an appreciable accuracy of 2.6 mm for tracked ultrasound to CT. It is however difficult to detect the required landmarks when using the ultrasound imaging hence high registration errors between CT and ultrasound can be attained indicating the fact that the proposed method is dependent on the user input and accuracy.

Housden *et al.* also proposed a technique to align CT, ultrasound and fluoroscopy images [119]. It involved an initial calibration between the probe and the TEE data through a calibration cage (Figure 3.5 (1)). A semi-automatic strategy was then proposed to align the fluoroscopy with the ultrasound worlds and a high-resolution surface model of the target structure was then generated after initial alignment. A manual segmentation of the esophagus centerline was created and included into the abovementioned high-resolution model. A simple downhill iterative optimization algorithm was used to align the high-resolution model with the ultrasound data (Figure 3.5 (2)) using the esophagus position to constrain the optimization.

Furthermore, Huang *et al.* proposed a different solution regarding the alignment of pre-operative data, 3D CT or 3D MRI with 2D ultrasound imaging [120]. A rigid transformation was used to spatially register both datasets while their time alignment was obtained using a simultaneously recorded ECG. A periodic heart motion was presumed ignoring the heart deformations caused by the respiration and surgical procedures since the procedure uses only rigid transformations. An accuracy of about  $1.7 \pm 0.4$  mm was obtained when this technique was tested on a beating heart phantom as well as animal models.

A strategy to align a 3D TEE data with fluoroscopy imaging was proposed by Gao *et al* [121]. This procedure commences with the automatic ultrasound probe identification on the X-ray image using a graphics processing unit (GPU)-based image registration between a 3D virtual model of the probe and the 2D fluoroscopy image. After this stage, a pre-interventional calibration of the ultrasound probe and the ultrasound image was done and a

transformation map between the fluoroscopy world and the ultrasound world can be obtained. A real heart phantom was used in testing this proposed method and the target registration error was lower than 2 mm. Later, an offline patient dataset was used and the measured mean registration error was between 1.5 to 4.2 mm. The probe estimation is a very time-consuming process of about 2 to 15 seconds thereby hindering their application in real-time procedures and hence failing to track the cardiac structure throughout the respiratory cycle. This procedure does not also have exhaustive online and offline validation [121].

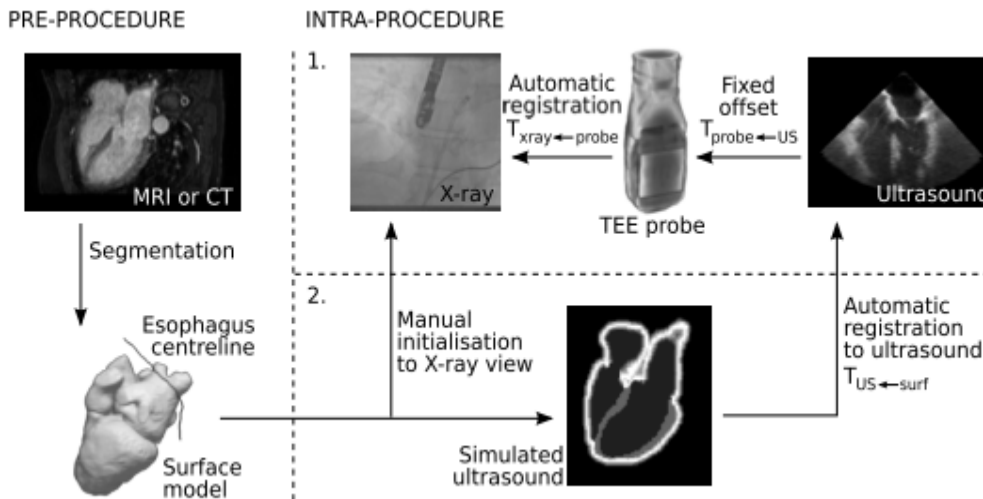


**Figure 3.5** - Workflow used to align MRI or CT, X-ray and ultrasound images. Pre-procedure phase; a CT or MRI image is acquired, automatically segmented and converted to a surface model. The esophagus centreline is manually segmented. During the procedure, an ultrasound volume is first acquired and registered to X-ray space via the TEE probe. The pre-procedure surface model is then manually positioned in the X-ray view before being automatically registered via the ultrasound image. The experiments in this paper evaluate intra-procedure stage 2 [119].

Lang *et al.* in their research to improve their previous proposal came up with a new method to align ultrasound and CT or MRI data. To perform this procedure, two different registration techniques were described and compared. These techniques are the surface-based registration and the image registration [122]. Surface-based registration relies on segmentation technique based on continuous max-flow algorithm to delineate the relevant structure in CT or MRI and ultrasound, followed by a mesh alignment based on ICP method. In the image registration technique, a non-rigid registration with mutual information metric was used to develop the image-alignment. Also, a GPU implementation of the tracking method was used. Registration error was lower than 2.5 mm, the dice coefficients were higher than 80% and a low computational time was obtained with surface and image registration approaches proving that both approaches have the potential to be used in image-guidance procedures after 18 datasets were tested. Catheter tracking techniques are required to identify the surgical equipment into the ultrasound imaging [122].

A different technique was proposed by Grbic *et al.* to align pre-operative 3D-CT and intra-operative rotational-angiography based on anatomical structure position [123]. The trachea bifurcation which is visible in both modalities without contrast is used to select surrogate anatomical structure. In view of this, a probabilistic boosting classifier is used to esti-

mate the global position of the trachea bifurcation of each image modality. A rigid-registration between the two meshes is performed in order to align the CT and rotational-angiography worlds. After testing the procedure on 28 patient datasets an accuracy of  $7.57 \pm 3.22$  mm was achieved.

A C-Arm technology can be employed to acquire 3D CT volumes and 2D fluoroscopy images that are intrinsically registered instead of using a multi-machine image acquisition. 3D CT imaging is only acquired in one temporal moment hence variations in the patient anatomy due to the insertion of the catheter were not accounted for. To resolve this deficiency, Liao *et al.* proposed a fully-automated solution to align the bi-dimensional X-ray images with the 3D datasets during the entire procedure [124] specifically procedures that emits agent contrasts. This procedure easily detects the contrast injection on the X-ray images based on histogram analysis as well as a possibility ratio test (likelihood ratio test). An optimized alignment on the basis of rigid transformation is subsequently performed between the contrast-based fluoroscopy image and a set of bi-dimensional (2D) digitally reconstructed radiographs (DRR) extracted from the 3D CT volumes using diverse plane orientations. After testing this technique on 34 datasets, a mean registration error of  $0.66 \pm 0.47$  mm and computational time of 2.5 seconds per alignment were obtained. It is still far off from being used in real-time procedures because it did not cater for the dynamics of the heart due to use of rigidly aligned static 3D volume.

All the above mentioned proposed techniques aimed at combining the pre-interventional and intra-interventional data did not take into account the surgical instruments used in this procedure making it difficult to implement them in real-time image-guidance procedures. Therefore, Brost *et al.* based their research on solutions to identify and track surgical catheter during fluoroscopy imaging to effectively assist the experts in numerous minimally invasive interventions such as catheter ablation and TSP [125]. A machine learning technique was used to segment the catheter structure and the authors presented a real-time strategy to identify the catheter through a cascade of boosted classifier combined with haar-features. A consecutive segmentation approach was employed in tracking the catheter after which the procedure was tested on 12 offline datasets and the obtained results showed a tracking error less than 0.7 mm [125].

In Buck *et al.* research, they proposed a novel technique to track the target catheter from X-ray images [126]. This procedure relied on a bi-dimensional template-matching obtained from a virtual 3D cylindrical model with a rounded tip projection coupled with Kalman filters to estimate the catheter tip in order to reduce the search space. This was also tested on about 14 fluoroscopy sequences and a maximum tracking error of 1.7 mm was obtained. Further clinical validations were performed on this technique and it was well accepted by the experts. However, this was short lived due to the introduction of multiple catheters which introduced more tracking errors.

Wu *et al.* solved the challenges faced by using ultrasound imaging to track and identify catheters by proposing a four-phase technique which includes:

1. Automatic or semi-automatic catheter identification in X-ray imaging based on speeded up robust features (SURF) and Frangi vesselness filter
2. Catheter tracking in X-ray imaging using Kalman filters
3. Fast registration of the X-ray and ultrasound imaging based on ultrasound probe position in the X-ray images

#### 4. Catheter segmentation/tracking in ultrasound images using the displacement field estimated in phase 2 [127].

This was tested on 5 porcine models and 4 patient datasets and the associated catheter tracking error was lower than 2 mm. The computational time was estimated to be 1.3 seconds per frame making it difficult to implement it in real-time procedures [127].

### 3.4 - Simulation of the atrium

*Moyer et al.* in their research on the changes in global and regional mechanics due to AF, constructed and validated a FEM model of the normal human left atrium using anatomic information obtained from cardiac MRI, iterative algorithm to estimate unloaded and material properties as well as fiber orientations derived from published articles. The FEM was then coupled to a circuit model to capture the hemodynamic interactions between the atrium, LV and pulmonary circulation [128]. This is to understand changes in atrial function by understanding how the accompanying systemic changes affect the atrium. The research was aimed at acquiring an in-depth knowledge of the role of the features of atrial remodeling known as the risk factors for future AF episodes by exploring the impact of changes in atrial size, shape, fibrosis, pressures and conduction velocity on the atrial mechanics. To construct and validate the FEM model, two sources of data were used. MRI studies of 10 healthy volunteers and 31 patients with paroxysmal AF in sinus rhythm during the period of a routine MRI prior to planned radiofrequency (RF) catheter ablation to obtain the average geometrics, volumes and regional wall motion throughout the cardiac cycle were used. An intra-operative pressure-volume data using Millar conductance catheter immediately prior to RF ablation [47] was additionally obtained from twenty-three (23) paroxysmal AF patients as well as six (6) healthy volunteers. The conductance catheter volumes were then calibrated against volumes from a pre-procedure MRI. FEM software FEBio v1.5 (Musculoskeletal Research Lab, University of Utah, Salt Lake City, Utah [129]) was used in the construction of the FEM model. The geometry were specified based on an average endocardial surface constructed from fits to contoured MR images of the 10 healthy volunteers [130]. A constant wall thickness of 3 mm, positioned midwall and epicardial nodes at equal distances from corresponding endocardial nodes along the local surface normal were employed and the resulting atrial mesh is shown in figure 3.6. Three (3) different mesh densities were used for preliminary simulations and they indicated that atrial volumes changed less than 5% between meshes of 19200 and 30000 elements [128]. From anatomic [131] and histologic [132] studies, the atrium was further subdivided into one posterior (bounded by the pulmonary veins (PV)) and four equatorial regions (lateral, inferior, septal and superior, each running between the pulmonary vein plane and the mitral annulus). The pulmonary veins were projected to be hollow cylinders of thickness 1.5 mm and diameter ranging from 4 to 6 mm [133], [134] composed of 200 hexahedral elements and oriented along the local surface normal. A thin ring composed of 80 elements were however created to denote the mitral annulus.



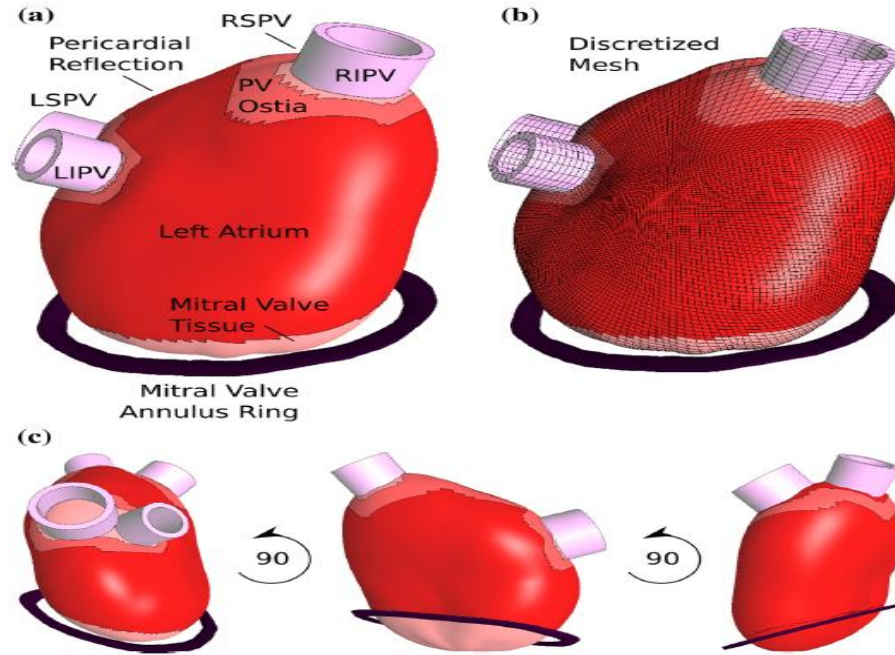


**Figure 3.6** - Geometry of the LA model at a pressure of 15 mmHg. (a) The four PVs denoted as right superior PV (RSPV), right inferior PV (RIPV), left superior PV (LSPV) and left inferior PV (LIPV). (b) FEM mesh with 30000 elements. (c) Different orientations of the model rotated in 90° [128].

The Bellini's strain-energy function available in the FEBio software was then used to generate the stress-strain curves for a range of biaxial test protocols to obtain the final material parameters for the atrial model. The boundary conditions of the setup were applied based on previous studies done or anatomical facts of the atrium and blood circulation and an example is prescribing a zero displacement of the pulmonary veins due to its ability to move only a few millimeters during a normal cardiac cycle [130]. The right atrial pressure was modeled as an inward-facing pressure on the epicardial face of the septal wall which was scaled to 30% of the left atrial pressure based on literature reviewed values [135]. An external pressure was then applied to the posterior wall where the atrium touches the chest wall. FEM employs stress-free configuration as its reference state but unfortunately this rarely exists in the human body. The unloaded geometry was estimated using an inverse displacement method similar to that of Raghavan *et al.* [136]. The circulation model was also constructed according to the cardiac circle where the atrium contracts and expands under varying chamber pressure. Based on Alexander *et al.* [137]., the atrial model was coupled to the hydraulic circuit model of the pulmonary vasculature, MV and LV. An exponential function (3.1) was used to model the passive properties of the ventricle as well as the atrial passive and active behaviours.

$$P_{LV,passive} = B_1 * (\exp(B_2 * (V_{LV} - V_{LV,0})) - 1) \quad (3.1)$$

Five (5) factors that changes in patients with AF and also might alter mechanics were investigated independently and they include: size, conduction, fibrosis, pressure and shape. The normal atrial model filled to a maximum volume of 66 mL, contracted to 27 mL at its minimum, emptied passively to 37 mL during diastasis. The predicted minimum and maximum volumes and their respective changes fell within a standard deviation of 1 of the measured in-vivo averages. Changes in the size and the pressure had the greatest effect on the function whereas changes in atrial shape and conduction had infinitesimal effects. Fibrosis simulation altered both the passive and active function but in a smaller degree compared

with that of the size and pressure. The modeled normal atrial was loaded with average pressures from literature instead of pressure measured simultaneously with wall motion and geometry and can be a cause for the variation in the results from the expected. Also, it is vital to note that the model doesn't reproduce diastasis accurately. The constructed and validated FEM model of the human LA was used to explore the impact of changes in atrial size, pressures, conduction velocity, shape and fibrosis. Also, the simulations of the model revealed that in these patients, dilation and increased pressures in the atrium are the most relevant factors affecting atrial function.

*Tobon et al.* [138] in their research on a three-dimensional human atrial model with fiber orientation, developed a realistic 3D computer model of the human atria to examine the relationship between different atrial arrhythmic propagation patterns and the electrogram (EGM) observed at different points along the atrial surface. Electrograms and their frequencies as well as their organizational index values were calculated over the entire atrial surface. This computer model of the human atria was the first model with realistic fiber orientation used to examine the relationship between the different atrial arrhythmic propagation patterns and the electrograms. Firstly, an anatomically accurate 3D model of the human atria was developed followed by the simulation of different tachyarrhythmic episodes in the electrically remodelled model of the atria. The 3D model consists of the LA, RA, twenty pectinate muscles (PM) in the RA free wall, the FO, crista terminalis, Bachmann's bundle (BB), left and right appendages (LAPG and RAPG), inferior and superior caval veins (ICV and SCV), the isthmus of RA, atrioventricular rings (AVR) as well as the coronary sinus (CS). This model also has three pathways for the inter-atrial conduction of electrical propagation as shown in figure 3.7.

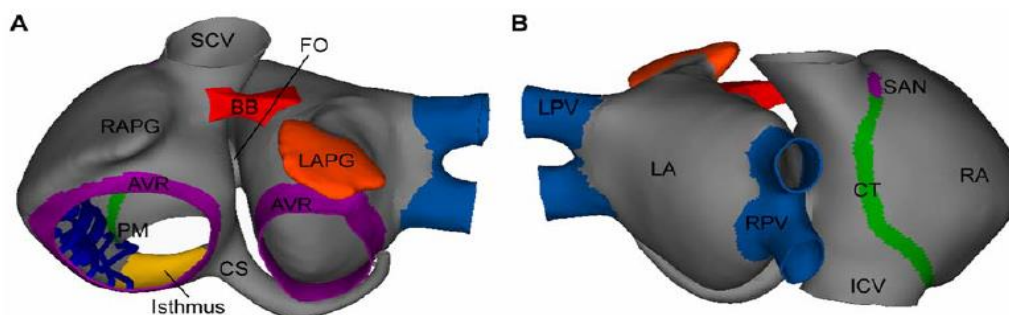


**Figure 3.7** - 3D model of the human atria. (A) denotes the frontal view while (B) depicts the dorsal view respectively [138].

Using the original set of surfaces of the model obtained from Harrild and Henriquez [89], the surfaces were then compared with the data from literature reviews of the human atria anatomy and histological observations [133], [139], [140] and the necessary modifications were done. The geometry and dimensions of the model were modified by creating the PV, APG, PM and AVR and the CS in accordance with the human data. After this process, the electrophysiological model was developed using the Nygren's model [141] of the human atrial action potential (AP) to reproduce the cellular electrical activity. To generate the APs in the different parts of the atria, the electrophysiological heterogeneity was introduced [142]. Changes in the maximum conductance and kinetics of the diverse ionic channels of the atria obtained from experimental studies [67] were incorporated into the AP models. It was observed that the atrial anatomy, anisotropy and fiber orientation are vital in determining the

spread and direction of the activating wave front [131], [139], [143]. The model represented the whole atria with highly detailed and simplified myocardial architecture which was obtained by dividing the model into 42 areas based on the orientation of the main muscle bundles to facilitate the assignment of a more realistic fiber direction to each region. The model also had a realistic RA-CS-LA interatrial connection; where the CS connects electrically the RA and the LA through some fiber tracks. The remodeling of this model however is based on experimental works performed by Bosh *et al.* [67]. The model also does not account for the real thickness of the atrial walls and the generated mesh is relatively coarse made of about 100554 nodes with a spatial resolution within the range of 300 to 700  $\mu\text{m}$ . The model has the ability to reproduce the stability and regularity that cause arrhythmias and areas with focal activity.

Harrild *et al.* [144] in their research into a computer model of the normal conduction in the human atria, developed a finite volume-based computer model of human atrial activation and current flow. The research was aimed at performing a comprehensive validation, investigation of the role of the well-defined atrial bundles in establishing the global activation sequence. The model developed was the first membrane-based 3D conduction model consisting of both the LA and RA as well as the major muscle bundles of the atria. It also comprised of the pectinate muscles, limbus of the FO, Bachmann's bundle and the crista terminals. A boundary-conforming mesh of the human atria comprising of hexagonal elements was constructed from an original set of surfaces used to control the generation of mesh obtained from Viewpoint Digital. The mesh generated consisted of 248264 elements as well as seven (7) constituent parts as shown in figure 3.8 below. The model also had two interatrial connections and provided a unique view of the atrial activation. The number of elements used in the various components of the mesh are scalable and the element sizes are ranged from 50 to 1650  $\mu\text{m}$  with a mean inter-element distance of 550  $\mu\text{m}$ ; 95% of the step sizes were smaller than 1060  $\mu\text{m}$ . It is worth noting that the largest elements were located in the left atrial appendage. This model was validated by comparing the simulated normal activation sequence and conduction velocities at various locations with experimental data and observations.

To represent the current flow, a monodomain and finite volume method were used to model the spatial spread of electric current with cell diameter of 11  $\mu\text{m}$  and surface-to-volume ratio of 3636/cm. Only three (3) conductivities were assigned to the model to limit the complexity and these conductivities had conduction velocities of approximately 60 to 70 cm/s in the bulk tissues, 200 cm/s in the bundles and 30 to 40 cm/s within slow regions. The Cuthill-McGee algorithm was applied to the sparse, symmetric positive-definite matrix bandwidth obtained from the application of the finite volume method to the block-structured grid. A first-order semi-implicit time integration scheme was used with a constant time step of 20  $\mu\text{s}$ . The conjugate gradient method with a convergence tolerance of  $10^{-6}$  was used to solve the system of equations iteratively. The simulation was performed to analyze the global conduction pattern in the model and for each case, the tissue activated at or before the indicated time. There are quite a number of well-defined uninsulated bundles within the atrial muscle for rapid current flow. These bundles are composed of the BB, limbus of the FO, pectinate muscles and the crista terminals which were meshed as discrete structures in the model and within the bundles, the hexagonal elements were aligned with their longitudinal axes which is very critical for the incorporation of anisotropy within the model. It must be said that the model was constructed based on a great number of assumptions and adjustments. The model was constructed using a monodomain formulation instead of trying to denote pre-

cisely the connections at the cellular level. This implies that there is still the need for a more realistic means of acquiring the anatomical features of the atria such as the thickness of the walls, the representation of the pectinate muscles to possess more branches and transverse connections. Relatively large elements have been used to ensure that the simulations are manageable hence limiting the discretization of the model since a finer discretization will be required to obtain the faster dynamics and sharper spatial fronts of the atrial membrane [144].

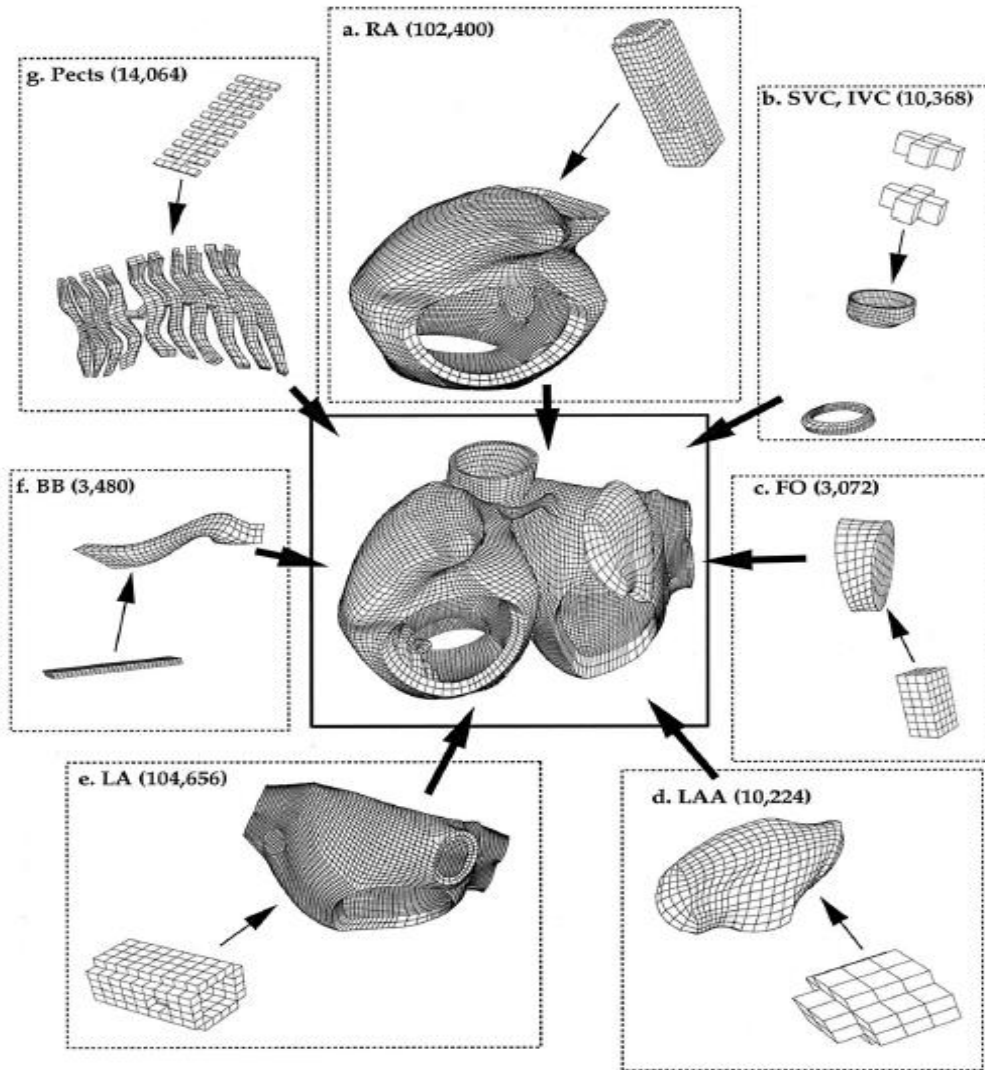


**Figure 3.8** - Block structure and low-density mesh views of the various components (from “a” to “g”) as well as the mesh of the entire model (centre) [144]

Corrado *et al.* in their research on personalized models of the human atrial electrophysiology derived from endocardial electrograms [145], proposed a novel method that characterizes regional electrophysiology properties. The tissue properties were predicted with the help of a 2D atrial tissue sheet model. Biophysical modeling gives a formal framework based on the understanding of the anatomy and physiology of the atria, the physical constraints as well as patient measurements to produce quantitative predictions of a patient’s response to treatment. The model characterizes the local cellular ionic properties, propagation of electrical activation across myocardial tissues and conductivity. A clinically tractable protocol

was developed to quantify local tissue properties. This research is basically in three main folds; firstly, the quantification of the accuracy of the model fitting protocol using in-silico data sets. Secondly, this fitting protocol is then applied to clinical measurements and finally, demonstration of the potential clinical utility of this approach using the fitted models to predict if characterized regions are potential ablation targets. A monodomain simplification was used to model the atrial tissue electrophysiology [146] and in order to simulate recordings from a decapolar catheter, a model of a 1D strip of the atrial tissue was created. The decapolar catheter electrodes were placed along the tissue strip. The monodomain equations were discretized in space with a first order FEM on a domain of length ( $L=20$  cm) with a discretization step of  $dx = 200$   $\mu\text{m}$ . Time discretization of the partial differential equations were performed using a semi-implicit backward Euler method shown in [147] and a constant time step ( $dt$ ) of 0.1 ms. The ionic model was selected to have the smallest number of parameters to limit its complexity to reflect the available clinical data. The Aliev Panfilov [148] and the Mitchell Schaeffer (MS) [149] are the simplest models of cardiac physiology with sharp upstroke and each model has four (4) ionic parameters and one (1) diffusion coefficient parameter. The atria were paced from the central poles of the decapolar catheter placed on the roof of the LA and the activation was measured distally, proximally and poles in a bipolar configuration. The Biotronik UHS 300 device simulator was also used during this research. Due to the curvature of the atria, it is impossible to guarantee good contact between all electrodes and the atrial wall at each location hence only one model is fitted to each catheter location. The error properties and robustness of the approach were evaluated firstly by generating a set of 247 models by randomly choosing parameter values within given intervals. This was then followed by generating a set of 1000 random parameter sets and then considered only combinations that had 1:1 capturing. This research was aimed at providing a robust and clinically feasible protocol and fitting algorithm for characterizing local atria tissue electrophysiology properties using an ionic model. There was no comparison of the relative accuracy of the different fitting approaches because no error estimate was presented in the earlier studies. The clinical measurements were characteristically noisy and the model did not cover the atrial curvature that affects wave propagation. Only limited number of patient cases were used making it difficult to conclude that the distinct tissue types identified were relevant to the general AF population. Furthermore, the model does not give a complete description of the atrial myocyte physiology as well as the cardiac memory [150].

### 3.5 - Simulation of needle insertion

Abolhassani *et al.* researched on needle insertion into soft tissues due to its application in minimally invasive procedures [5]. In their research, they observed that percutaneous procedures are constrained procedures where visibility of the target, access to target and ability to maneuver coupled with physiological variations are vital issues. Some conventional needle insertion processes require the surgeon to rely on kinesthetic feedback from the tool being used (either catheter or needle) as well as his mental 3D visualization of the anatomical structures [151]. The visibility of the target can be improved by the use of real-time imaging techniques. Human errors [152] (usually attributed to poor techniques and inexperience of the surgeon), target uncertainty (usually related to geometrical and/or physiological prob-

lems), imaging limitations [11], needle deflection (associated with bevel tip, needle diameter and the tissue being penetrated by the needle) as well as tissue deformation (caused by the needle tip contact force and the frictional forces between the tissue and the needle shaft) are the well-known contributors to needle misplacements during percutaneous procedures. There are several factors that generally restricts the use of diverse imaging modalities to enhance the visualization of targets during clinical and research processes and they include: poor resolution, high cost, radiation exposure, biocompatibility as well as the reliability of real-time processing techniques. The use of medical imaging plays a crucial part in image-guided procedures, however, numerous research has shown that offline medical imaging does not enhance the accuracy of the procedure. This points to the fact that real-time imaging techniques are very important in achieving the desired accuracy associated with these procedures. Several modeling and simulation of needle insertion have been performed in 2D and 3D platforms both for generic and specified applications. To be able to effectively model and simulate this process, the boundary conditions, tissue geometry and biomechanical properties are very vital since they determine or affect the degree of tissue deformation, force of interaction as well as the extent of needle deflection. In this review, the needle insertion procedure has been demonstrated in several stages shown in figure 3.9 below. Both visual and haptic feedback are necessary indications to improve the clinical procedure when a needle is inserted percutaneously. The data obtained from both visual and haptic feedbacks give adequate information about tissue deformation and needle deflection during the needle insertion process and are very vital in the modelling process. Visual data acquired can be processed and used in image-guided procedures while models obtained from both visual and haptic data can be used to generate intra-operative path planning, route generation and improve of-line planning and simulations.

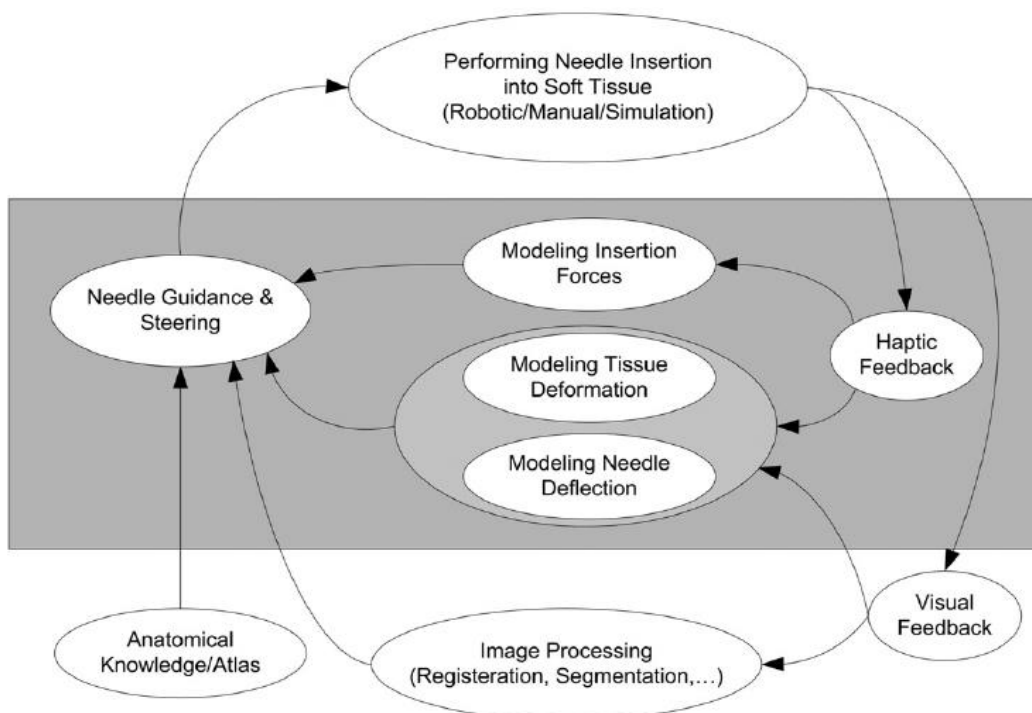


Figure 3.9 - Block diagram of needle insertion procedure [5]

An adequate knowledge of the interactive forces during needle insertion is very vital in obtaining a safe and precise needle insertion which helps to identify and model the diverse layers of the tissues as well as the various types of tissues adequately. It also helps to limit tissue deformation and needle deflection. Special characteristics such as the force peak, separation of different forces, the latency in the force changes as well as calculation of the magnitude of the insertion forces can be evaluated and compared with the actual measurements to assist in generating an accurate model. During percutaneous procedures, the needle punctures and traverses diverse tissue layers including the skin, muscles, connective and fatty tissues before reaching the desired target and each of these requires a different amount of applied force. It must be noted that these forces also vary from patient to patient due to other factors such as age, gender, body mass just to mention but a few.

Maurin *et al.* [153], in their studies on insertion forces during in-vivo needle insertions into the kidney and liver of anesthetized pigs compared the manual and robotic insertions. The manual insertion did not utilize an imaging system and the radiologist inserted the needle manually by holding the force device attached to the needle whereas the needle holder was attached to the end-effector of the robot for the robotic insertions. For the manual insertion, the needle was inserted for approximately 30 to 50 mm while the robotic insertion had a fixed insertion depth of 20 mm. Two main methods were used to access the target organ; a) “direct access” where all other anatomical layers were removed and b) “with skin access” where the needle passes through different anatomical layers. The results obtained indicated that the different layers associated with the “skin access” emphasized the forces. Also, the results showed that the robotic insertion required lesser force compared to the manual insertion during the “with skin access” procedure.

Due to the nonlinear, inhomogeneous, anisotropic, elastic and viscous nature of soft tissues, it is very complicated to model tissue deformation during needle insertion. To be able to effectively model the soft tissue, there is the need to do the following: determination of the biomechanical properties through in-vivo and in-vitro measurements, the use of constitutive laws and development of FEM or spring-mass models for real-time simulations [5]. The constitutive laws used for tissue modeling are based on nonlinear stress-strain relationships, viscoelasticity, nonhomogeneity, anisotropy and large deformations [5]. For nonlinear stress-strain relationships, the force is not linearly proportional to the displacement. Viscoelasticity, nonhomogeneity and anisotropy means that soft tissue properties are functions of time, varies through out the tissue thickness and also vary in direction. There are no closed-form solutions for a number of these problems. The mass-spring models and FEM are the current solutions for modeling tissue deformation not forgetting their limitations. Mass-spring models may work in real-time processes but are less accurate [154] while FEM is accurate for modeling small linear elastic deformations. DiMaio and Salcudean [151], [155]-[157] in their studies on simulation of tissue deformations that occur during needle insertion in soft tissues, developed a real-time haptic simulation system that provided both visual and kinesthetic feedback to the user while performing a virtual planar needle insertion. They also described tissue deformation using FEM as shown in equation 3.2 where “K” denotes the system’s stiffness matrix, “u” and “f” are the displacement and force vectors respectively for nodes resting on the finite element mesh. The boundary conditions were only applied to the nodes in direct contact with the needle shaft and thus the associated deformation was calculated for the working nodes.

$$Ku = f \quad (3.2)$$

Alterovitz *et al.* [158]-[160] provided a 2D FEM model and simulation of needle insertion using a prostate brachytherapy. The mechanical properties of the soft tissues such as the Young's modulus and Poisson's ratio were obtained from datasets obtained as results from research conducted [161]. The FEM was assumed to be made up of linearly elastic homogeneous materials. The needle insertion forces were applied as boundary conditions on the elements by assuming that the puncturing membrane tissue required additional force at the needle tip. They noticed that increasing the needle insertion velocity resulted in smaller deformation and thus decreased the seed placement error. It is worth noting that the velocity can however not be set high as a result of safety issues and path verification during the insertion process.



## Chapter 4

# Simulation Methodology

This chapter gives detailed information about the mechanical properties of the human atria, the geometry of the needle, cardiac muscle, soft tissue as well as the steps and methods used in modelling the needle, cardiac muscle and tissue for the project. Many researches have been conducted with regards to the mechanical properties of the biological tissue systems as well as in-vitro measurement of soft tissues [162]-[164]. There has been an extensive use of tissue phantoms in medical imaging studies and reviews with the assistance of water-based materials such as agar and gelatine. These materials are noted for their excellent properties for MRI, X-Ray and ultrasound experimental procedures but are mostly inappropriate for numerous applications that require physical needle insertions as done in this dissertation. This is due to the fact that both materials possess little resistance to puncture [165]. In view of this, recent motivation has been on acquiring quantitative details from the in-vivo biomechanical properties of the soft tissues. This section is however focused on reviewing existing articles on the mechanical properties of the human atria to obtain the needed mechanical properties which will help in the development of the FEM model of the human atria.

### 4.1 - Mechanical properties of the human atria

Schwartzman *et al.* [134] researched to examine the dimensions and morphology of the LA and distal PVs using a multidetector helical computed tomography (MDCT). Most heart related diseases are dependent on the LA and PVs for its initiation and sustenance. A more detailed and accurate morphology and dimensions of the LA and PVs will play a vital role in the development of a more specified FEM models. The MDCT was used because it permits multidimensional reconstruction [166]. A total of 117 subjects divided into two groups were used to perform the MDCT procedure. The first group consisted of 70 subjects who had either paroxysmal or persistent AF hence given the name AF group. The second group known as the no-AF group had 47 subjects without AF. The images were acquired using the General Electrical Lightspeed scanners and iodinated contrast was used in a test dose to determine the peak LA filling moment. The acquisition period was 25 to 30 seconds. After the acquisition process, the commercial General Electric software was used for the image reconstruction

process. The other structures were eliminated by taking into account and editing the shape, density, continuity and sequential axial images to obtain just the LA and the PV. By combining these images, the multidimensional reconstruction was obtained as extra-atrial and intra-atrial as shown in figures 4.1 and 4.2 respectively. Echocardiography and EGMs were subsequently used to assess the accuracy of the MDCT technique. The point of reflection of the parietal pericardium is known as the AV junction or the pulmonary vein ostium. The ostial branch is a PV branch joining within 5 mm of the AV junction and the saddle is the area of tissue interposed between intervenous or intravenous branches. The common vein is the combination of the inferior and superior veins proximal to the junction with the LA body.

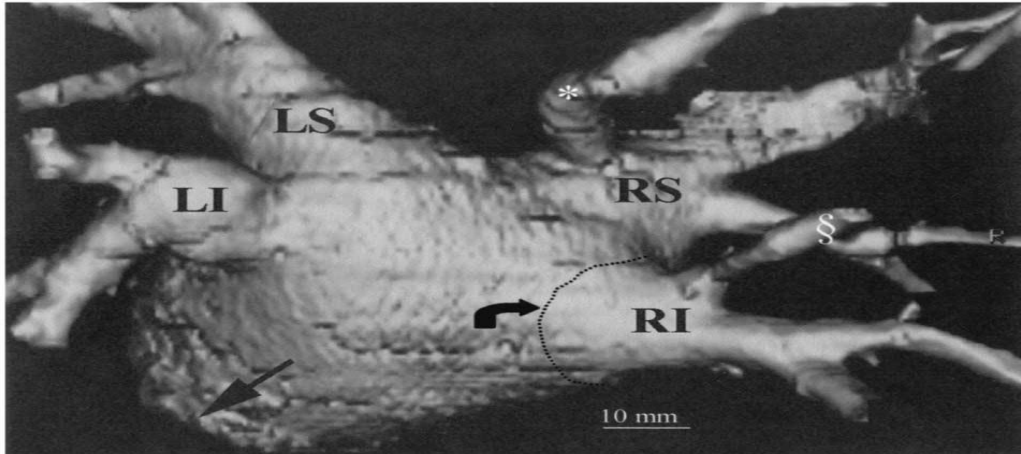


**Figure 4.1** - Extra-atrial MDCT view. The right inferior ostium is denoted by the dotted lines whereas the straight arrow denotes the region of the AV groove. \* represents the sharp angulation in the vein. SA is the region where branches of separate veins have direct spatial contiguity. LI is LIPV, LS is LSPV, RI is RIPV and RS is RSPV [134].

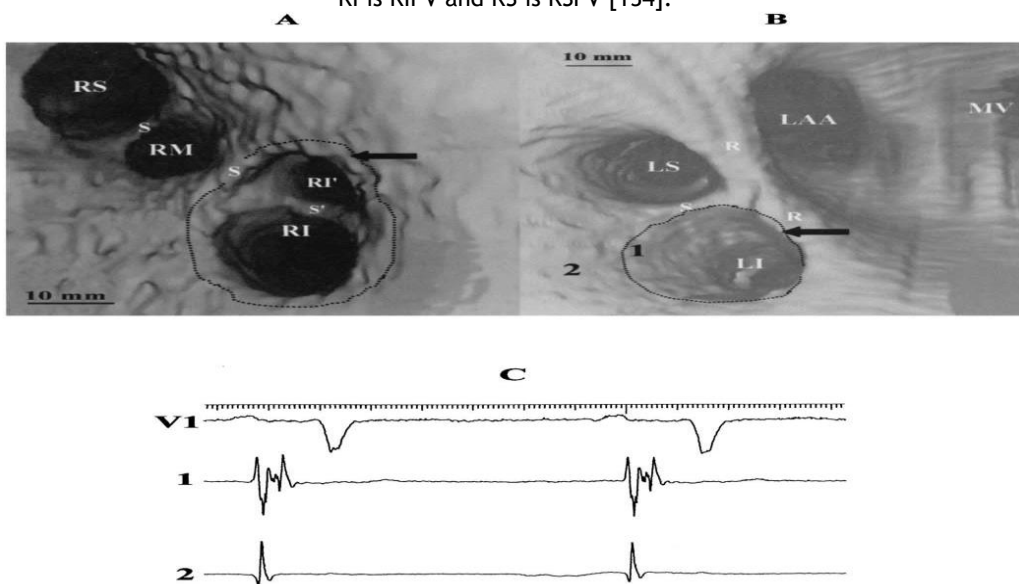


**Figure 4.2** - Intra-atrial views of the posterior LA and PV regions. (A) Right superior (RS), right inferior (RI), right middle (RM) vein ostia. RI' is the ostial branch of the RIPV. S and S' denotes intervenous and intravenous saddles respectively. Dotted lines denote the AV junction. (B) Left superior (LS), left inferior (LI) vein ostia, ostium of the appendage (LAA) and a section of the posterior MV leaflet. It also shows the ridge between the vein inflow region and the appendage ostium (R) as well as LI ostium represented by the dotted lines. (C) Electrograms recorded from the area in B with the corresponding number [134].

The supernumerary vein is an additional vein which is neither superior nor inferior having an independent AV junction. The echocardiography and the generated MDCT LA volumes were adequately correlated using the Spearman test. It was observed that the superior vein ostial circumference was significantly bigger than the inferior vein circumference. There were however no clear-cut differences between the corresponding left and right veins. The aggregate pulmonary vein circumference ( $r = 0.43$ ,  $p < 0.001$ ) and aggregate maximal diameter ( $r = 0.48$ ,  $p < 0.001$ ) were both correlated with the LA volume. Also, aggregate pulmonary vein circumference ( $r = 0.23$ ,  $p = 0.01$ ) and aggregate maximal diameter ( $r = 0.29$ ,  $p = 0.001$ ) were correlated with the LA maximal planar diameter. Below are the morphological observations in both the AF and no-AF groups:

1. Supernumerary veins were common on the right particularly draining the middle lobe and were barely observed in the left.
2. Higher PV ostial branching on the right and more common in the inferior vein compared to the superior.
3. The average ostium-to-first branch distance in the left vein was emphatically bigger than that in the right veins.
4. There was a common PV occurring frequently on the left but the same was not observed on the right.
5. Veins could be sharply angulated as shown in figure 4.1 above.

Most of the measured dimensions and volume of the LA were greater in men as compared to women. However, the PV ostial dimensions before and after the correlation for the LA volume were similar for both men and women. Also, there were no distinct differences between men and women in relation to the vein multiplicity, ostium-to-branch distance, saddle length and ostial branching. Subjects with persistent AF had significantly greater volume and dimensions of the LA compared to those with paroxysmal. The accuracy of the MDCT images were reinforced by the correlation with echocardiographic and electrographic indices. It is vital to note the complexity and heterogeneity of the LA and PV anatomical structure.

Siew *et al.* in their research on the anatomy of the LA [133] reviewed the structure of the LA through the examination of the septum, pulmonary veins insertions into the heart as well as the appendage. A total of twenty-six (26) heart specimens were examined of which seventeen (17) were males and nine (9) were females within the ages of twenty-five (25) and eighty-five (85) years. Twenty-five (25) of the hearts used were normal structurally and were obtained from patients who died without cardiac diseases. The weight of the hearts ranged from 350 to 512 grams (g). Calipers were used to internally measure the dimensions of the left atrium as well as the pulmonary veins. The diameters of the veins were measured at the venoatrial junctions. The orthogonal dimensions of the atrial chamber were measured as longitudinal (measured from the level of the mitral orifice to the dome of the atrium at the mid-point between the four pulmonary veins), anteroposterior (the distance between the middle of the posterior wall and the middle of the anterior wall) and transverse (minimal distance of a line that extends between the left and right pulmonary veins of the orifices). To effectively dissect the LA, the epicardium and endocardium were peeled away from the outside and inside respectively leaving the muscular bundles of the LA. LA is regarded to consist of four (4) components: the appendage, septum, vestibule and venous components. Observing from the right atrial aspect, the atrial septum is made of the flap valve of the oval foramen coupled with its immediate inferior muscular rim. The rest of the structures are composed of infolded right atrial wall inferiorly and superiorly as well as the fibrofatty sandwich of atrial and ven-

tricular musculature anteriorly. The atrial myocardium of the vestibules covering the inferior AV groove resting on the crest of the muscular ventricular septum comprises the sandwich. The muscular fold creating the rim of the oval foramen is filled with fibrofatty tissues of the epicardium as well as artery which supplies the sinus node. Examining from the left atrial aspect, the flap valve of the oval foramen represents the site of atrial septum. The crescent-like edge in most hearts relates to the anterior atrial wall on its epicardial and not the septum. The vestibular components however are the smooth circumferential area surrounding the orifice of the MV. The atrial wall is thin posteriorly and parietally overlies directly the cardiac vein through the left AV groove. The vestibular wall is thin and tapers where it dismisses over the MV. Unlike RA, the LA wall is generally smooth and without array of pectinate muscles which are mostly found in atrial appendage. The junction between the appendage and the venous component is connected by a narrow mouth. A large portion of the LA is made of the venous component receiving the pulmonary veins. In accordance to McAlpine's research [167], the walls of the LA can be described as superior, posterior, left lateral, anterior and septal excluding the atrial appendage. The anterior wall which is located behind the transverse pericardial sinus is very thin and measures an average of about 2 mm in thickness in the area close to the vestibule. The superior wall has a thickness between 3 and 6.5 mm as shown in table 4.1. Also, the longitudinal, anteroposterior and transverse dimensions of the LA are  $4.5 \pm 1.4$  cm (range 3.4 to 6.2),  $3 \pm 0.8$  cm (range 2.4 to 4.3) and  $4 \pm 1.2$  cm (range 2.6 to 5.5) respectively [133].

**Table 4.1** - Thickness of the LA walls as measured in 26 hearts [133] showing the median  $\pm$  standard deviation and (range) in millimeters.

<b>Anterior</b>	<b>Posterior</b>	<b>Superior</b>	<b>Lateral</b>	<b>Vestibule</b>
$3.3 \pm 1.2$	$4.1 \pm 0.7$	$4.5 \pm 0.6$	$3.9 \pm 0.7$	$2.3 \pm 0.7$
(1.5 - 4.8)	(2.5 - 5.3)	(3.5 - 6.5)	(2.5 - 4.9)	(1.2 - 3.3)

The macroscopic appearance of the strands of the myocytes that provides the atrial wall with its grain-like appearance are said to be fibers because they are circumferential when they are parallel to the plane of the mitral orifice and longitudinal when aligned at right angles to the orifice. In most of the specimens, the epicardial fibers of the LA were observed to have a common pattern even though there were few differences. Anteriorly, the pattern consisted of a main bundle parallel to the AV groove due to the interatrial bundle. In the LA, the interatrial bundle was inferiorly joined at the septal raphe by fibers generating from the anterior rim of the oval foramen. Superiorly, the interatrial bundle blended with the circumferential fibers arising from the anterosuperior part of the septal raphe. The LA has no terminal crest and its pectinate muscles are mostly found in the atrial appendage hence they (LA) are considered to be structurally simple compared to the RA.

Accurate atrial structures and location is very paramount in the successful execution of the TSP procedure by eliminating the risks of damages caused by the procedure [139]. The LA is seen to have relatively smooth walls and small tubular-shaped appendage compared to the RA which is predominately made of appendage. Ho *et al.* [139] in their research to determine the importance of atrial structure and fibers summarized the 3D arrangement of the atrial structure and differences in the muscular interatrial connections. The rapid enhancements of the TSP procedure have led to the eminence of the atrial compartments for effective treat-

ment of heart-related diseases. Both LA and RA have some identical anatomical parts such as the venous portion, vestibule which leads to the AV valve and the appendage as shown in figure 4.3 below.

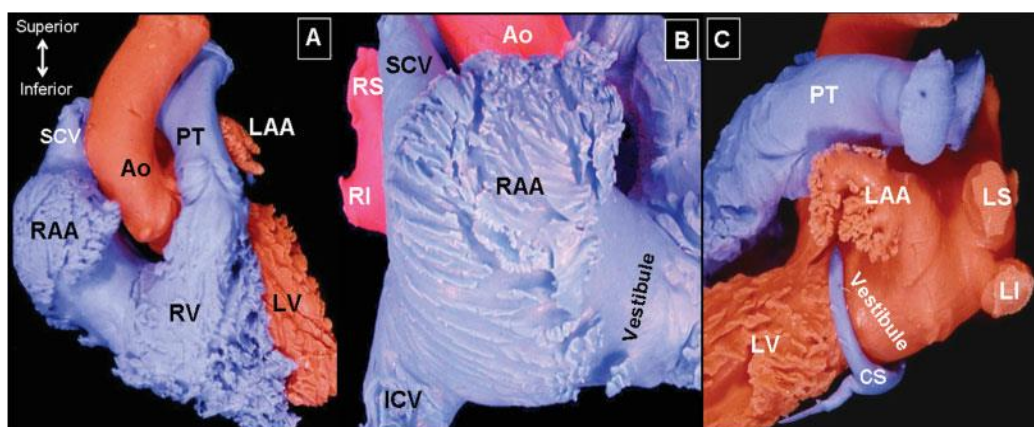
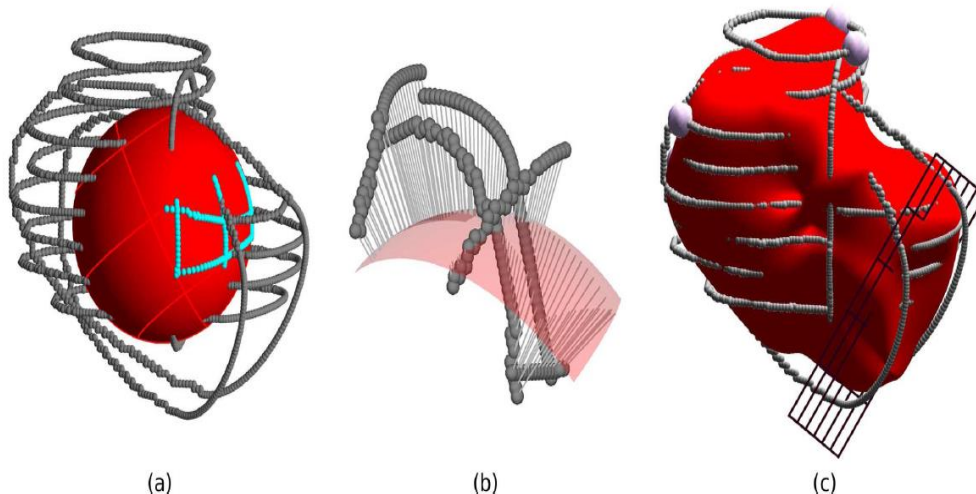


Figure 4.3 - An endocast from a normal heart showing the arrangement of components of the atria as observed from (A) the front, (B) the right and (C) the left [139]

The LA is predominately made up of appendages and they are relatively smaller and tubular in shape with one or several bends like a little finger [168] as shown in figure 4.3 (c) above. The rough part of the LA is embedded in the appendage. The endocardial characteristic has complicated network of fine muscular ridges lining it with a parchment wall in between the bridges. The body of the LA joins together the septum, venous part and vestibule. The venous part is the posterior part of the LA collecting the pulmonary veins and can be found immediately in front of the oesophagus and the fibrous epicardium separates the two [169]. The endocardial surface of the LA looks like ridges in between the superior and inferior venous orifices. The vestibular part of the LA denotes the LA outlet. In as much as the LA have smooth walls, they do not have uniform wall thickness. The Bachmann's bundle is a broad muscle bundle that runs along the anterior atrial and it is made up of myofibers aligned parallel to the plane of the AV junction. The interatrial muscular connections are made of atrial myofibers and have diverse lengths, widths and distance to the rim of the FO [133].

Moyer *et al.* [130] in their research to evaluate regional and global mechanical functions using cardiac MRI as well as finite element surface fitting. A total of 23 healthy volunteers as well as AF patients were used for this research. A new approach to measure the regional mechanics was generated by fitting the data obtained from the cardiac MRI to create a continuous surface denoting the LA endocardium in time and space. FEM was used to generate the endocardial surfaces mainly to break a continuous body into elements connected together by nodes. These elements were then fitted to the image-derived data points. The use of this method in any procedure or work have concerns such as: rigid-body motion assessments, scaling of nodal parameters within the elements, accurate and quick optimization of the nodal parameters, assigning of data points to locations on the mesh to mention a few. It is worth noting that based on the structure and application of the procedure, these challenges can be addressed differently. The research was the first application of finite element fitting as well as analysis of wall motion to quantify 3D mechanics in the LA. Of the 23 subjects used, 9 were healthy while 14 were AF patients. The steady-state free precession (SSFP) imaging technique was used using a median flip angle of  $71^\circ$ , repetition time of 39 ms and an echo

time of 1.4 ms. The slice used had a 6 mm thickness and a single slice was obtained in the coronal and sagittal planes together with two chambers of the left vertical long-axis and four chambers of horizontal long-axis planes relative to the heart. Approximately, 15 to 20 axial images were obtained to be able to have a detailed representation of the LA. The field of view is dependent on the imaging plane being used but it was about 300 X 300 mm and had a pixel size of about 1.2 X 1.2 mm and a RF bandwidth of 930 Hz/pixel. Cardiac MRI were contoured manually by the help of the ARGUS software. A standardized contouring process was developed to curb inter-operator variations. The coronal imaging plane was used to detect the left superior pulmonary vein while the lateral and septal mitral valve points were detected with the help of the horizontal long-axis plane. Due to the approximately spherical shape of the LA, spherical coordinates  $(\theta, \varnothing, r)$  were used. The endocardial surface was denoted by a FEM mesh with varying radius as a function of space and time expressed as  $r = r(\theta, \varnothing, r)$ . The element coordinates were represented as  $(\xi_1, \xi_2, \xi_t)$  with 0 to 1 being the ranges mainly determined by the relative location of any point within the element. The cubic Hermite basis functions as well as the Lagrange interpolation were employed to interpolate the radii in the two spatial dimensions  $(\theta, \varnothing)$  since the coefficients denotes physically meaningful parameters. The spherical surface of the LA was alienated into 16 elements equally spread out in  $(\theta, \varnothing)$ . A 7<sup>th</sup> order temporal fit was then used to capture the complex LA emptying pattern. The element was designed to have 32 nodes while each node also contained 4 nodal parameters hence generating 128 nodal parameters. The total 16-element mesh (u) has 160 nodes as well as 640 nodal parameters. With the application of the constraints, the independent nodal parameters were reduced to 432 to generate the initial mesh being a static sphere having a constant radius as shown in figure 4.4 below.



**Figure 4.4** - The generation, projection and optimization of the mesh. (a) the 16-element static spherical mesh (red) (b) projections along the fitted radius onto the surface (gray lines) (c) optimization of mesh parameters [130].

An artificial MV was then introduced to standardize the behaviour of the fits close to the MV orifice before the projection of the data points onto the FEM mesh was performed. Contour points that fell beneath the MV plane were replaced with artificial point sets and in the bid to promote the smooth boundary, the position and direction of the LA wall immediately adjacent the annulus were used to create the cap. All data points were projected radially

onto the FEM mesh by assigning points of elements based on their coordinates ( $\theta$ ,  $\varnothing$ ,  $t$ ). This process was followed by the implementation of the scaling factors where the data points were plotted onto the mesh made of elements with normalized coordinates ranging from 0 to 1. The scaling factor is known to be a property of the element and also scales the nodal parameters bordering the element. Each element dimension was scaled based on its global space occupied as well as the cross-derivative term. As a result of using a spherical surface to denote the atrium, the nodal radii were constrained to be equal to the nodal derivatives in relation to the zenith angle ( $\varnothing$ ) to be the negative of the derivative of the opposite side of the given pole. To ensure optimization, Newton's method was employed to detect nodal parameters providing the best fit of the model surface using the following components: creation of error minimization function, imposing of surface smoothing penalties, ensuring the use of the relevant parameter constraints, building of objective function and finally, the calculation of the relevant gradients and Hessian matrices. Numerical integration was employed to calculate the LA chamber volume of the fitted surface where the axial volume was computed as the reference through the sum of the axial contour area. Fractional volume changes were calculated by normalizing the chamber volumes to the maximum value while the fractional radii changes were computed using fractional shortening. The data sets used converged to a tolerance of  $1 \times 10^{-10}$  in the range of 1.4 to 3.4 having a root mean square error (RMSE) mean value of  $2.3 \pm 0.5$  mm. Also, the fitted regional radii ranged between 10 to 42 mm and a mean of 26 mm. The maximum atrial volumes detected at the end of the atrial filling process ranged from 42 to 180 mL and a mean value of  $91 \pm 29$  mL [130].

## 4.2 - Needle geometry and modelling

One of the commonly used medical devices employed in diverse medical procedures are needles [170] and there are currently numerous configurations of the needle tips depending on the purpose for which it is being used in the medical procedure [170], [171]. The most utilized needle tip for biopsy [5], vessel access [172] as well as other needle insertion procedures is the lancet point that was invented by Huber as far back as 1946 [173]. Needle insertion into soft tissues is a tissue cutting procedure which effectiveness and efficiency is dependent on the cutting-edge geometry of the needle tip [174]-[176]. Yancheng *et al.* [41] in their research on optimal needle design of the needle geometry to minimize the insertion force and bevel length (defined as the distance between the tip of the needle point to the lowest point of the bevel in the Z-direction [170]) based on mathematical models of cutting-edge inclination and rank angles. Based on the results of their research, an optimized needle will be modelled and used during the simulation procedure. The performance of a needle tip can be evaluated based on the bevel length and the insertion force. Research has it that the lower the insertion force, the lower the needle deflection and tissue deformation when performing the needle insertion process [177]. Also, it is less painful [178] and distressing for patients [179]-[181] as well as it being more precise in guiding the physician during the procedure thereby increasing the efficiency and safety. A shorter bevel length is preferred when assessing vessels. The shape of the lancet needle is usually determined by the following parameters: the bevel angle ( $\xi$ ), secondary bevel angle ( $\varphi$ ), the needle tube outer and inner radius as well as the angle of rotation ( $\beta$ ). In view of the above information and the results

obtained from their research, the chosen needle tip for this project had a bevel angle of  $12.4^\circ$ , an angle of rotation of  $15^\circ$ , a bevel length of 13.30 mm and a predicted insertion force of 0.94 Newtons as shown by needle B in figure 4.5 below. The needle has an outer and inner diameter of 3.048 mm and 2.388 mm respectively. Also, it has a wall thickness of 0.33 mm. The needle tip and needle developed for this project can be seen in figure 4.6 below.




	Needles	Angles	Bevel length (mm)	Model-predicted needle insertion force (N)*
Needle A		$\zeta = 12.0^\circ$ $\varphi = 18.0^\circ$ $\beta = 60.0^\circ$	13.30	1.06
Needle B		$\zeta = 12.4^\circ$ $\varphi = 12.4^\circ$ $\beta = 15.0^\circ$	13.30	0.94
Needle C		$\zeta = 23.0^\circ$ $\varphi = 23.0^\circ$ $\beta = 10.0^\circ$	7.17	1.06

Figure 4.5 - Optimized lancet needle geometry [41] (\* represents assuming  $\theta = 360^\circ$ )

In modelling this needle, the solidworks software was used by first and foremost specifying the inner and outer diameters and extruding them to obtain a cylindrical figure as shown in figure 5.3 (a). To obtain the specified needle tip, the following steps were employed: the needle tube was tilted at an angle of  $12.4^\circ$  to grind a bevel at the needle tube as shown in figure 5.3 (b). This was then followed by rotating the tube along the centerline axis at an angle of  $15^\circ$  and the grinding wheel was moved up by an offset distance from the datum plane to ensure that the first lancet was grinded as shown in figure 5.3 (c). Subsequently, the needle tube was rotated at an angle of  $30^\circ$  in the opposite direction as performed in the previous rotation to obtain the second lancet as shown in figure 4.6 (d) [41] to generate the needle displayed in figure 4.7 below.

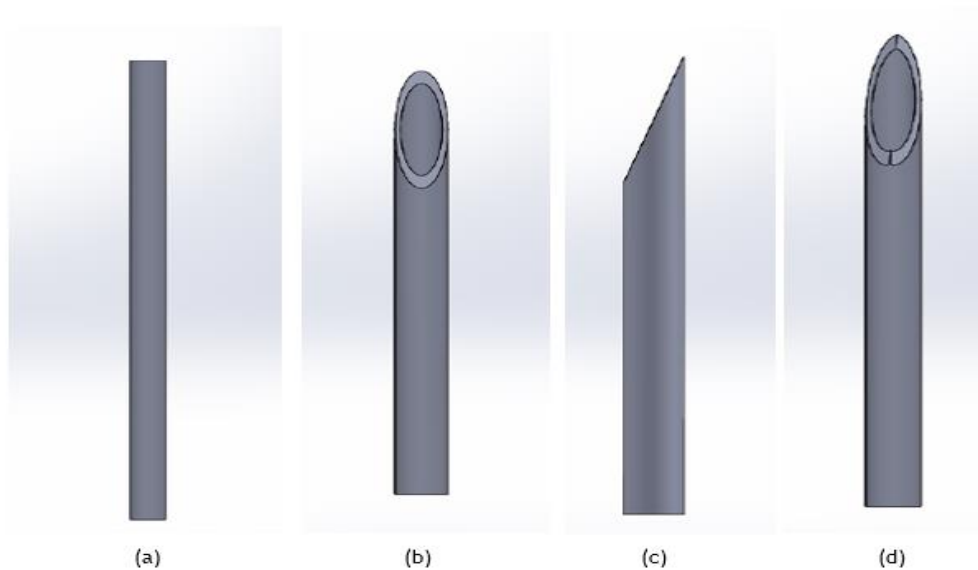


Figure 4.6 - (a) The cylindrical model of the needle. (b) The front view of the needle tube after grinding at an angle of  $12.4^\circ$ . (c) The side view of the needle tube after grinding at an angle of  $12.4^\circ$ . (d) Front view of the needle tube after the first and second lancet.





Figure 4.7 - Developed needle tip and needle for the needle simulation

### 4.3 - Tissue geometry and modelling

The human heart is composed of four (4) different layers namely the pericardium, epicardium, myocardium and the endocardium from the outer layer to the inner layer respectively. The diverse layers have distinct functions but collectively work together in the pumping of blood to all parts of the body by the heart [182]. The cardiac tissue consists of numerous interlocking cardiac muscle cells or fibres that gives the tissue its mechanical properties. It is vital to note that each individual cell is not mechanically strong enough but a collection of millions of them makes it possible for the heart to effectively discharge its duties [183].

To model the soft tissue and the cardiac muscle of the heart, two different slices or patches were considered and represented as an extruded cube using the Abaqus software. The cube had dimensions of 40 mm by 20 mm as shown in figure 4.8 below. A modified patch was also designed with dimensions of 40 mm by 40 mm to evaluate the effect of the difference in size on the simulation results. The patch was also considered to be an Eulerian component with two layers or materials comprising the tender tissue and the soft tissue for the needle insertion of the soft tissue and the tender tissue and cardiac muscle for the cardiac muscle needle insertion procedure. Both materials or layers had the same density which is equivalent to the density of water since the body is considered to be made up of about 70% of water. Also, both sections or materials had the same Poisson ratio of 0.475 as used in related works [184]. The tender tissue was designed to have Young's modulus similar to that of the human skin which is 0.129 MPa in accordance with research to improve the tenderness of the patch. The soft tissue however had a much lower Young's modulus of 0.007 MPa [184] while the cardiac muscle had a Young's Modulus of 0.1 MPa [185]. The tender tissue was designed to occupy the top-most region of the assembly with a depth of 5 mm. The soft tissue or cardiac muscle however occupied the rest of the Eulerian cube depending on the type of needle insertion simulation being performed. An initial part was also created to indicate the initial conditions of the simulation and as such it had no assigned material properties due to the fact that it does not take part in actual simulations.

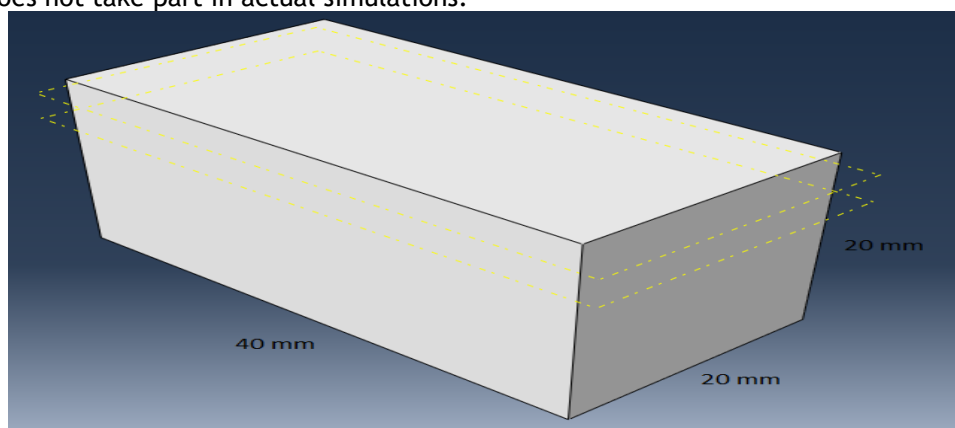


Figure 4.8 - An extruded cube representing the slice or layer of the soft tissue or cardiac muscle

## 4.4 - Simulation of needle insertion

After the various parts required to successfully simulate the needle insertion procedure were created using the required softwares, the Abaqus software was then used to assemble the various parts into the desired setup as shown in figure 4.9 to perform the needle insertion process. Two different sets of simulations were performed; a) needle insertion of the soft tissue and b) needle insertion of the cardiac muscles. The front, back, left and right views of the assembly are also displayed in figure 4.10 below. A dynamic explicit step of 2 seconds was created and the interval of the F-Output of the field output requests was set at 50.

The mesh of the assembly was generated by parts and not collectively as an assembly due to the complex geometry of the needle. The soft tissue and cardiac muscle mesh had a global size of 1 mm, a total number of 42336 nodes and 38637 total number of linear hexahedral elements of type EC3D8R. Figure 4.11 displays the generated mesh of the soft tissue or cardiac muscle. The generated mesh for the needle had 793 total number of nodes, 2281 total number of linear tetrahedral elements of type C3D4 and a global size of 1 mm. The generated mesh of the needle is shown in figure 4.12 while figure 4.13 denotes the generated mesh for the entire assembly.

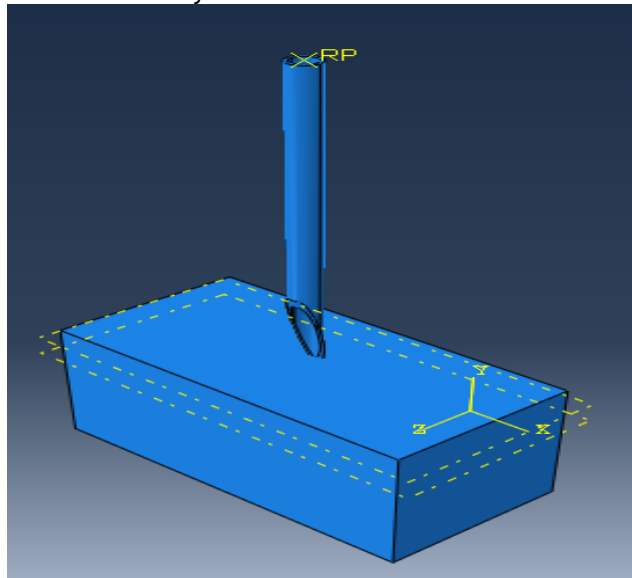


Figure 4.9 - Assembly of the soft tissue or cardiac muscle and the needle

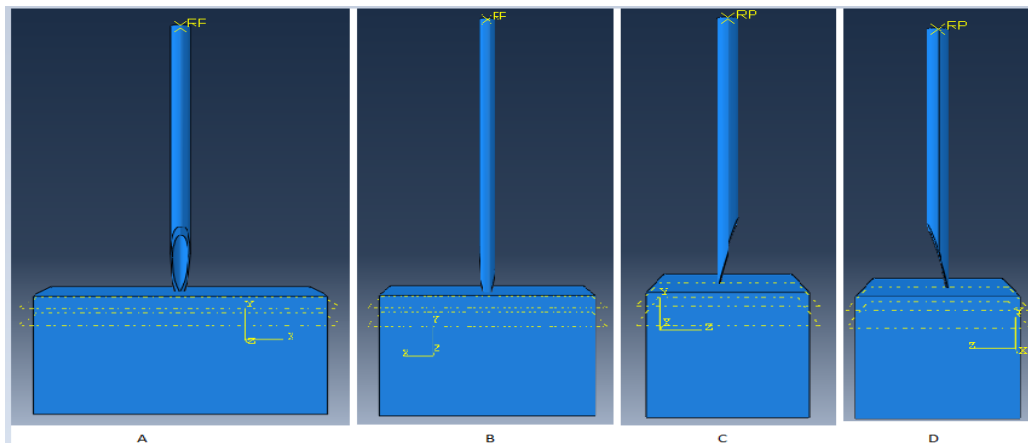


Figure 4.10 - The (A) Front, (B) Back, (C) Left and (D) Right views of the assembly

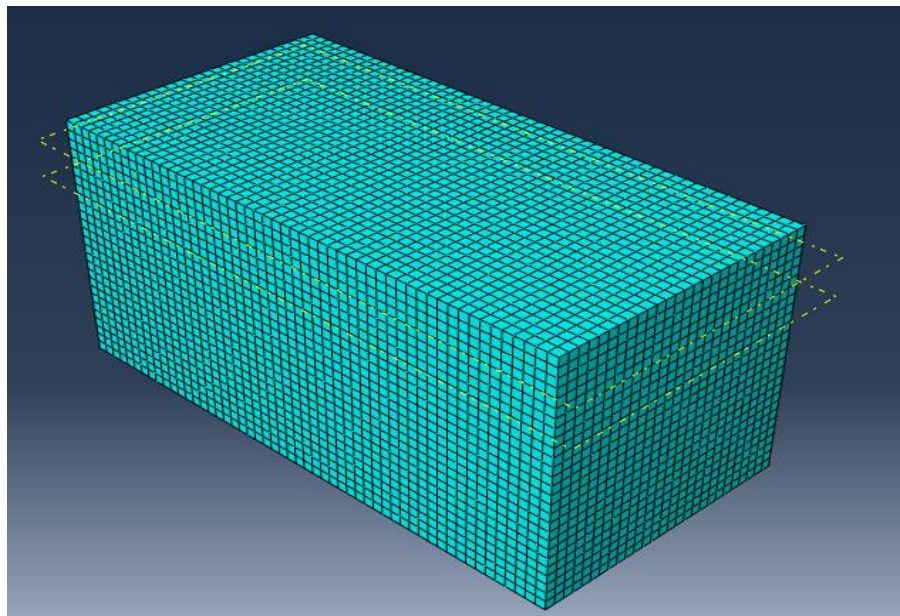


Figure 4.11 - The generated mesh of the soft tissue or cardiac muscle

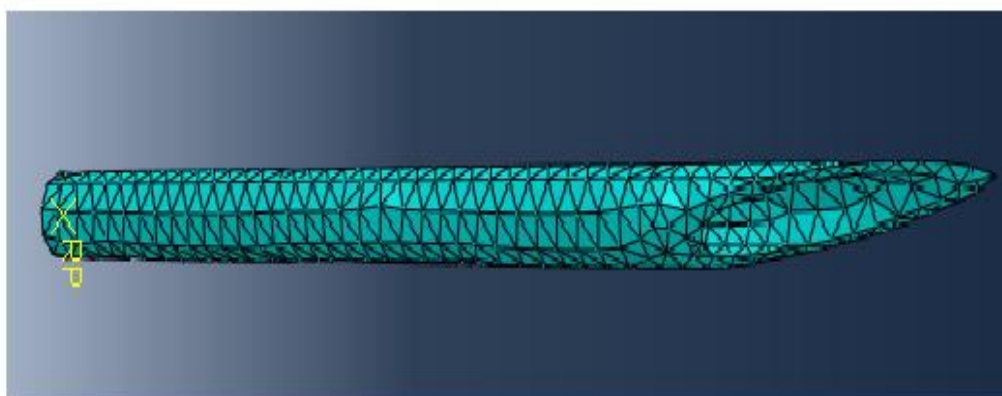


Figure 4.12 - The generated mesh of the needle

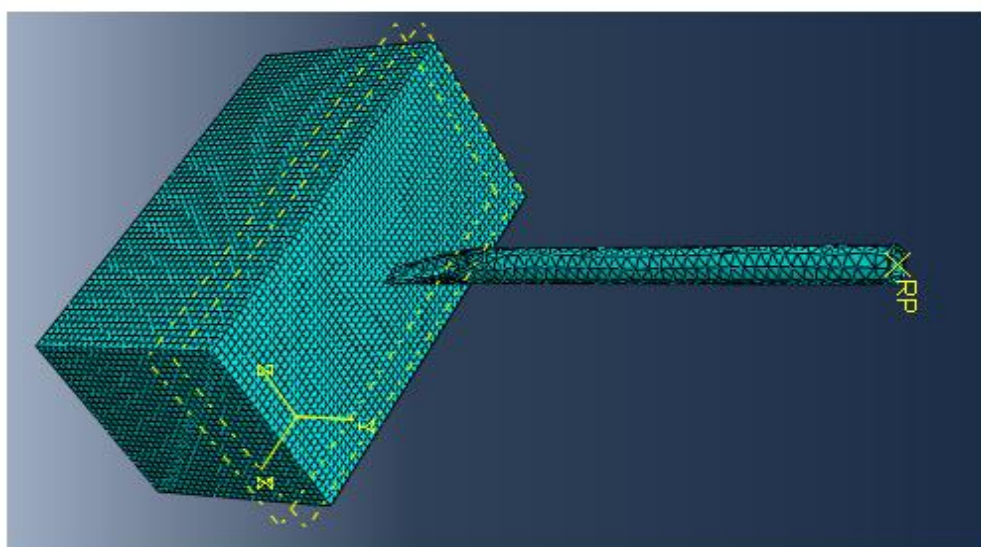


Figure 4.13 - The generated mesh of the entire assembly (Tissue and needle)

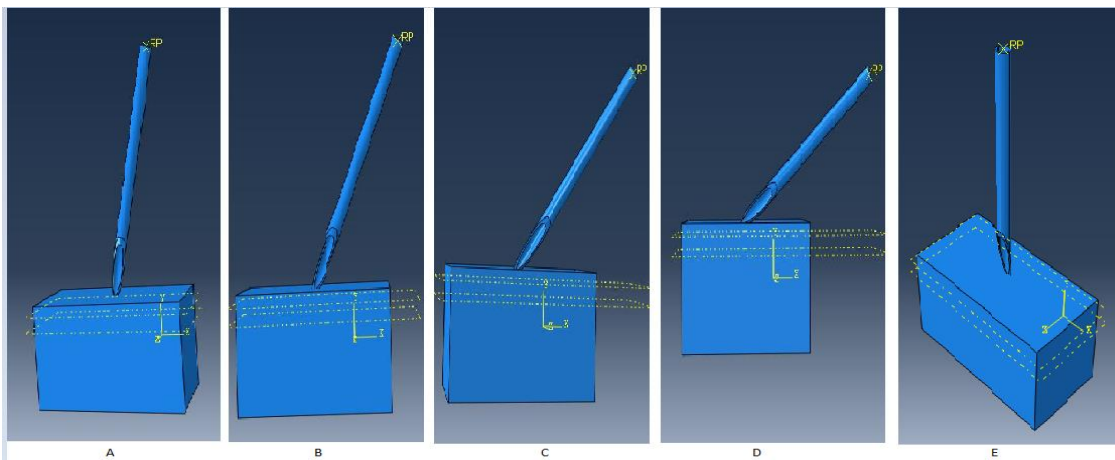
A general contact interaction was created with “All with self” as the contact domain, the contact property had a hard contact normal behaviour and a frictionless tangential behaviour. The reference point (RP) was selected at the top of the needle as shown in figure 4.13 above, the rigid body constraints of the setup were also defined. A discrete field associated to the Eulerian part with regards to the predefined field in the initial step was also created.

To load the setup, boundary conditions were created for the tissue by indicating the degree of freedom of the various faces of the soft tissue and the cardiac muscle before performing the simulation. The two faces of the soft tissue or cardiac muscle (Eulerian part) with the face normal to the Z-axis had V3 degree of freedom to fix the normal velocity of these faces, those (face of the soft tissue or cardiac muscle) with the face normal to the Y-axis had V2 degree of freedom to fix the normal velocity of the face and finally, those normal to the X-axis had V1 degree of freedom to fix the normal velocity of the face.

To create and run the job, the needle of the assembly was rotated at different angles with respect to X and Z axis and their respective displacement co-ordinates were calculated accordingly based on the angle of rotation. According to the calculations performed using the pythagorean theorem, the displacement co-ordinates of the X and Y axes were computed as shown below in table 4.2 with respect to the rotation about the Z-axis. The angles of rotation used in this simulation were  $0^\circ$ ,  $15^\circ$ ,  $30^\circ$ ,  $45^\circ$  and  $60^\circ$  which are shown in figure 4.14 below with respect to the Z-axis. Also, from the calculations obtained using the pythagorean theorem, the displacement co-ordinates of the Y and Z axes were tabulated as shown below in table 4.3 with respect to the rotation about the X-axis. The angles of rotation used in this simulation were also  $0^\circ$ ,  $15^\circ$ ,  $30^\circ$ ,  $45^\circ$  and  $60^\circ$  which are shown in figure 4.15 below with respect to rotation about the X-axis. It must be emphasized that this process was repeated since two sets of simulations were performed as stated earlier (simulation of needle insertion of the soft tissue and needle insertion of the cardiac muscle).

**Table 4.2** - Displacement co-ordinates for the X and Y axes for the rotation about the Z-axis

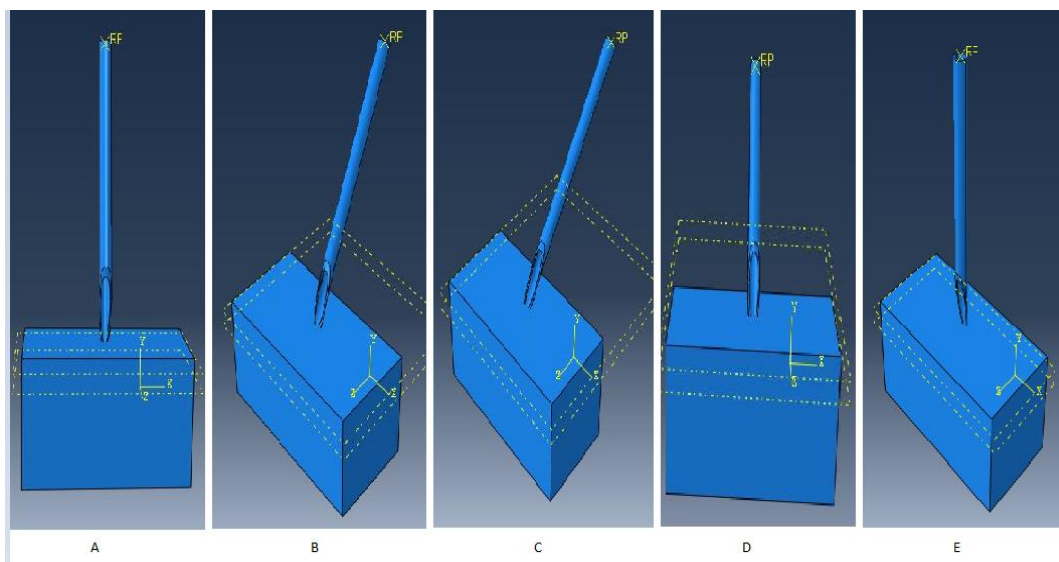
	$15^\circ$	$30^\circ$	$45^\circ$	$60^\circ$	$0^\circ$
X (mm)	-8.04	-14.43	-25	-26	0
Y (mm)	-30	-25	-25	-15	-25



**Figure 4.14** - (A)  $15^\circ$ , (B)  $30^\circ$ , (C)  $45^\circ$ , (D)  $60^\circ$  and (E)  $0^\circ$  angle of rotation of the needle about the Z-axis

**Table 4.3** - Displacement co-ordinates for the Y and Z axes for the rotation about the X-axis

	15°	30°	45°	60°	0°
Y (mm)	-30	-25	-25	-10	-25
Z (mm)	8.04	14.43	25	17.32	0

**Figure 4.15** - (A) 15°, (B) 30°, (C) 45°, (D) 60° and (E) 0° angle of rotation of the needle about the X-axis



## Chapter 5

# Simulation Results and Discussion

This chapter presents the results obtained from the simulation of the needle insertion of a slice or patch of the soft tissues as well as the cardiac muscles at different angulations of the needle as described in the previous chapter with regards to the X and Z axes. Subsequently, these results would be analyzed and discussed in this chapter.

The results would be presented in three main groups; the results of needle insertion forces, results of varying the size of the patch and finally, the results of the Mises force distribution during the simulations.

Furthermore, this chapter discusses the effects, implications and consequences of the results obtained from the simulations with respect to the applied forces and the correlation between the applied forces and the angle rotation, just to mention but a few.

### 5.1 - Results of needle insertion forces

During needle insertion, four main activities usually take place and they include: the initial puncture, insertion, relaxation and withdrawal but this research work or simulation focuses mainly on the initial puncture and the insertion. While the needle is progressively inserted into the tissue or cardiac muscle, the insertion force increases and decreases due to the series of small and big punctures within the tissue or cardiac muscle being simulated mostly resulting from appreciable changes in stiffness and/or an encounter of an obstacle. It can also be observed that the needle insertion force relatively increases linearly as a result of an increase in the frictional force due to the increase in surface area of the needle within the tissue or cardiac muscle during the needle insertion process [186].

The results represent two sets of simulations; the results of needle insertion force during the simulation of the soft tissue patch which is given in (a) and (b) are the results of the needle insertion force during the simulation of the cardiac muscle patch having the same dimensions as the soft tissue. To be able to have equal grounds for comparisons, the same degree of movements were specified for both simulations.

#### **a. Results of needle insertion force during the simulation of the soft tissue patch**

Five main simulations were done at different angles of the needle rotation along the Z-axis.

Figure 5.1 shown below gives a collective graphical representation of all the individual rotations of the needle insertion forces against time at angles  $15^\circ$ ,  $30^\circ$ ,  $45^\circ$ ,  $60^\circ$  and  $0^\circ$  (perpendicular) about the Z-axis.

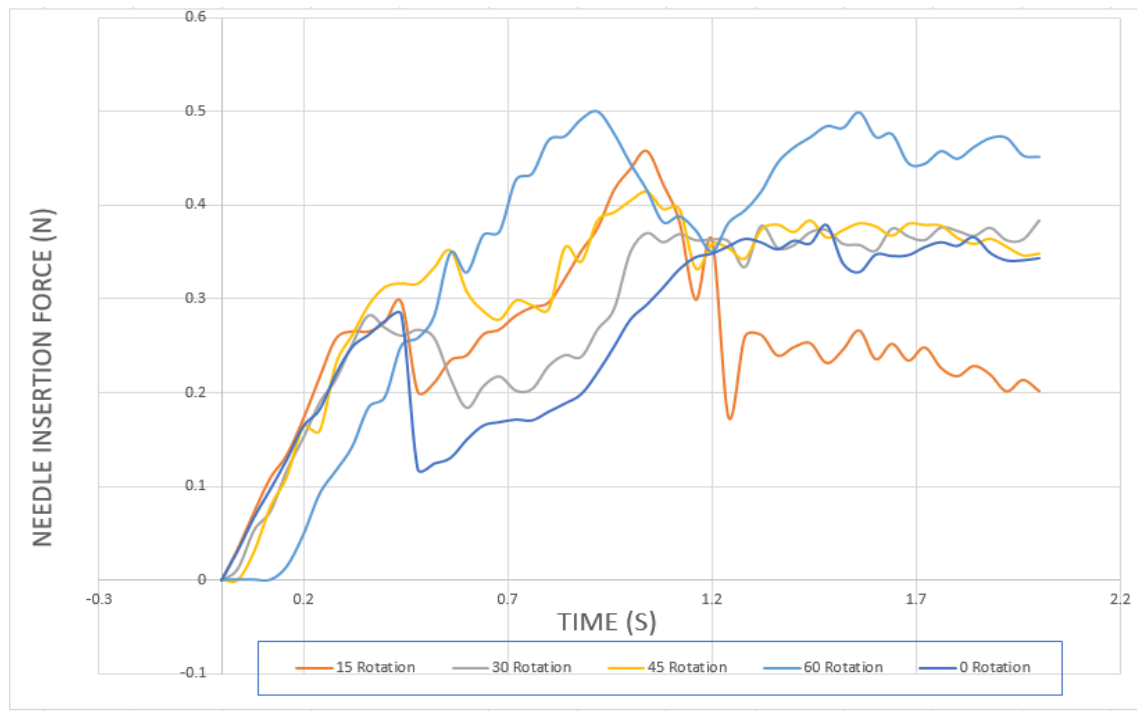


**Figure 5.1** - Graphical representation of all rotations of the needle about the Z-axis during the needle insertion into the soft tissue patch

From the graphical representation of the needle insertion forces against time in figure 5.1 above with regards to the initial dimensions of the patch of the soft tissue, the highest maximum generated needle insertion force was experienced at the  $60^\circ$  rotation about the Z-axis at a value approximately 0.5 N whereas the lowest generated maximum needle insertion force was experienced at the  $30^\circ$  rotation about the Z-axis at 0.377 N. Furthermore, it can be observed that all the graphical representations of figure 5.1 had two main peaks or spikes due to the fact that two different materials of different Young's modulus were used to depict the tender tissue and the soft tissue making up the patch for the simulation. In view of this, they both require different maximum insertion forces resulting in the difference in the spikes. The first spike represents the maximum needle insertion force of the tender tissue and the second spike is the maximum insertion force of the soft tissue.

Also, it can be observed that the insertion force drops getting to the end of the simulation for all the simulations of the rotation about the Z-axis using the initial dimension of the soft tissue because the simulation was done in a way to ensure that the needle perforates the soft tissue to denote the perforation of the atria. As a result of this perforation of the soft tissue, the needle insertion force drops gradually as observed in figure 5.1.

Similar to the rotation about the Z-axis, five simulations were also performed at different angles of the needle rotation about the X-axis. Figure 5.2 shown below denotes the collective graphical representation of all the individual rotations of the needle insertion forces against time at angles  $15^\circ$ ,  $30^\circ$ ,  $45^\circ$ ,  $60^\circ$  and  $0^\circ$  (perpendicular) about the X-axis.



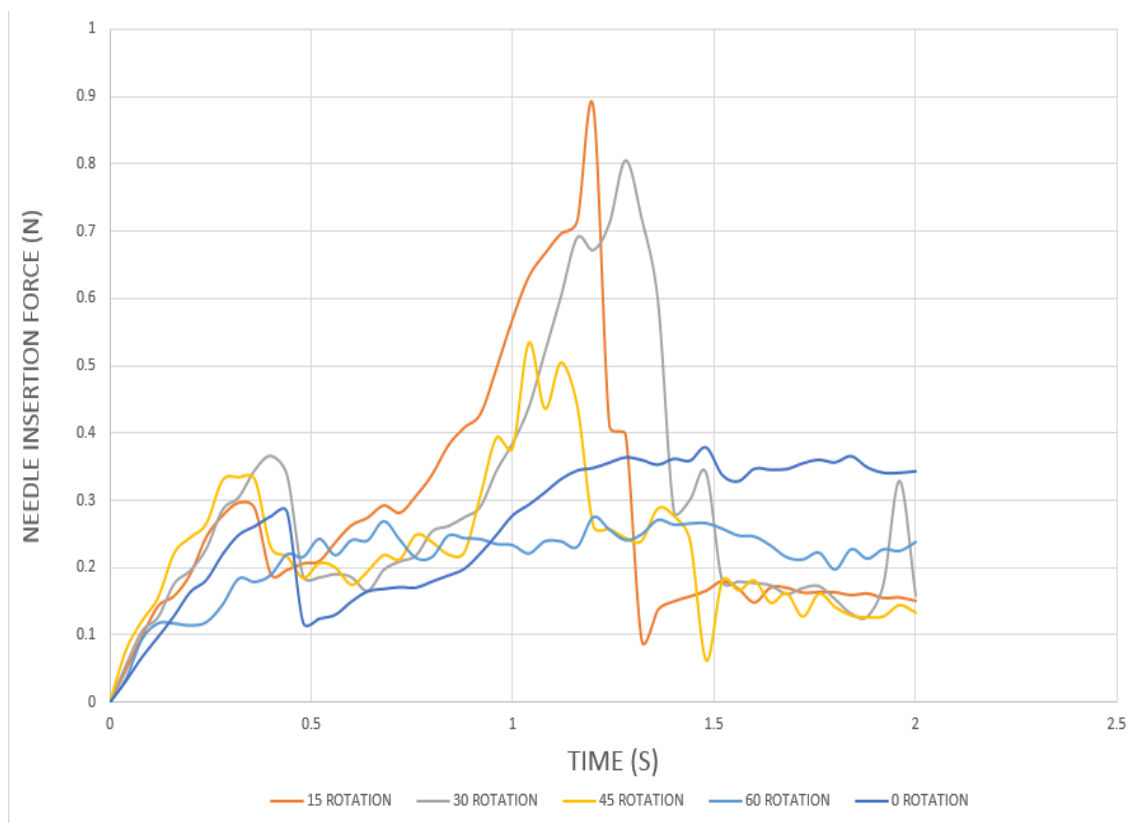


**Figure 5.2** - Graphical representation of all rotations of the needle about the X-axis during the needle insertion into the soft tissue patch

From figure 5.2 above, with regards to the simulation using the initial dimensions of the patch of the soft tissue, the highest generated needle insertion force was experienced at the 15° rotation about the X-axis at a value approximately 0.88 N whereas the lowest generated maximum needle insertion force was experienced at the 60° rotation about the X-axis at 0.272 N. Also, it can be observed that all the graphical representations in figure 5.2 have at least two main spikes due to the fact that two different materials of different Young's modulus were used to depict the tender tissue and the soft tissue.

Ideally, since the assembly (tender tissue and soft tissue) was considered to be homogenous, then the axis of rotation of the needle should have no influence on the obtained results but the opposite was observed in this simulation largely due to the orientation of the bevel of the needle after the rotation of the needle about the axis before the simulation was performed. From the analyze of the simulations performed, it was observed that the orientation of the bevel was different for the same degree of rotation about the two axes hence affecting the needle insertion forces for a given angel of rotation and as such affecting the generated graphical representation of the needle insertion force against time.

#### **b. Results of needle insertion force during simulation of the cardiac muscle patch**

Similar to the soft tissue simulations, five simulations were conducted at different angles of the needle rotation about the Z-axis.

Figure 5.3 represents the collective representation of all the individual rotations (15°, 30°, 45°, 60° and 0° (perpendicular)) about the Z-axis of the needle insertion forces against time as shown below during the needle insertion procedure into the cardiac muscle patch.

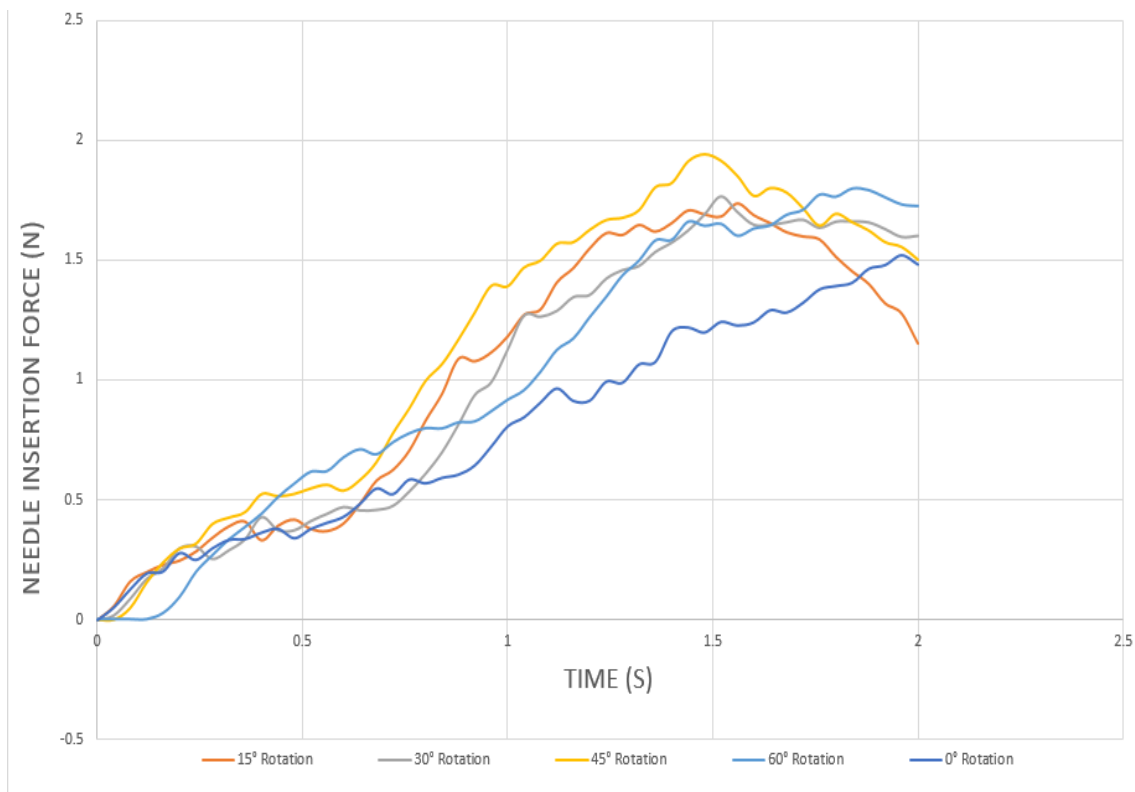


**Figure 5.3** - Graphical representation of all rotations of the needle about the Z-axis during the needle insertion into the cardiac muscle patch

To have a better understanding of the simulations, the mechanical properties of the soft tissue patch were modified to conform to that of the cardiac muscle and the same simulations performed for the soft tissue patch were repeated. From the graphical representation of the needle insertion forces against time in figure 5.3 above in relation to the initial dimensions of the cardiac muscle patch, the highest generated needle insertion force was experienced at the 45° rotation about the Z-axis at a value approximately 1.94 N whereas the lowest generated maximum needle insertion force was experienced at the 0° rotation about the Z-axis at 1.52 N. It can also be observed that this simulation has higher insertion forces compared to the simulations performed on the soft tissue patch as expected due to the high mechanical properties of the cardiac muscles compared to the soft tissues.

As described above, five main simulations were performed at different angles of the needle rotation about the X-axis.

Figure 5.4 shown below denotes the collective graphical representation of all the individual rotations of the needle insertion forces against time at angles 15°, 30°, 45°, 60° and 0° (perpendicular) about the X-axis.

With regards to figure 5.4 below, the highest generated needle insertion force was experienced at the 15° rotation about the X-axis at a value approximately 2.45 N whereas the lowest generated maximum needle insertion force was experienced at the 60° rotation about the X-axis at 0.59 N. Both simulations of the soft tissue and cardiac muscle about the X-axis showed that the 60° rotation provided the lowest amount of insertion forces during the simulations.

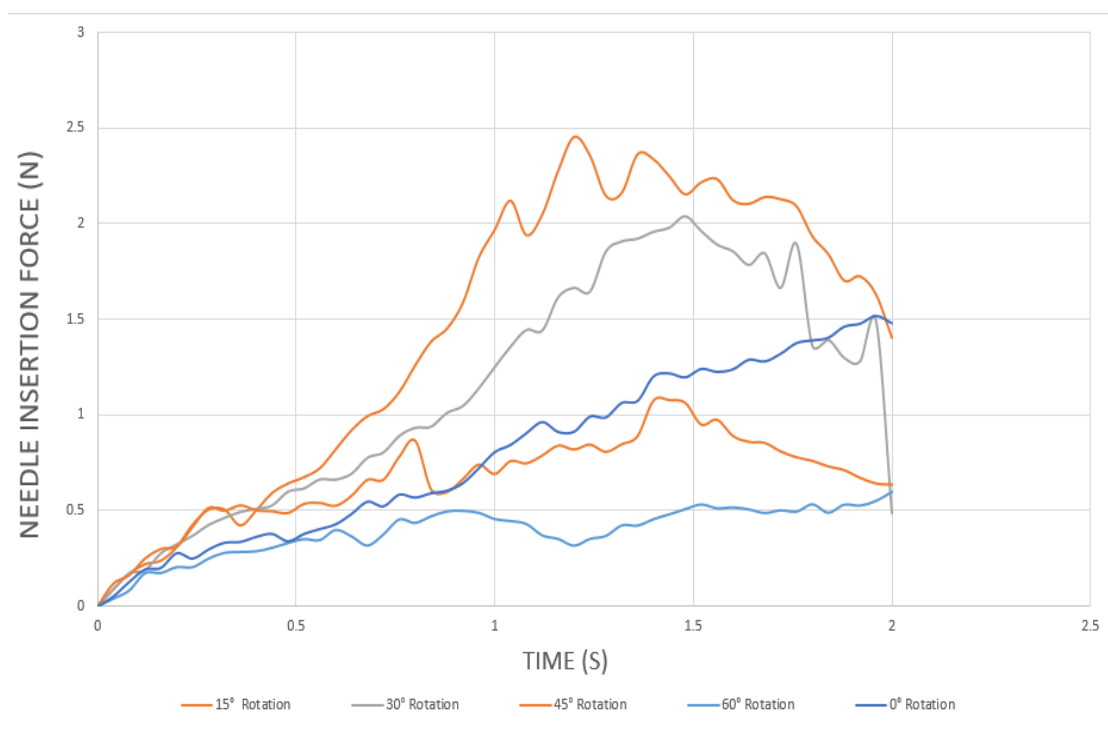


**Figure 5.4** - Graphical representation of all rotations of the needle about the X-axis during the needle insertion into the cardiac muscle patch

## 5.2 - Results of varying the size of the patch

In the bid to acquire an in-depth knowledge and understanding of the effect of the size of the patch of the tissue or cardiac muscle being simulated on the results, I varied the dimensions of the patch for the simulations from 40 mm by 20 mm to 40 mm by 40 mm while keeping their respective mechanical properties exactly the same. The simulations were done for selective angles of rotations ( $30^\circ$ ,  $45^\circ$  and  $0^\circ$ ) about the X and Z-axes and their respective graphical representations have been displayed in figures 5.5 to 5.14 below.

To evaluate the effect of varying the size of the patch of the soft tissue being simulated on the obtained results, from figures 5.5 and 5.6 below, it was observed that the graphical representations of the simulation of the new dimensions of the soft tissue patch (denoted as bigger dimension of tissue in the figure) about the  $30^\circ$  rotation about the X and Z-axes had very similar graphical distributions of the needle insertion forces or simply had a similar graph as that of the initial patch dimensions (denoted as initial dimension of tissue). The distinct difference however is that the bigger soft tissue patch had a relatively lower maximum needle insertion force compared to that obtained from the initial size simulation above for the same angle of rotation.

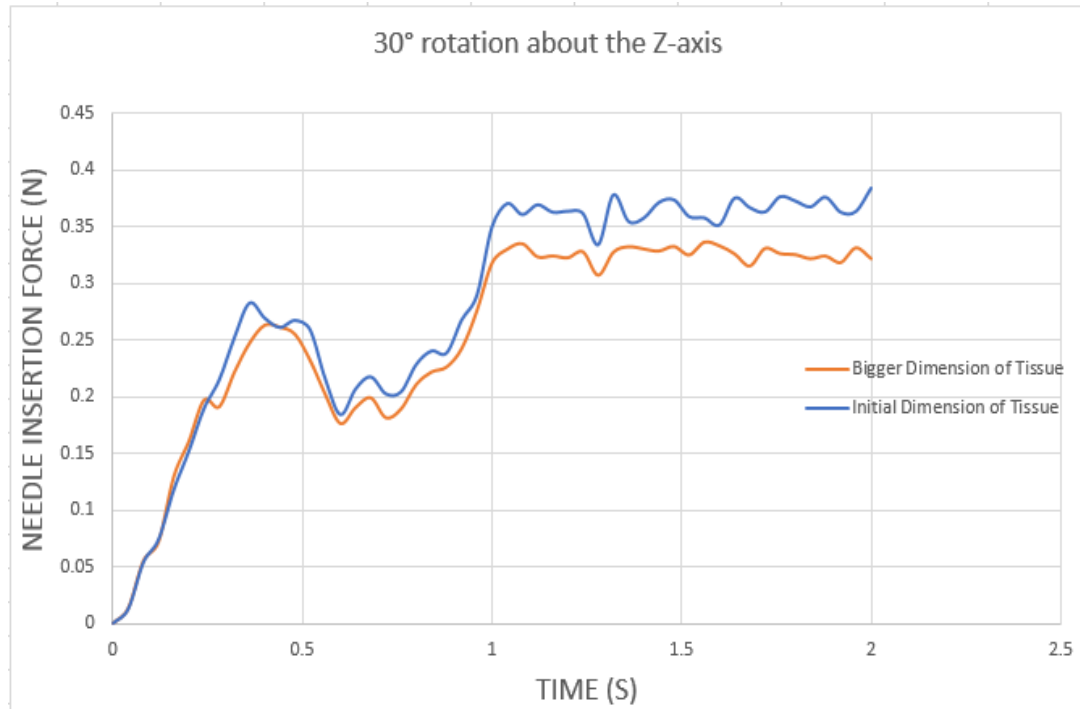


**Figure 5.5** - Graphical representation of a 30° rotation of the needle about the Z-axis during the needle insertion into the soft tissue patch for both the initial and modified dimensions of the soft tissue patch

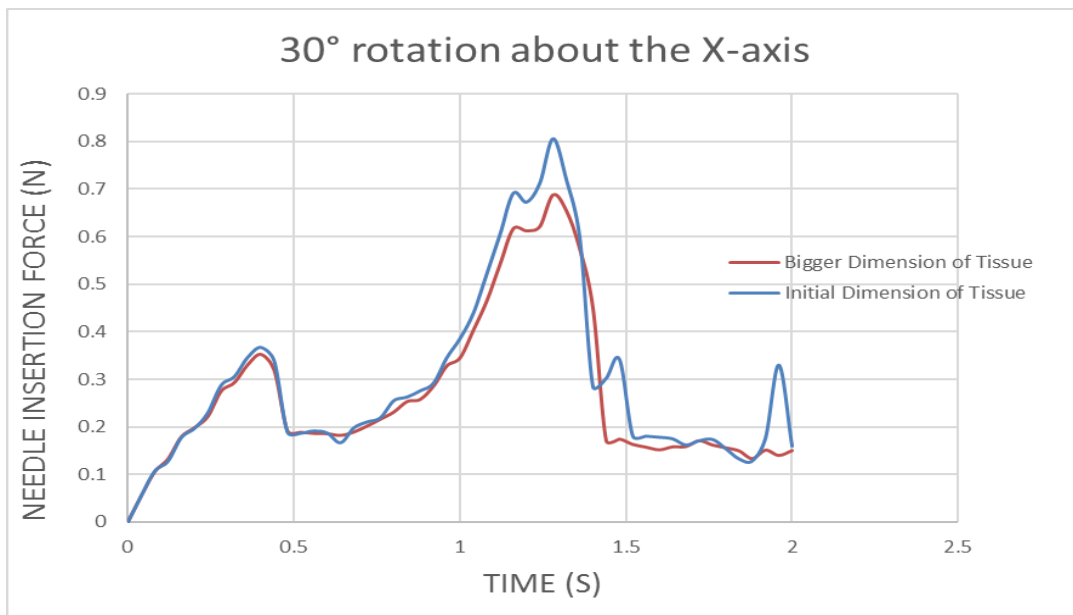


**Figure 5.6** - Graphical representation of a 30° rotation of the needle about the X-axis during the needle insertion into the soft tissue patch for both the initial and modified dimensions of the soft tissue patch

As the angle of rotation about the Z-axis was increased to 45°, it was noticed that the graphical representation differed slightly from that obtained originally from the simulation of the initial size of the soft tissue patch as shown in figure 5.7 below. It also had a higher needle insertion force of 0.5 N compared to that of the initial size which was 0.41 N. Again, there was a relatively sharp fall in the needle insertion force after the perforation for the bigger dimension of the soft tissue patch compared to the initial smaller size of the patch.

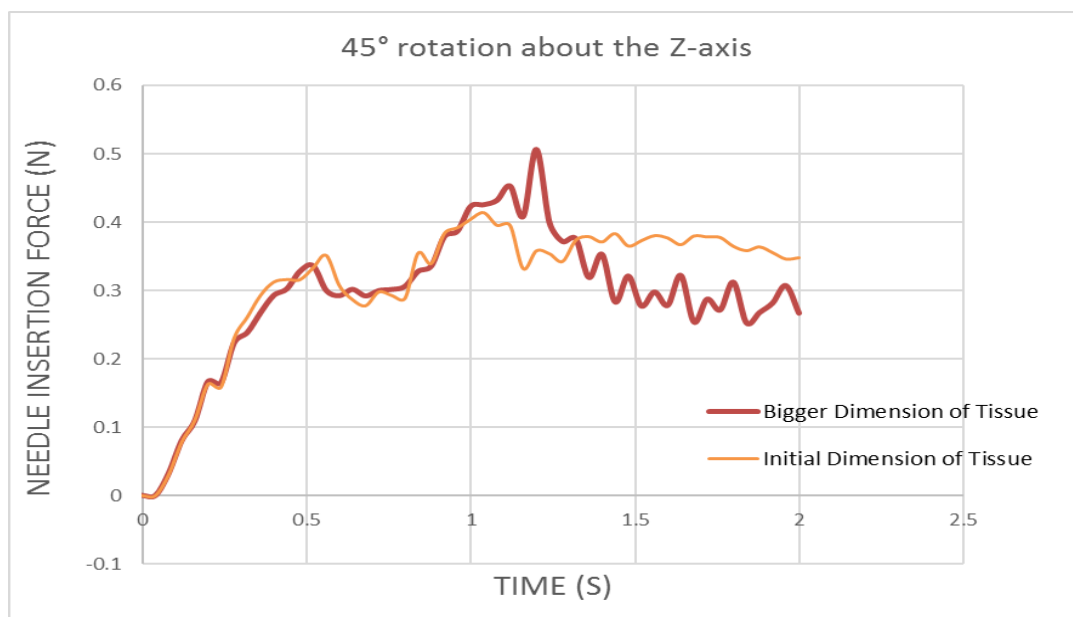


**Figure 5.7** - Graphical representation of a 45° rotation of the needle about the Z-axis during the needle insertion into the soft tissue patch for both the initial and modified dimensions of the soft tissue patch

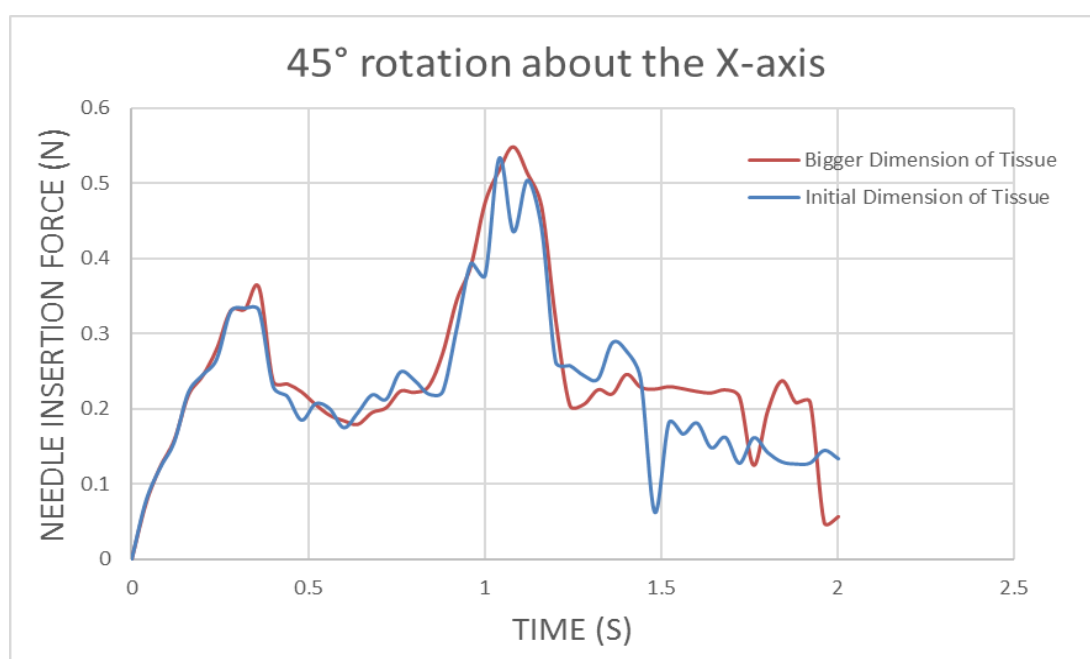


**Figure 5.8** - Graphical representation of a 45° rotation of the needle about the X-axis during the needle insertion into the soft tissue patch for both the initial and modified dimensions of the soft tissue patch

Furthermore, during the perpendicular (0°) insertion of the needle as shown in figure 5.9 below, a similar graphical representation of the needle insertion force against time was observed between the initial and modified dimensions of the soft tissue patch. Also, both the initial and new dimensions of the soft tissue patch had relatively the same maximum needle insertion force due to the fact that the needle traversed the soft tissue patch perpendicularly and during this procedure, they both had the same surface area of penetration hence the similarity in the needle insertion forces.

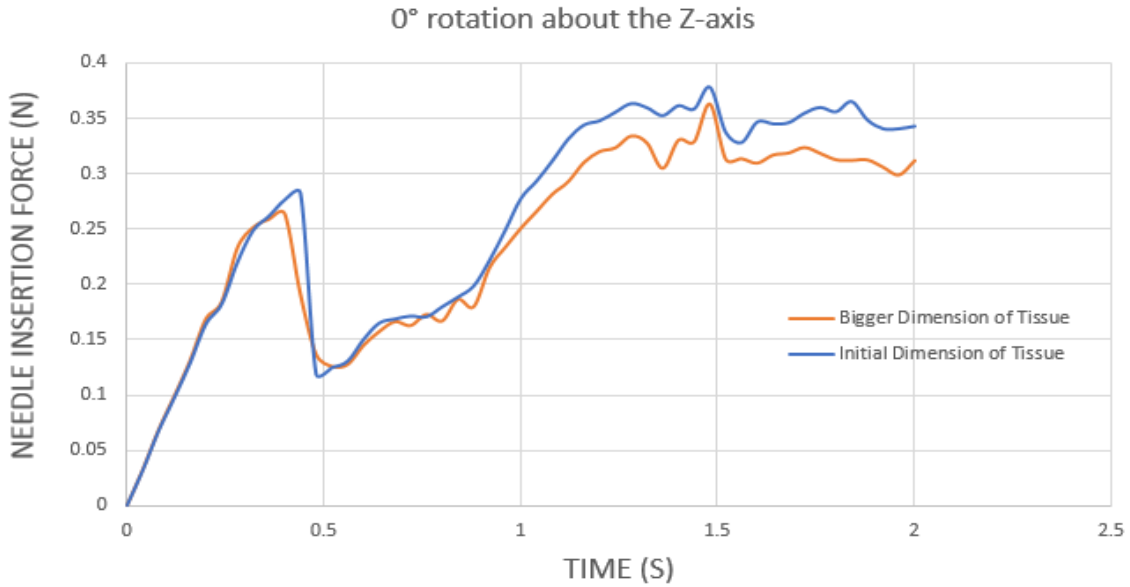


**Figure 5.9** - Graphical representation of a 0° rotation of the needle during the needle insertion into the soft tissue patch for both the initial and modified dimensions of the soft tissue patch

Evaluating the effect of varying the size of the cardiac muscle patch being simulated on the results obtained, figures 5.10 and 5.11 denoting the graphical representations of the simulation of the new dimension of the cardiac muscle about the 30° rotation about the Z and X-axes respectively had very similar graphical distributions of the needle insertion forces against time compared to the initial dimension of the patch. The obvious difference however was that the bigger dimension of the cardiac muscle patch had a relatively lower maximum needle insertion force compared to that from the initial patch dimension and it was very prominent in the rotation about the X-axis.

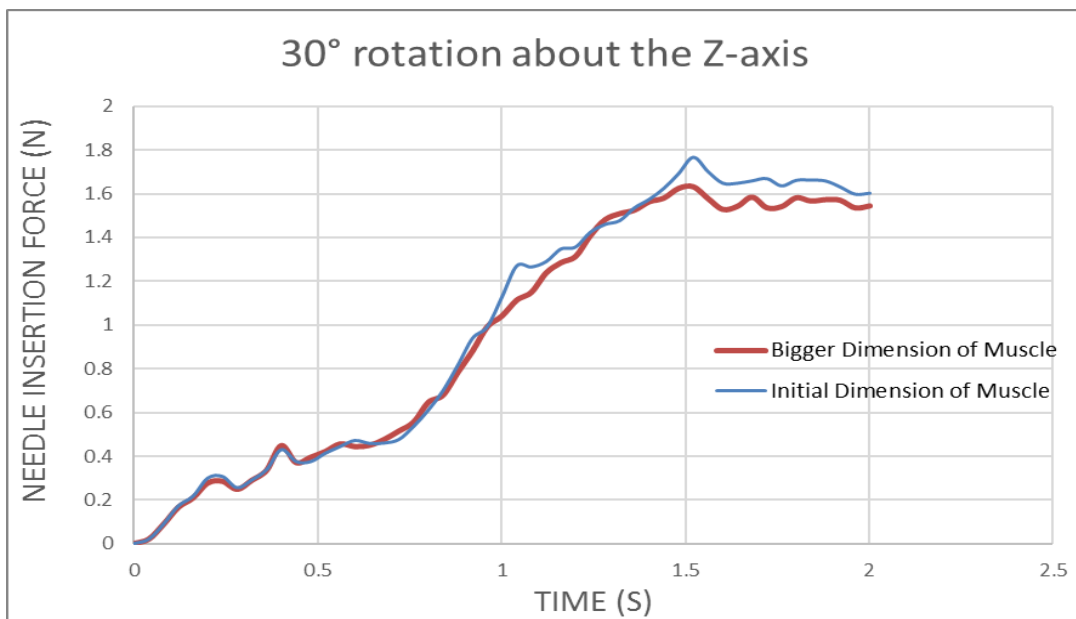


**Figure 5.10** - Graphical representation of a 30° rotation of the needle about the Z-axis during the needle insertion into the cardiac muscle for both the initial and new dimensions of the cardiac muscle patch

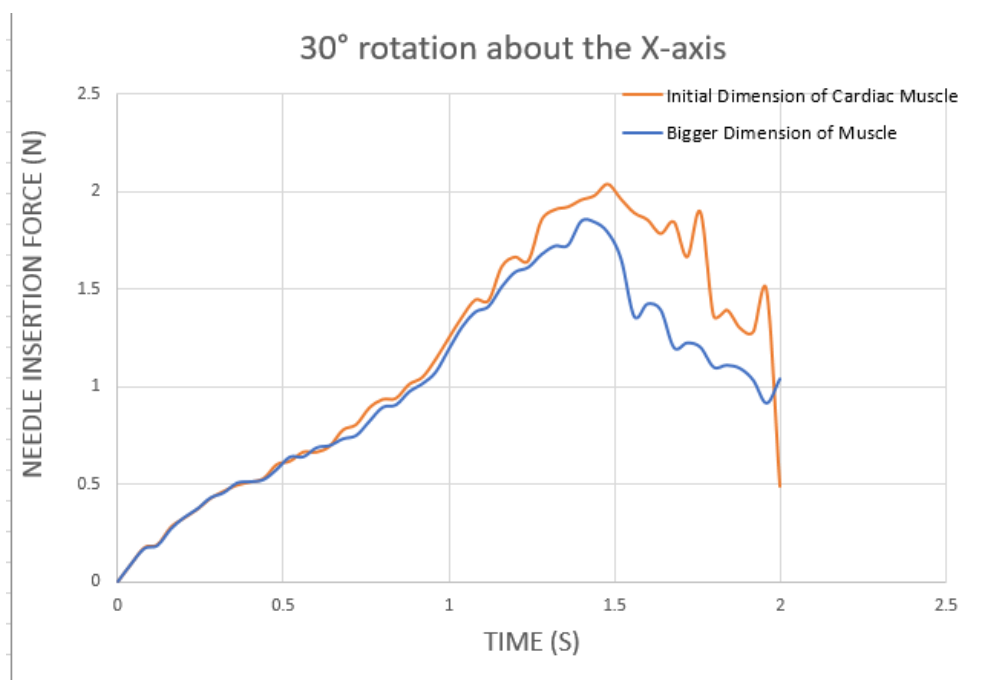


**Figure 5.11** - Graphical representation of a 30° rotation of the needle about the X-axis during the needle insertion into the cardiac muscle for both the initial and new dimensions of the cardiac muscle patch

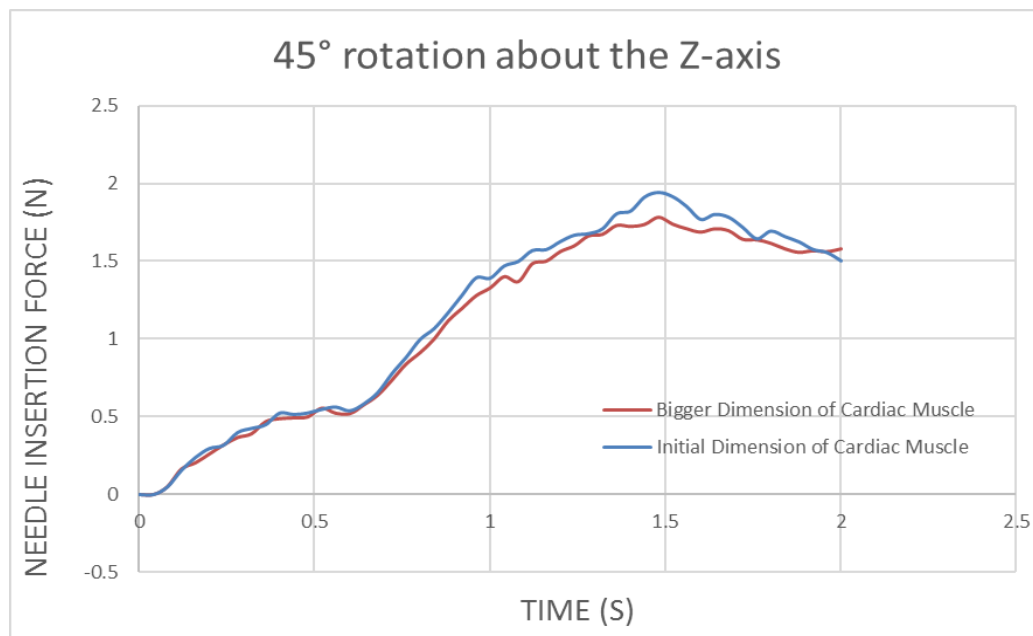


**Figure 5.12** - Graphical representation of a 45° rotation of the needle about the Z-axis during the needle insertion into the cardiac muscle for both the initial and modified dimension of the cardiac muscle patch

In relation to the 45° rotation about the Z-axis, the graphical representation was relatively similar and the maximum needle insertion forces were approximately the same indicating that the size of the cardiac muscle patch being simulated had little or no effect on the needle insertion forces and the graph for a 45° rotation about the Z-axis as shown in

figure 5.12 above. Also, by increasing the angle of rotation about the X-axis to  $45^\circ$ , it was observed that the graphical representation differed largely from the graph obtained during the simulation of the initial dimension of the cardiac muscle patch as displayed in figure 5.13 below and this could be attributed to the difference in width of the patch. The new dimension also had a higher needle insertion force of 1.49 N compared to that of the initial dimension which was 1.06 N due to an increase in surface area as the needle traverses the cardiac muscle patch resulting in an increase in frictional force leading to an increase in the needle insertion force. In addition, the graph (figure 5.13) had a relatively sharp drop in the needle insertion force after the perforation for the bigger dimension of the patch compared to the initial (smaller) dimension of the cardiac muscle patch which had a steady drop in needle insertion force.

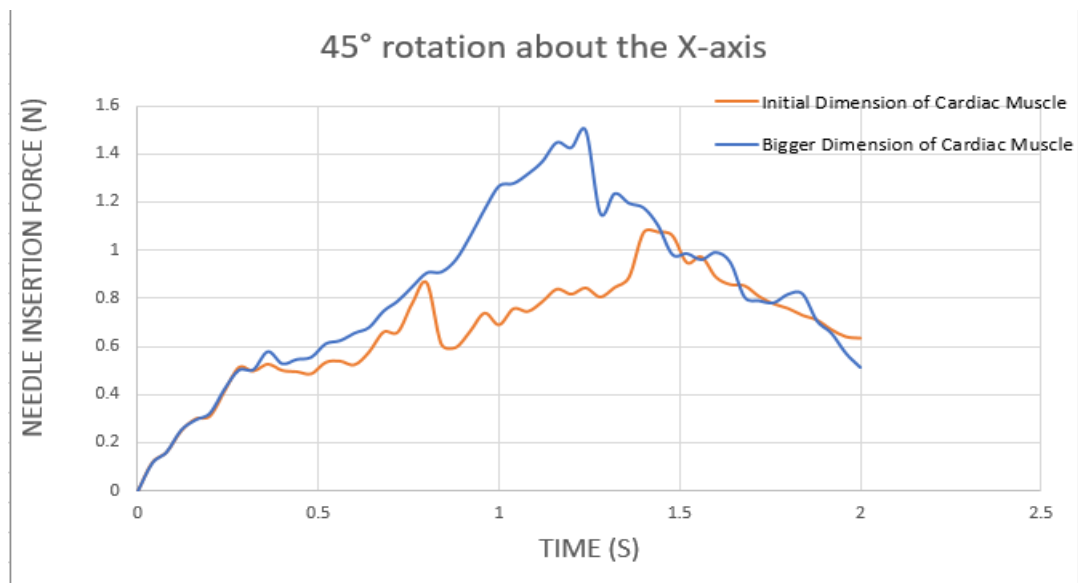


**Figure 5.13** - Graphical representation of a  $45^\circ$  rotation of the needle about the X-axis during the needle insertion into the cardiac muscle for both the initial and new dimension of the cardiac muscle patch

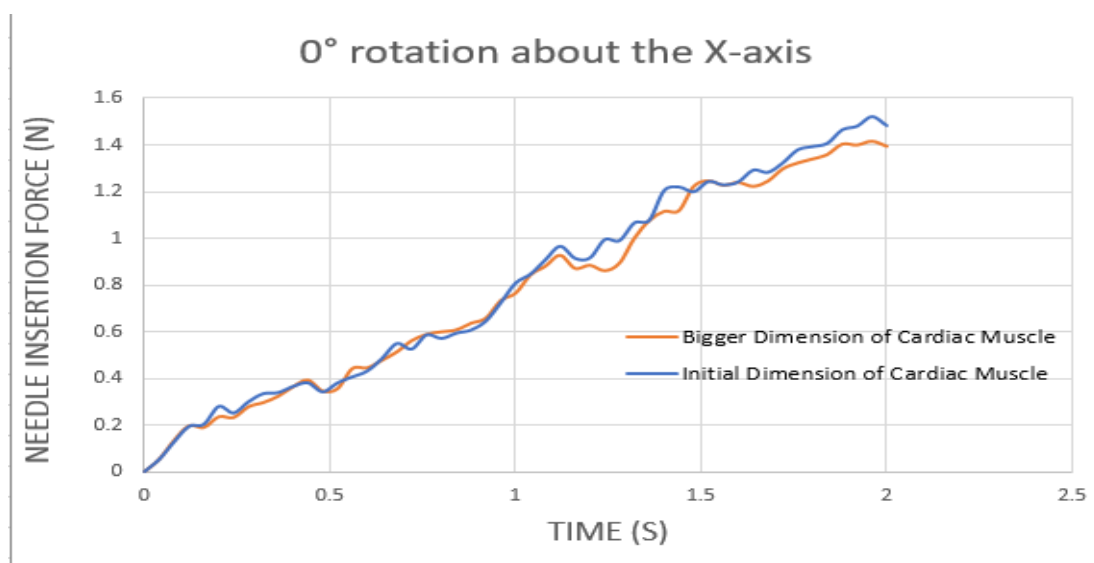


**Figure 5.14** - Graphical representation of a  $0^\circ$  rotation of the needle about the X-axis during the needle insertion into the cardiac muscle for both the initial and new dimension of the cardiac muscle patch



Furthermore, during the perpendicular insertion of the needle as shown in figure 5.14, a similar graphical representation of the needle insertion force against time was observed between the initial dimension and the modified dimension of the cardiac muscle patch but the initial cardiac muscle patch had a slightly higher maximum needle insertion force (1.48 N) compared to the modified dimension of the soft tissue (1.41 N).

### 5.3 - Results of the von Mises stress distribution

Furthermore, to get a thorough visualization of the needle insertion force distribution during the needle insertion simulation, a visual display of the stress distribution experienced by the tender tissue, soft tissue and the cardiac muscle have been provided below from figure 5.15 to figure 5.34.

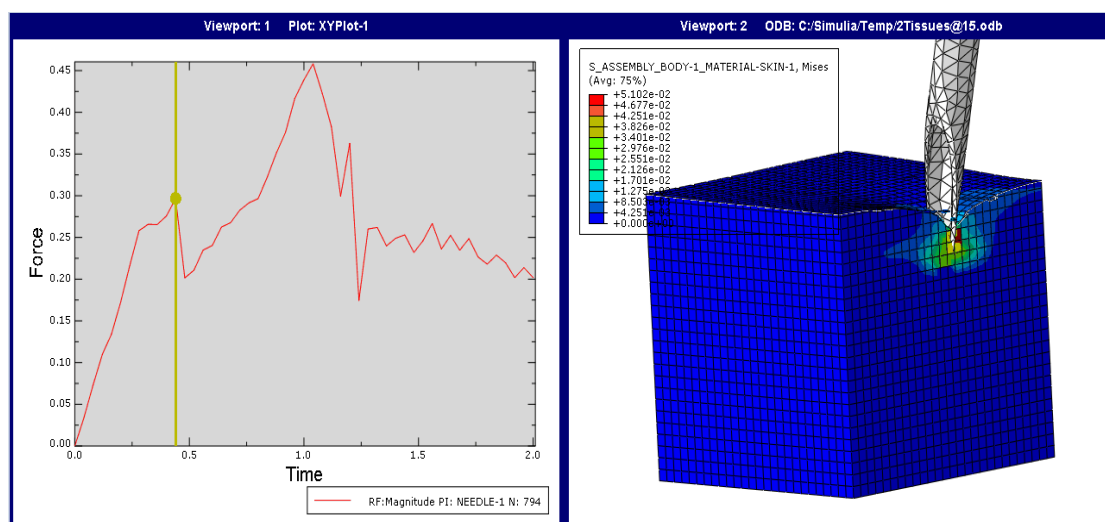


Figure 5.15 - Mises stress distribution of the tender tissue at a 15° rotation of the needle about the Z-axis during the needle insertion into the soft tissue patch

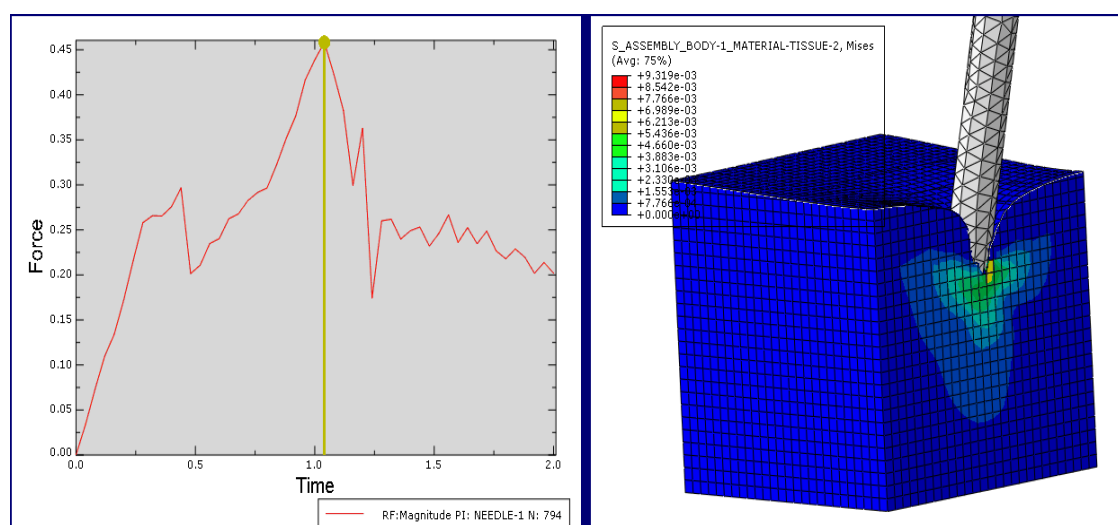
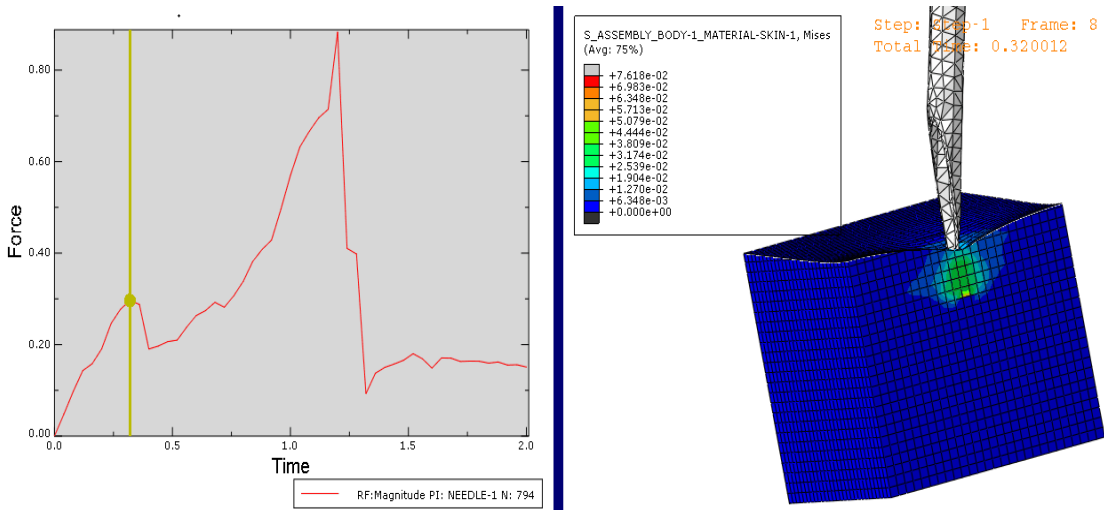
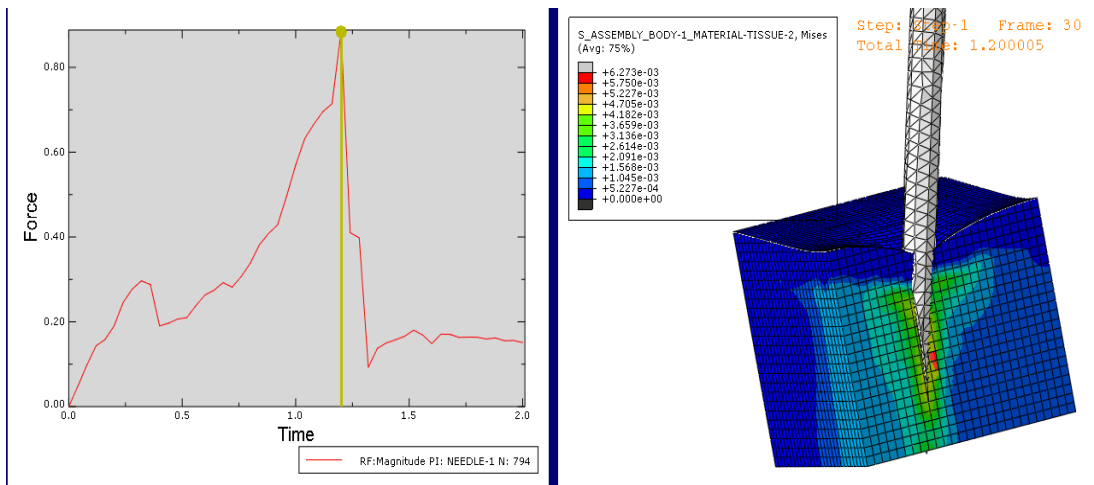


Figure 5.16 - Mises stress distribution of the soft tissue at a 15° rotation of the needle about the Z-axis during the needle insertion into the soft tissue patch



**Figure 5.17** - Mises stress distribution of the tender tissue at a 15° rotation of the needle about the X-axis during the needle insertion into the soft tissue patch



**Figure 5.18** - Mises stress distribution of the soft tissue at a 15° rotation of the needle about the X-axis during the needle insertion into the soft tissue patch

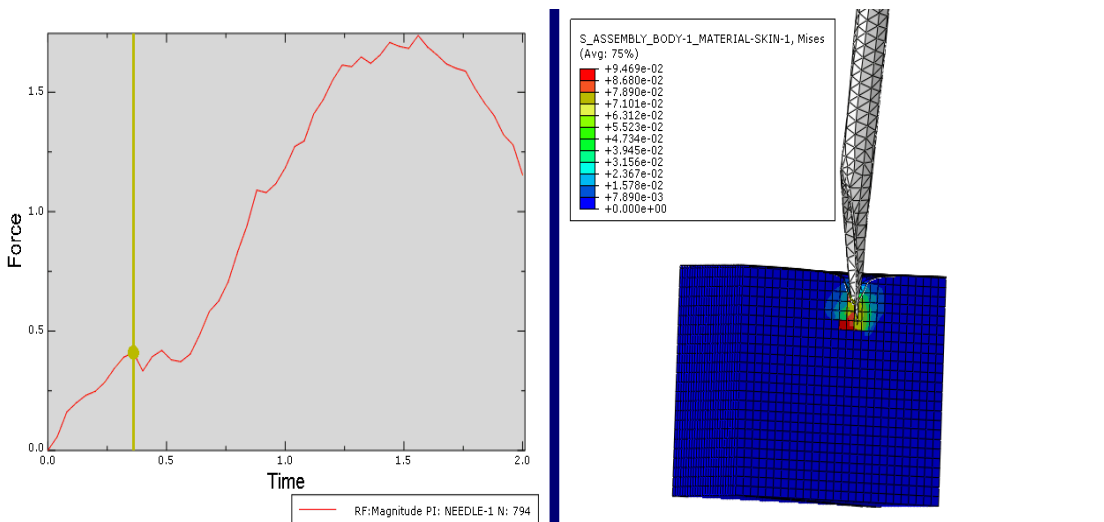


**Figure 5.19** - Mises stress distribution of the tender tissue at a 15° rotation of the needle about the Z-axis during the needle insertion into the cardiac muscle patch

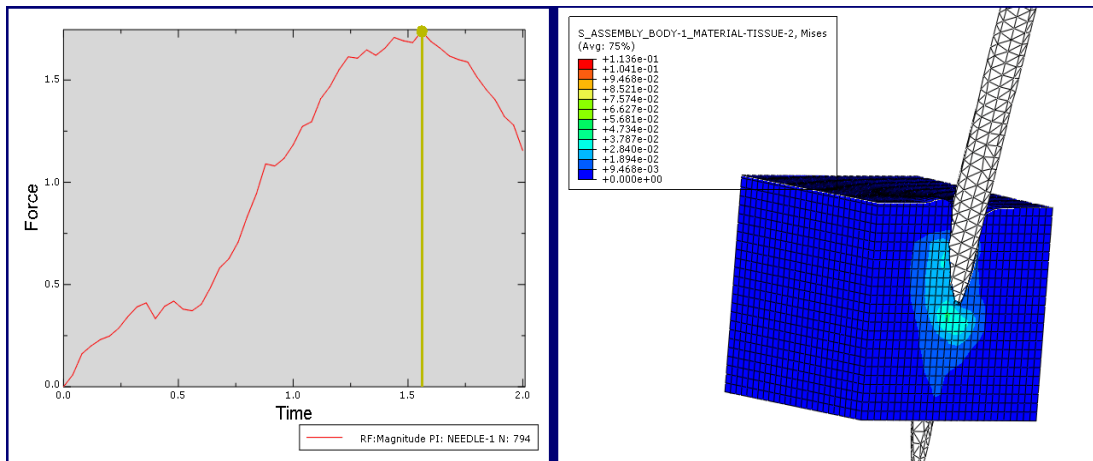


**Figure 5.20** - Mises stress distribution of the cardiac muscle at a 15° rotation of the needle about the Z-axis during the needle insertion into the cardiac muscle patch

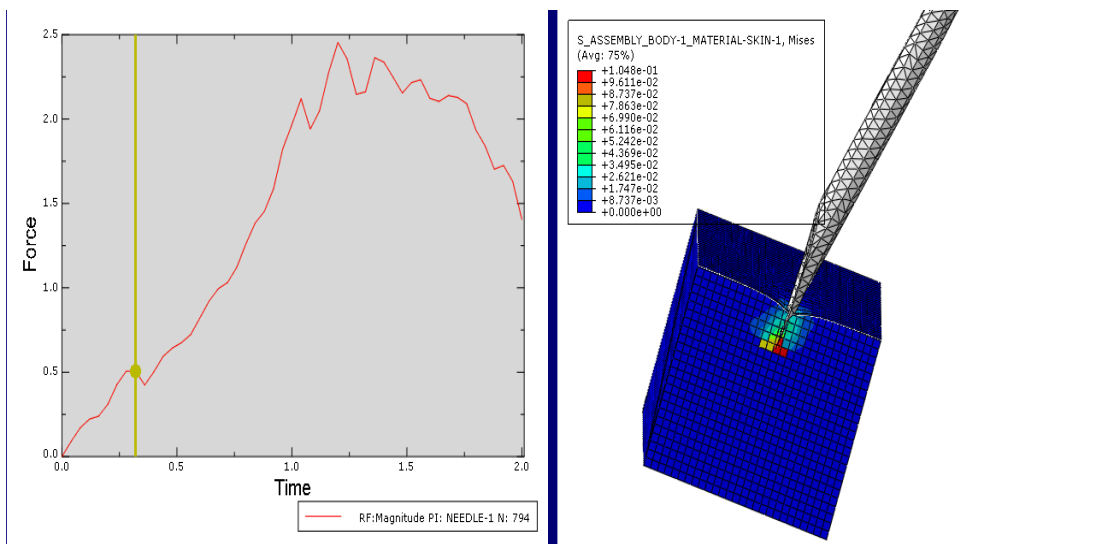


**Figure 5.21** - Mises stress distribution of the tender tissue at a 15° rotation of the needle about the X-axis during the needle insertion into the cardiac muscle patch

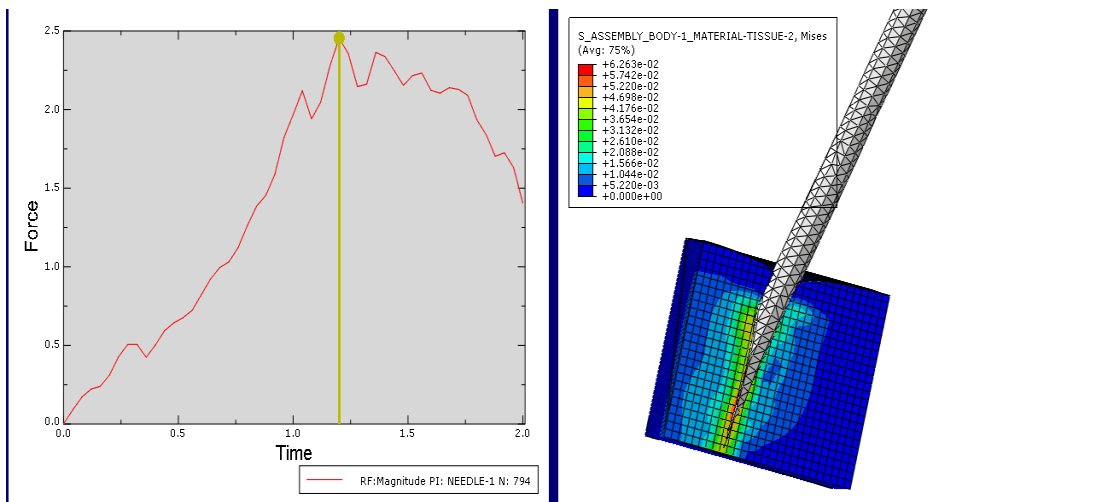


**Figure 5.22** - Mises stress distribution of the cardiac muscle at a 15° rotation of the needle about the X-axis during the needle insertion into the cardiac muscle patch

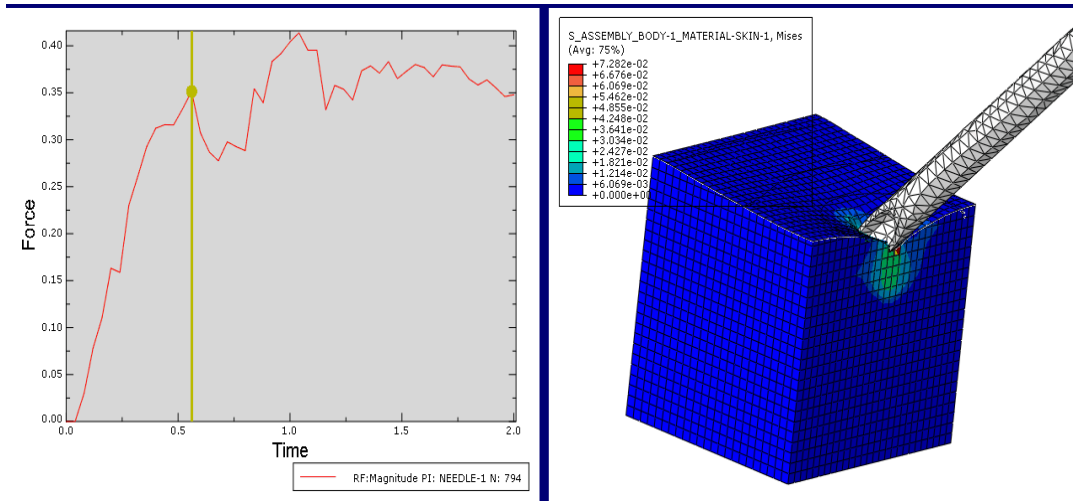


**Figure 5.23** - Mises stress distribution of the tender tissue at a 45° rotation of the needle about the Z-axis during the needle insertion into the soft tissue patch

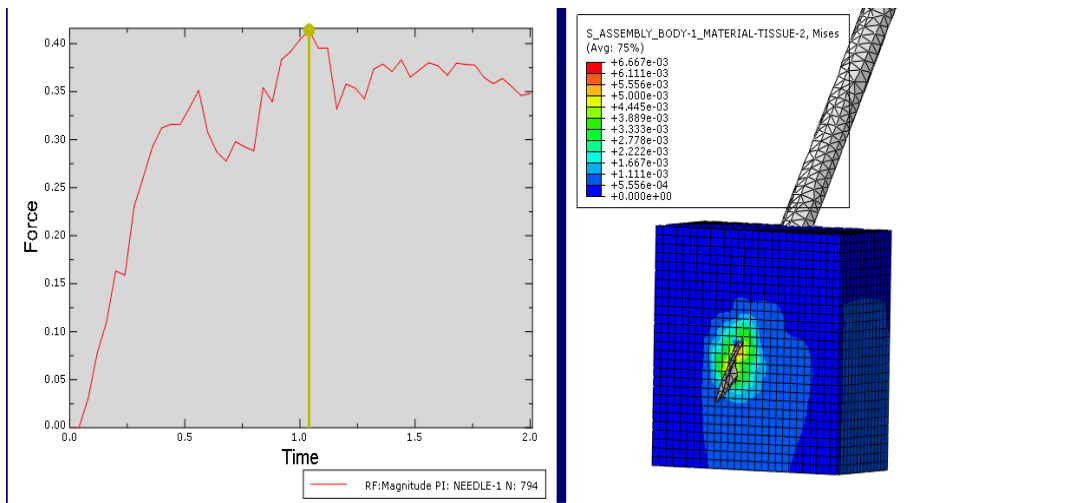


**Figure 5.24** - Mises stress distribution of the soft tissue at a 45° rotation of the needle about the Z-axis during the needle insertion into the soft tissue patch

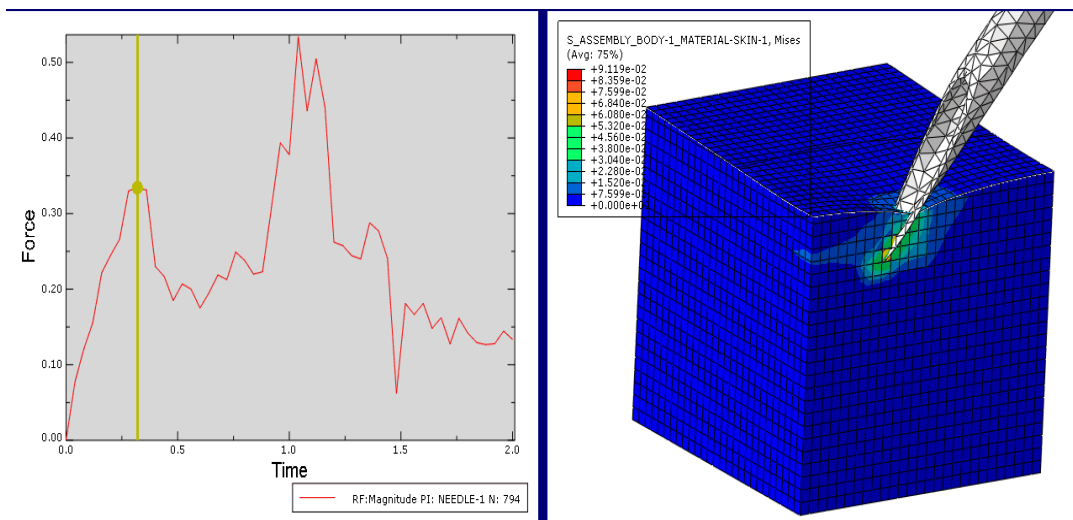


**Figure 5.25** - Mises stress distribution of the tender tissue at a 45° rotation of the needle about the X-axis during the needle insertion into the soft tissue patch

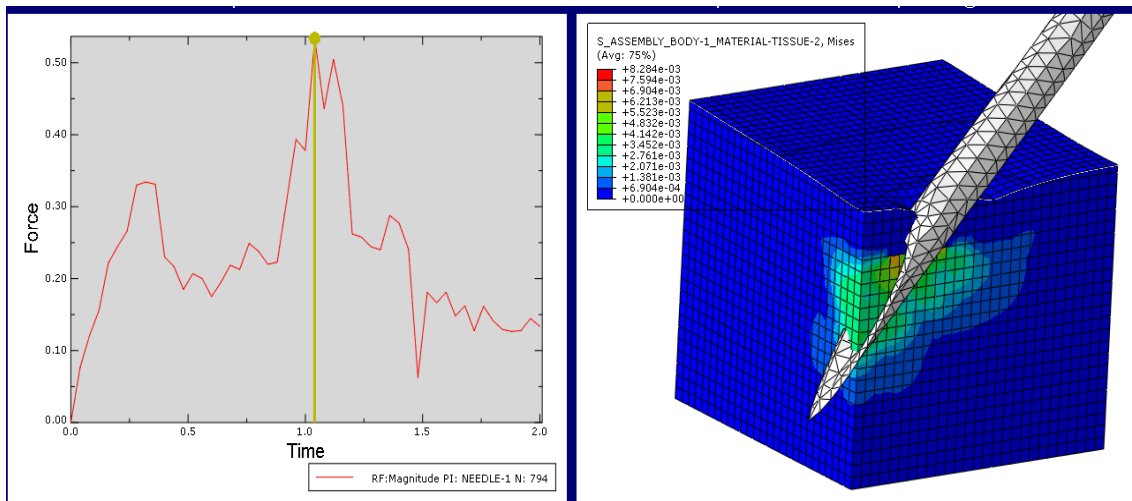


Figure 5.26 - Mises stress distribution of the soft tissue at a 45° rotation of the needle about the X-axis during the needle insertion into the soft tissue patch

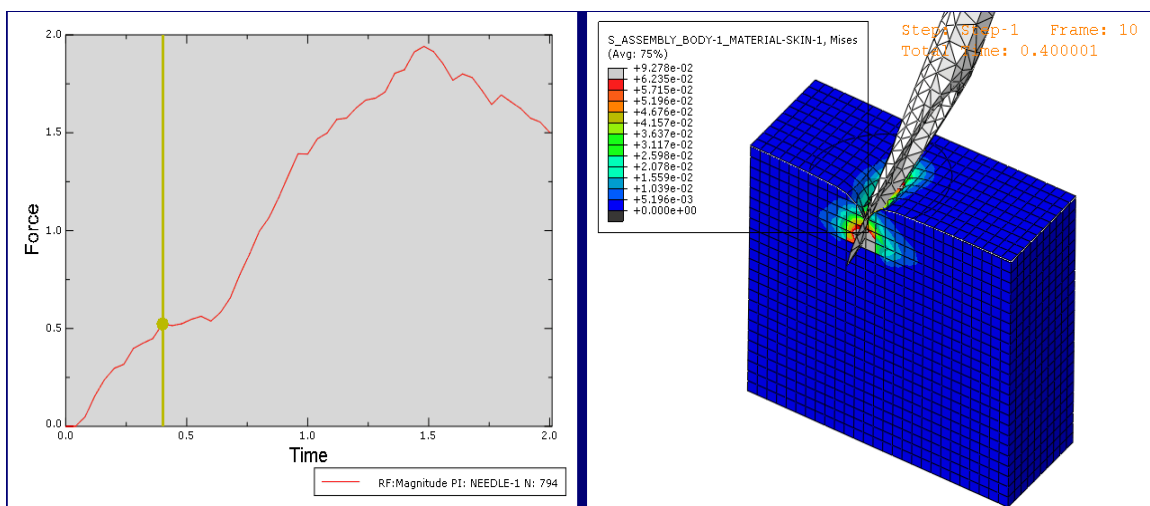


Figure 5.27 - Mises stress distribution of the tender tissue at a 45° rotation of the needle about the Z-axis during the needle insertion into the cardiac muscle patch

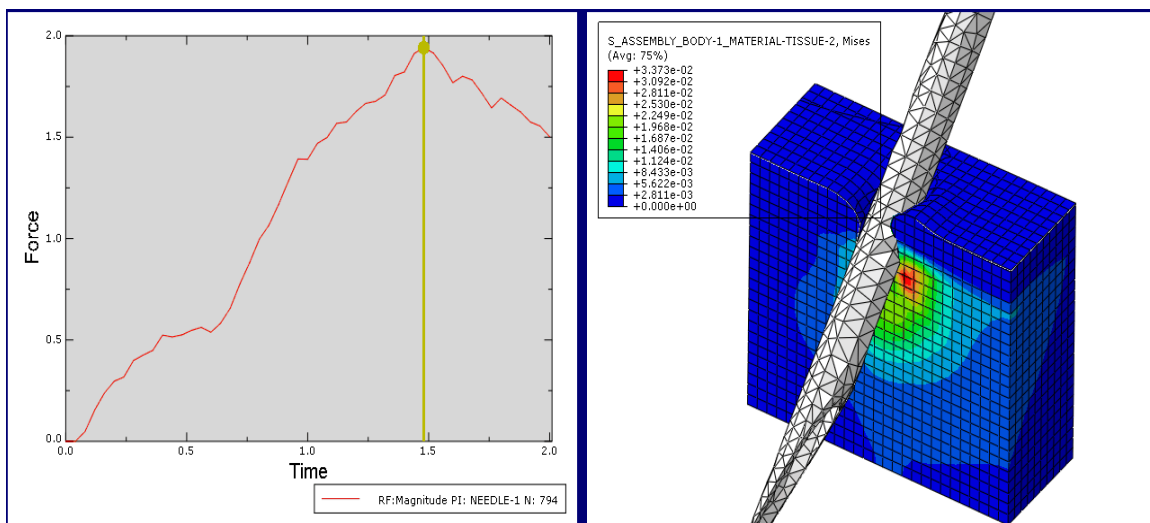


Figure 5.28 - Mises stress distribution of the cardiac muscle at a 45° rotation of the needle about the Z-axis during the needle insertion into the cardiac muscle patch

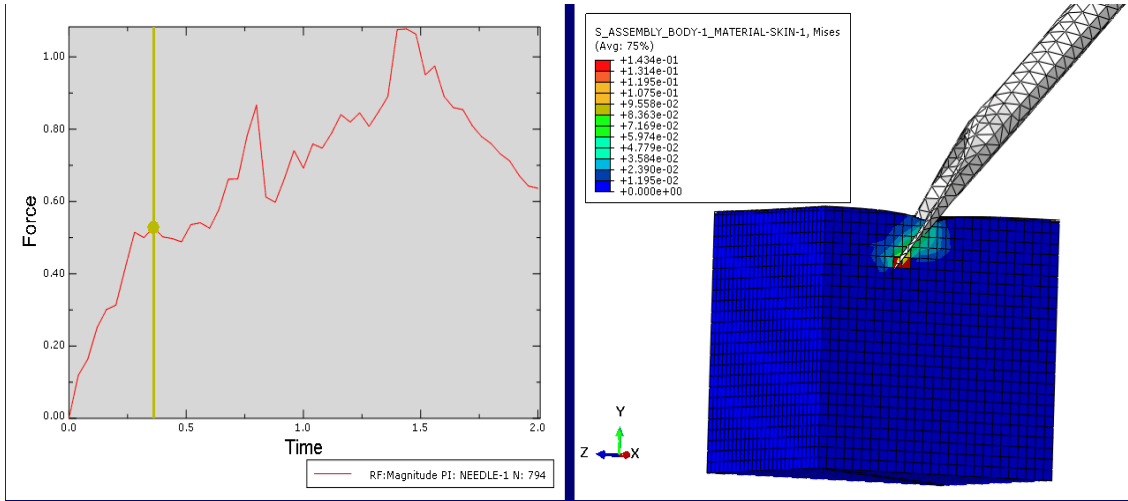


Figure 5.29 - Mises stress distribution of the tender tissue at a 45° rotation of the needle about the X-axis during the needle insertion into the cardiac muscle patch

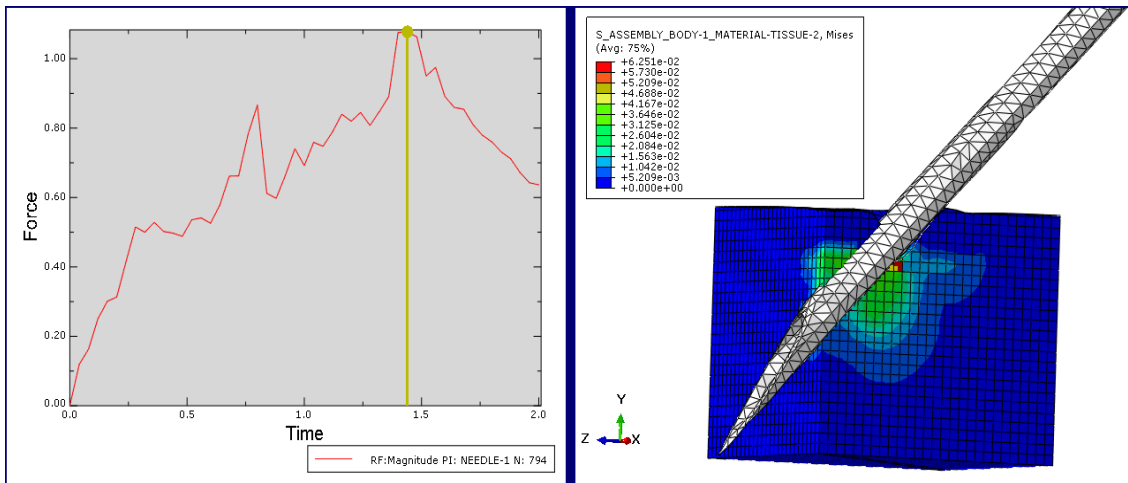


Figure 5.30 - Mises stress distribution of the cardiac muscle at a 45° rotation of the needle about the X-axis during the needle insertion into the cardiac muscle patch

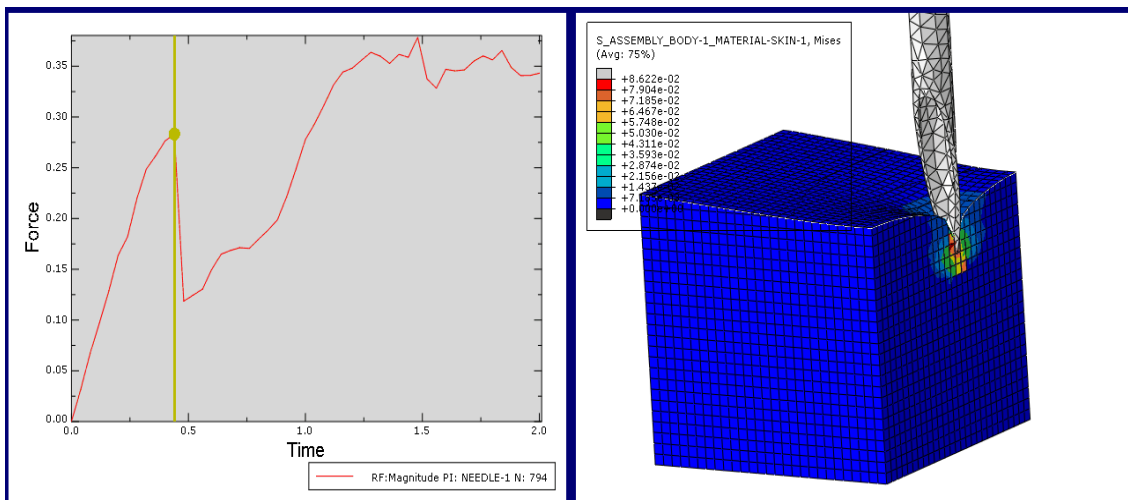


Figure 5.31 - Mises stress distribution of the tender tissue at a 0° rotation (perpendicular) of the needle during the needle insertion into the soft tissue patch



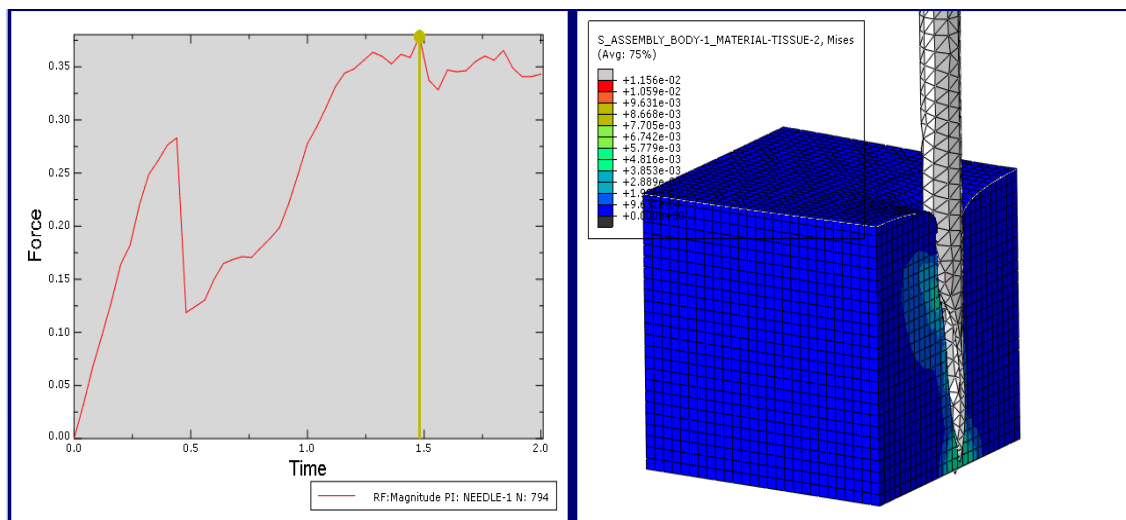


Figure 5.32 - Mises stress distribution of the soft tissue at a 0° rotation (perpendicular) of the needle during the needle insertion into the soft tissue patch

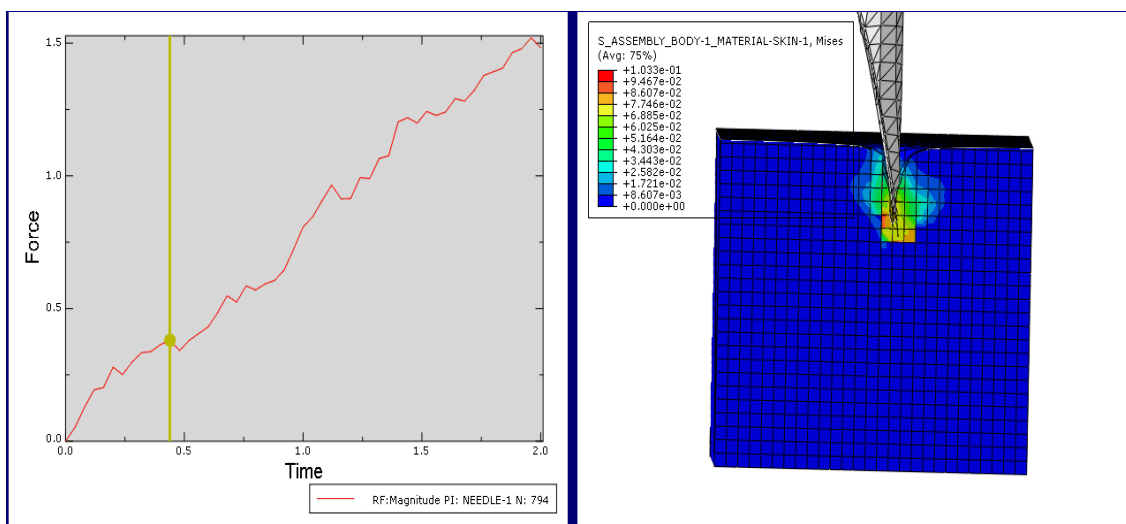


Figure 5.33 - Mises stress distribution of the tender tissue at a 0° rotation (perpendicular) of the needle during the needle insertion into the cardiac muscle patch

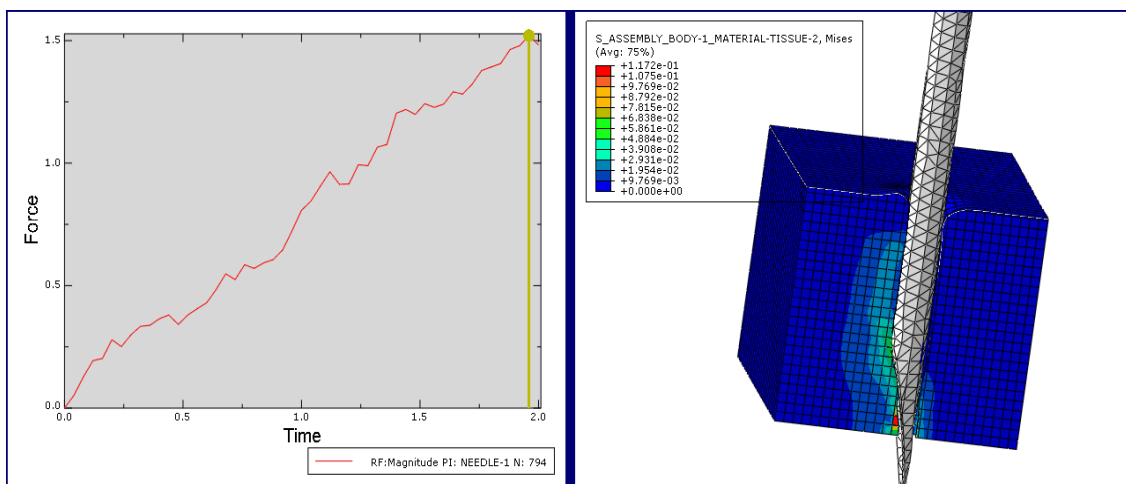


Figure 5.34 - Mises stress distribution of the cardiac muscle at a 0° rotation (perpendicular) of the needle during the needle insertion into the cardiac muscle patch

## 5.4 - Discussion

Two different patches were developed; one representing the soft tissue patch and the other denoting the cardiac muscle patch. Each patch however had two sets of layers comprising of different materials; the tender tissue which occupied the topmost layer of the patch and the rest of the patch was either composed of soft tissue or cardiac muscles for the soft tissue and cardiac muscle patch respectively. Using the Abaqus software and the CEL method of analysis, three sets of simulation results were obtained for each patch and they include: a) graphical representation of the needle insertion forces, b) effects of varying the size of the patch and c) von Mises stress distribution experienced by each layer of the patch. All the simulations were done over a time period of two (2) seconds.

After the simulations were performed for the desired rotations about the specified axis, graphical representations were generated to denote the needle insertion forces with respect to time and each angle of rotation was done about the X and Z-axes.

With regards to the needle insertion forces, the study of the rotation about the Z-axis of the needle during the needle insertion procedure of the soft tissue, it can be noticed that the 30° rotation of the needle during the simulation of the initial dimensions of the soft tissue patch produced relatively the lowest amounts of maximum needle insertion forces. Hence the most suitable degree of rotation of the needle about the Z-axis for the simulation performed since the lower the insertion forces, the lower the tissue deformation as well as the needle displacements and the higher the success rate of the procedure. Also, the perpendicular (0°) needle insertion procedure produced relatively very low maximum needle insertion forces but in reality, it is almost impossible to achieve this since the needle is never inserted into the heart perpendicularly.

Furthermore, considering the needle insertion forces with respect to the X-axis during the needle insertion into the soft tissue patch, it was observed from figure 5.2 that the insertion force dropped sharply towards the end of the simulation for the rotations 15°, 30° and 45° for the initial dimensions of the soft tissue patch simulation. These rotations had reasonably higher insertion forces compared to the other rotations (60° and 0°). A relatively steady drop in the insertion forces were however observed for the rotations with lower needle insertion forces (60° and 0° rotations). The simulations were modelled in a way so as to ensure that the needle perforates the soft tissue to denote the perforation of the atria by the needle and for the simulations with the higher insertion forces, the sharp drop of the insertion forces resulted from the perforation of the soft tissue since there was no frictional force as well as obstructions. Also, it can be noticed that the 60° rotation of the needle about the X-axis during the simulation of the initial dimensions of the soft tissue patch generated the lowest maximum needle insertion forces and hence the most suitable degree of rotation of the needle with regards to the X-axis for the simulation of the soft tissue patch by comparing the results obtained from figures 5.1 and 5.2 in section 5.1.

Considering the needle insertion forces experienced by the cardiac muscle patch, the study of the rotation about the Z-axis of the needle during the needle insertion procedure into the cardiac muscle patch, it can be observed that the 15° rotation of the needle during the simulation of the initial dimensions of the cardiac muscle patch produced relatively very low maximum needle insertion force and hence the most suitable degree of rotation of the needle with regards to this simulation about the Z-axis. It is important however to point out the fact that the 0° rotation generated the lowest maximum needle insertion force but since



that is not realistically achievable (was simulated to give a general overview of its associated needle insertion forces compared to that experienced by the other angles of rotation), the  $15^\circ$  rotation was selected as the most suitable angle of rotation. Again, it is evident from figure 5.3 that the insertion force drops towards the end of the simulation for all the simulations of the rotation about the Z-axis using the initial dimension of the cardiac muscle patch as expected because the simulation was designed to ensure that the needle completely perforates the cardiac muscle patch to demonstrate the perforation of the atria.

In addition, considering the needle insertion forces with respect to the X-axis during the needle insertion into the cardiac muscle patch, it was observed from figure 5.4 that the insertion force dropped sharply towards the end of the simulation for the rotations  $15^\circ$ ,  $30^\circ$  and  $45^\circ$  for the initial dimensions of the cardiac muscle patch simulation due to the higher needle insertion forces generated while the needle insertion forces increased slowly towards the end for the  $60^\circ$  and  $0^\circ$  rotations. Again, it can be deduced that the  $60^\circ$  rotation of the needle about the X-axis during the simulation of the initial dimensions of the cardiac muscle patch generated the lowest maximum needle insertion forces and hence the most suitable degree of rotation of the needle with regards to the X-axis as displayed in figure 5.4 in section 5.1.

The dimensions of the initial patch of the soft tissue and the cardiac muscle were changed but their mechanical properties were kept the same to verify the effect of the size of the patch on the needle insertion forces. Three angles of rotation were used in this simulation (due to time constraint and also, the longer computational time taken to successfully complete one simulation) and they are;  $30^\circ$ ,  $45^\circ$  and  $0^\circ$  about the X and Z-axes. The simulations were again done for both the soft tissue patch and the cardiac muscle patch.

The  $30^\circ$  rotation of the needle about both the Z and X-axes during the simulation of the needle insertion into the new dimension of the soft tissue patch generated similar graphical distribution of the needle insertion force against time. The new dimensions of the soft tissue patch however had lower maximum needle insertion forces which is evident in figures 5.5 and 5.6 in section 5.2. With the rotation about the Z-axis, the highest needle insertion force was 0.383 N for the initial dimensions of the soft tissue patch while the modified dimension had a maximum needle insertion force of 0.337 N. The rotation about the X-axis had the highest needle insertion force to be 0.805 N for the initial dimensions of the soft tissue patch while the modified dimension had a maximum needle insertion force of 0.654 N.

Furthermore, the  $45^\circ$  rotation of the needle about the Z-axis during the simulation of the needle insertion into the new dimension of the soft tissue patch generated slightly varying graphical distribution of the needle insertion force against time. The new dimensions of the soft tissue patch had higher maximum needle insertion forces which is evident in figures 5.7 and 5.8 in section 5.2 due to an increase in the cross-sectional area of the simulation patch along the path of the needle insertion. With the rotation about the Z-axis, the highest needle insertion force was 0.414 N for the initial dimensions of the soft tissue patch while the modified dimension had a maximum needle insertion force of 0.507 N. The rotation about the X-axis had the highest needle insertion force to be 0.534 N for the initial dimensions of the soft tissue patch while the modified dimension had a maximum needle insertion force of 0.549 N. With the  $45^\circ$  rotation about the X-axis after varying the size of the soft tissue patch, the graphical representation in figure 5.8 was relatively similar and the maximum needle insertion forces were approximately the same indicating that the size of the tissue patch

being simulated had little or no effect on the needle insertion forces and the graph for a 45° rotation about the X-axis.

The 0° rotation of the needle about the Z-axis during the simulation of the needle insertion into the new dimension of the soft tissue patch generated similar graphical distribution of the needle insertion force against time as shown in figure 5.9 in section 5.2. The new dimensions of the soft tissue patch however had lower maximum needle insertion forces. With the rotation about the Z-axis, the highest maximum needle insertion force was 0.378 N for the initial dimensions of the soft tissue patch while the modified dimension had a maximum needle insertion force of 0.363 N because the needle insertion for the new dimensions of the patch experienced a lower cross-sectional area compared to the initial dimensions of the patch during the simulation procedure.

The 30° rotation of the needle about the Z axis during the simulation of the needle insertion into the new dimension of the cardiac muscle patch generated relatively similar graphical distribution of the needle insertion force against time while the rotation about the X axis produced a varying graphical distribution of the needle insertion force against time. The new dimensions of the cardiac muscle patch however had lower maximum needle insertion forces which is evident in figures 5.10 and 5.11 in section 5.2 for both axes rotations. With the rotation about the Z-axis, the highest needle insertion force was 1.765 N for the initial dimensions of the cardiac muscle patch while the modified dimension had a maximum needle insertion force of 1.633 N. With the rotation about the X-axis, the highest maximum needle insertion force was 2.038 N for the initial dimensions of the cardiac muscle patch while the modified dimension had a maximum needle insertion force of 1.849 N.

Again, the 45° rotation of the needle about the X-axis during the simulation of the needle insertion into the new dimension of the cardiac muscle patch generated a varying graphical distribution of the needle insertion force against time while the rotation about the Z-axis produced a similar graphical distribution of the needle insertion force against time. The new dimensions of the cardiac muscle patch had higher maximum needle insertion forces about the rotation about the X-axis which is evident in figure 5.13 of section 5.2 compared to the initial dimensions of the patch because the movement of the needle during the simulation was along the side of the patch with the modified dimensions hence resulting in an increase in cross-sectional area and subsequently an increase in the needle insertion forces. The rotation about the Z-axis of the new dimension of the cardiac muscle patch however had a lower maximum needle insertion force compared to the initial dimension of the cardiac muscle patch as seen in figure 5.12 in section 5.2. With the rotation about the Z-axis, the highest maximum needle insertion force was 1.941 N for the initial dimensions of the cardiac muscle patch while the modified dimension had a maximum needle insertion force of 1.780 N. The rotation about the X-axis had the highest maximum needle insertion force to be 1.078 N for the initial dimensions of the cardiac muscle patch while the modified dimension had a maximum needle insertion force of 1.494 N. With the 45° rotation about the X-axis after varying the size of the cardiac muscle patch, the graphical representation in figure 5.13 was largely varied and the maximum needle insertion forces were different as well pointing to the fact that the size of the cardiac muscle patch being simulated had an appreciable effect on the needle insertion forces and the graph for a 45° rotation about the X-axis mainly due to an increase in the surface area of the simulation region of the patch as the needle traversed the cardiac muscle patch.

The 0° rotation of the needle about both the X-axis during the simulation of the needle insertion into the new dimension of the cardiac muscle patch generated similar graphical distribution of the needle insertion force against time. The new dimensions of the cardiac muscle patch however had lower maximum needle insertion forces which can be observed in figure 5.14 in section 5.2. With the 0° rotation, the highest needle insertion force was 1.520 N for the initial dimensions of the cardiac muscle patch while the modified dimension had a maximum needle insertion force of 1.413 N. The same rotation about the Z-axis generated exactly the same set of results because there was no change in the cross-sectional area as well as the direction of the needle insertion. In view of this, only one axis of rotation was displayed in the simulation results.

In a nutshell, it was discovered that the size of the soft tissue and cardiac muscle patch being simulated may/or may not have significant effects on the results based on the angle of rotation as well as the axis of rotation as seen in the earlier results because not all the angles and axes of rotation results in an increase in cross-sectional area and as such generating an increase in needle insertion forces. This is so because in this dissertation, the modification of the dimensions of the patch did not affect all the sides (length, width and height) of the patch but affected just one side (width). An increase in the cross-sectional area will cause a significant increase in the variations of the maximum needle insertion forces as well as the graphical representation.

Based on the mathematical relation between stress and force ( $Stress * Area = Force$ ), the Mises stress distribution images from figures 5.15 to 5.34 were to give an in-depth knowledge and information about the needle insertion force distribution with respect to time. Each needle rotation about the axis had two main sets of Mises stress distribution; one denoting the stress distribution on the tender tissue and the second representing the stress distribution for either the soft tissue or cardiac muscle depending on the type of simulation being performed.

Since the patch used for this simulation had two layers, all the graphical representation of the simulation results of the needle insertion forces against time had at least two spikes or peaks: the first representing the maximum insertion force experienced by the tender tissue and the second represents that experienced by the soft tissue or cardiac muscle depending on the type of needle insertion simulation being conducted. As expected, each figure of the von Mises stress distribution revealed that the maximum von Mises stress experienced by each layer of the patch coincided exactly with either the first or second peak (highest value) of the graphical representation of the needle insertion force against time depending on the layer being displayed (first layer coincided with the first peak while the second layer coincided with the second peak). This indicates the fact that the highest forces were experienced at the highest peaks of the graph for both materials of the assembly (tender tissue and soft tissue or cardiac muscle) during the insertion procedure depending on the location of the needle.

The figures also showed the regions of the tender tissue and soft tissue or cardiac muscle that were likely to experience the highest force or stress during the needle insertion simulation and the colour red indicates the highest experienced stress regions and for almost all the images, the maximum stress was experienced around the regions very close to the needle as the needle traverses the patch in accordance with literature reviews conducted.

## 5.5 - Limitations

In as much as this research work had numerous positives, no mesh convergence study was conducted for the generated finite element mesh of the needle. The mesh convergence study could have had an effect on the simulation results but since it was not done, it will be very difficult to quantify the degree or extent of these variations. Mesh convergence is basically how small the elements need to be in a given finite element model to ensure that the results of the analysis are not influenced by changing the size of the mesh. It is very vital in obtaining accurate results and simulations when using numerical techniques such as finite element analysis.

Also, the cardiac muscles as well as the tissues used in this dissertation were assumed to be elastic materials rather than viscoelastic materials hence they did not possess viscoelastic properties. The human tissues and cardiac muscles however have viscoelastic properties.

Furthermore, only two layers of materials or tissues were considered in this simulation but the human heart is composed of numerous layers of tissues and muscles hence it does not give adequate and accurate information and analysis of the needle insertion into the human atrium.

Finally, due to the long period taken by the individual simulations to complete the needle insertion procedure, a constant time period of two (2) seconds (an increase in the time period of the simulation will give more detailed information about the needle insertion forces) was considered for all simulations and also the size of the patch could not be considered to be very big since the bigger the patch, the longer the time taken to complete the simulation.

## Chapter 6

# Conclusions and future perspectives

This chapter presents the summary of the work done during this dissertation, the conclusions derived after the dissertation based on the results obtained from the simulations as well as the future works and modifications that can be applied to this dissertation to improve the standard of work and also enhance the understanding in this subject area.

### 6.1 - Conclusions

A thorough study of the anatomy of the human heart, right and left atrium, the superior vena cava, inferior vena cava and the atrial septal wall has been performed. A literature review of the finite element models applied to the human atria as well as the atrial wall was also conducted. A thorough study and quantification of the mechanical properties of the different tissues of the human atria were also done.

It is evident that almost all the above reviews done during the literature review and related works used the monodomain equation despite the fact that the bidomain equations accounted for the diverse electrical conductivities of the intracellular and extracellular spaces while the monodomain equations only used one conductivity. This is basically due to the fact that the monodomain and bidomain results were infinitesimally different and also the monodomain requires lower computational cost compared to the bidomain.

In the bid to improve the accuracy of the needle insertion procedure and subsequently enhance the effectiveness and safety of the procedure, a complete review of the researches of needle insertion into soft tissue was conducted. It is however disturbing to note that most of the researches done in this field are still in its early stages and a lot more research is required to be able to ascertain the desired results which would be very close and similar to the actual needle insertion process during the TSP procedure. The current models employed in the reviewed simulations were modelled to be linear and homogeneous which are not the exact properties of the human tissues and cardiac muscles hence more research needs to be conducted to be able to develop real-time, complex models capable of incorporating nonlinearity, inhomogeneity, viscosity and anisotropy.

The mechanical properties of the different atria tissues of the human atria were studied, reviewed and quantified through the effective study of the state-of-the-art research works

done in this field of study. A review and study of the various FEM simulations of needle insertion into the human atria were also conducted to serve as a guide in the development of the new strategy to automatically generate meshes for the constructed patient-specific models of the atria.

Comprehension of the CEL method, the related biomechanical simulations, research into the patient-specific anatomical models, simulations of the atrium as well as the simulation of the needle insertion process into the human atria were done to assist in the development of the new tissue and cardiac muscle patch to be simulated not forgetting the most suitable simulation approach or method to be used during the simulation process.

Finally, after the development of the tissue and cardiac muscle patch and performing the simulations as presented in the results and discussions in the chapter above, it was observed that the size of the tissue and cardiac muscle patch, the angle of rotation of the needle as well as the axis of rotation may have a significant influence on the needle insertion force which is an important factor in determining the success rate of the procedure because a lower insertion force results in very small needle deflection and tissue deformation hence improving the safety and accuracy of the procedure. The von Mises stress distribution analysis also revealed that the highest maximum needle insertion forces experienced by each layer of the soft tissue and cardiac muscle patch coincided exactly with the spikes of their corresponding graphical representation of the needle insertion force against time.

## 6.2 - Future works

The ultimate goal of this field of study is to develop an integrated framework to effectively guide the physician throughout the TSP technique based on the creation of a patient-specific biomechanical model of the atrium. This novel framework is expected to be incorporated into the intra-procedural planning of the expert, with the real-time data acquired from the three-dimensional imaging technique (preferably non-ionization radiation techniques like ultrasound) to successfully guide the transeptal needle position with the optimal puncture site.

This dissertation can be modified by developing the actual anatomical structure of the human atria and simulating the needle insertion procedure using the CEL method as done in chapter 4 of this work in order to obtain more realistic results and simulations.

Furthermore, to attain more accurate and reliable models, patient-specific parameters such as the gender and age, temperature, vascular pressure must be factored into the modelling of the tissue models to increase the efficiency of using the TSP techniques as well as reducing the complications associated with this procedure. Also, it will help decrease the use of ionizing radiation due to the use of volumetric ultrasound imaging.

Another important thing to consider is the mechanical properties of in-vivo soft tissues during the modelling and simulation of soft tissues. In as much as current procedures are able to measure the stress, strain and stiffness in-vivo, more tools need to be developed to measure diverse properties of different organs.

## References

- [1] N. Townsend, M. Nichols, P. Scarborough, and M. Rayner, "Cardiovascular disease in Europe - Epidemiological update 2015," *Eur. Heart J.*, vol. 36, no. 40, pp. 2696-2705, 2015.
- [2] A. Wennevold, "Complications in 1,056 investigations of the left side of the heart," 1950.
- [3] V. C. Babaliaros, J. T. Green, S. Lerakis, M. Lloyd, and P. C. Block, "Emerging Applications for Transseptal Left Heart Catheterization. Old Techniques for New Procedures," *J. Am. Coll. Cardiol.*, vol. 51, no. 22, pp. 2116-2122, 2008.
- [4] M. T. and K. S., "Latest advances in transseptal structural heart interventions - Percutaneous mitral valve repair and left atrial appendage occlusion," *Circ. J.*, vol. 78, no. 8, pp. 1782-1790, 2014.
- [5] N. Abolhassani, R. Patel, and M. Moallem, "Needle insertion into soft tissue: A survey," *Med. Eng. Phys.*, vol. 29, no. 4, pp. 413-431, 2007.
- [6] A. Zivanovic and B. L. Davies, "A robotic system for blood sampling," *IEEE Trans. Inf. Technol. Biomed.*, vol. 4, no. 1, pp. 8-14, Mar. 2000.
- [7] Z. Wei, G. Wan, L. Gardi, G. Mills, D. Downey, and A. Fenster, "Robot-assisted 3D-TRUS guided prostate brachytherapy: System integration and validation," *Med. Phys.*, vol. 31, no. 3, p. 539, 2004.
- [8] P. R. Rizun, P. B. McBeth, D. F. Louw, and G. R. Sutherland, "Robot-Assisted Neurosurgery," *Surg. Innov.*, vol. 11, no. 2, pp. 99-106, Jun. 2004.
- [9] J. H. Youk, E.-K. Kim, M. J. Kim, J. Y. Lee, and K. K. Oh, "Missed Breast Cancers at US-guided Core Needle Biopsy: How to Reduce Them," *RadioGraphics*, vol. 27, no. 1, pp. 79-94, Jan. 2007.
- [10] S. Nath, Z. Chen, N. Yue, S. Trumppore, and R. Peschel, "Dosimetric effects of needle divergence in prostate seed implant using [<sup>sup</sup>125]I and [<sup>sup</sup>103]Pd radioactive seeds," *Med. Phys.*, vol. 27, no. 5, p. 1058, 2000.
- [11] J. J. Carr, P. F. Hemler, P. W. Halford, R. I. Freimanis, R. H. Choplin, and M. Y. M. Chen, "Stereotactic Localization of Breast Lesions: How It Works and Methods to Improve Accuracy," *RadioGraphics*, vol. 21, no. 2, pp. 463-473, Mar. 2001.
- [12] P. L. Roberson, V. Narayana, D. L. McShan, R. J. Winfield, and P. W. McLaughlin, "Source placement error for permanent implant of the prostate," *Med. Phys.*, vol. 24, no. 2, p. 251, 1997.
- [13] H. K. Hussain, J. E. Kingston, P. Domizio, A. J. Norton, and R. H. Reznick, "Imaging-Guided Core Biopsy for the Diagnosis of Malignant Tumors in Pediatric Patients," *Am. J. Roentgenol.*, vol. 176, no. 1, pp. 43-47, Jan. 2001.
- [14] R. Taschereau, J. Pouliot, J. Roy, and D. Tremblay, "Seed misplacement and stabilizing needles in transperineal permanent prostate implants," *Radiother. Oncol.*, vol. 55, no. 1, pp. 59-63, Apr. 2000.
- [15] V. Narayana, P. L. Roberson, R. J. Winfield, M. L. Kessler, and P. W. McLaughlin, "Optimal placement of radioisotopes for permanent prostate implants.," *Radiology*, vol. 199, no. 2, pp. 457-460, May 1996.
- [16] T. K. Rosengart, T. Feldman, M. a. Borger, T. a. Vassiliades, a. M. Gillinov, K. J. Hoercher, A. Vahanian, R. O. Bonow, and W. O'Neill, "Percutaneous and Minimally Invasive Valve Procedures A Scientific Statement From the American Heart Association Council on Cardiovascular Surgery and Anesthesia, Council on Clinical Cardiology, Functional Genomics and Translational Biology Interdisciplina," *Circulation*, vol. 117, pp. 1750-1767, 2008.
- [17] M. J. Earley, "How to perform a transseptal puncture.," *Heart*, vol. 95, no. 1, pp. 85-92, 2009.

- [18] C. Cope, "Technique for transeptal catheterization of the left atrium; preliminary report.," *J. Thorac. Surg.*, vol. 37, no. 4, pp. 482-6, Apr. 1959.
- [19] H. Calkins, J. Brugada, D. L. Packer, R. Cappato, S.-A. Chen, H. J. G. Crijns, R. J. Damiano, D. W. Davies, D. E. Haines, M. Haissaguerre, Y. Iesaka, W. Jackman, P. Jais, H. Kottkamp, K. H. Kuck, B. D. Lindsay, F. E. Marchlinski, P. M. McCarthy, J. L. Mont, F. Morady, K. Nademanee, A. Natale, C. Pappone, E. Prystowsky, A. Raviele, J. N. Ruskin, and R. J. Shemin, "HRS/EHRA/ECAS Expert Consensus Statement on Catheter and Surgical Ablation of Atrial Fibrillation: Recommendations for Personnel, Policy, Procedures and Follow-Up," *Hear. Rhythm*, vol. 4, no. 6, pp. 816-861, 2007.
- [20] G. B. Peckham, a Chrysohou, H. E. Aldridge, and E. D. Wigle, "Combined Percutaneous Retrograde Aortic and Transeptal Left Heart Catheterization.," *Br. Heart J.*, vol. 26, no. 1, pp. 460-8, 1964.
- [21] Z. a Adrouny, D. W. Sutherland, H. E. Griswold, and L. W. Ritzmann, "Complications with transeptal left heart catheterization.," *Am. Heart J.*, vol. 65, pp. 327-333, 1963.
- [22] J. C. Hsu, N. Badhwar, E. P. Gerstenfeld, R. J. Lee, M. C. Mandyam, T. A. Dewland, K. E. Imburgia, K. S. Hoffmayer, V. Vedantham, B. K. Lee, Z. H. Tseng, M. M. Scheinman, J. E. Olgin, and G. M. Marcus, "Randomized trial of conventional transeptal needle versus radiofrequency energy needle puncture for left atrial access (the TRAVERSE-LA study)," *J Am Hear. Assoc*, vol. 2, no. 5, p. e000428, 2013.
- [23] L. Mitchell-Heggs, N. Lellouche, L. Deal, N. Elbaz, B. Hamdaoui, J. B. Castanié, J. L. Dubois-Randé, P. Guéret, and P. Lim, "Transeptal puncture using minimally invasive echocardiography during atrial fibrillation ablation," *Europace*, vol. 12, no. 10, pp. 1435-1438, 2010.
- [24] Y. Wang, Y. M. Xue, P. Mohanty, A. Natale, L. Li, W. F. Wu, C. M. Zhu, H. Liu, G. Q. Zhong, L. G. Zhu, Z. H. Zeng, and D. W. Wang, "Dilator method and needle method for atrial transeptal puncture: A retrospective study from a cohort of 4443 patients," *Europace*, vol. 14, no. 10, pp. 1450-1456, 2012.
- [25] G. K. Feld, J. Tiongson, and G. Oshodi, "Particle formation and risk of embolization during transeptal catheterization: Comparison of standard transeptal needles and a new radiofrequency transeptal needle," *J. Interv. Card. Electrophysiol.*, vol. 30, no. 1, pp. 31-36, 2011.
- [26] L. M. Haegeli, T. Wolber, E. Ercin, L. Altwegg, N. Krasniqi, P. G. Novak, L. D. Sterns, C. B. Brunckhorst, T. F. Lüscher, R. a Leather, and F. Duru, "Double transeptal puncture for catheter ablation of atrial fibrillation: safety of the technique and its use in the outpatient setting.," *Cardiol. Res. Pract.*, vol. 2010, p. 295297, 2010.
- [27] M. P. Smelley, D. P. Shah, I. Weisberg, S. S. Kim, A. C. Lin, J. F. Beshai, M. C. Burke, and B. P. Knight, "Initial experience using a radiofrequency powered transeptal needle," *J. Cardiovasc. Electrophysiol.*, vol. 21, no. 4, pp. 423-427, 2010.
- [28] R. B. Tang, J. Z. Dong, D. Y. Long, R. H. Yu, X. P. Liu, Y. L. Cheng, C. H. Sang, M. Ning, C. X. Jiang, U. M. R. Avula, R. Bai, N. Liu, Y. F. Ruan, X. Du, and C. S. Ma, "Incidence and clinical characteristics of transient ST-T elevation during transeptal catheterization for atrial fibrillation ablation," *Europace*, vol. 17, no. 4, pp. 579-583, 2015.
- [29] Y. Yao, J. Guo, L. Ding, J. Bao, W. Huang, R. Shi, L. Wu, and S. Zhang, "Improved approach to atrial septum puncture: experience in 539 cases.," *Chin. Med. J. (Engl.)*, vol. 125, no. 6, pp. 1179-81, Mar. 2012.
- [30] F. Bayrak, G.-B. Chierchia, M. Namdar, Y. Yazaki, A. Sarkozy, C. de Asmundis, S. A. Muller-Burri, J. Rao, D. Ricciardi, A. Sorgente, and P. Brugada, "Added value of transoesophageal echocardiography during transeptal puncture performed by inexperienced operators," *Europace*, vol. 14, no. 5, pp. 661-665, May 2012.
- [31] Y.-F. Hu, C.-T. Tai, Y.-J. Lin, S.-L. Chang, L.-W. Lo, W. Wongcharoen, A. R. Udyavar, T.-C. Tuan, and S.-A. Chen, "The change in the fluoroscopy-guided transeptal puncture site and difficult punctures in catheter ablation of recurrent atrial fibrillation," *Europace*, vol. 10, no. 3, pp. 276-279, Mar. 2008.
- [32] T. Karagöz, A. Akın, and H. H. Aykan, "NRG™ RF powered transeptal needle: a useful technique for transcatheter atrial septostomy and Fontan fenestration: report of three cases.," *Bosn. J. basic Med. Sci.*, vol. 14, no. 4, pp. 259-62, Oct. 2014.
- [33] P. Wagdi and H. Alkadhi, "Can computer tomography help predict feasibility of transeptal puncture after percutaneous closure of an interatrial septal communication?," *J. Interv. Card.*



- Electrophysiol.*, vol. 34, no. 2, pp. 167-172, Aug. 2012.
- [34] S. Verma, S. Adler, A. Berman, A. Duran, and D. Loar, "Localization of fossa ovalis and Brockenbrough needle prior to left atrial ablation using three-dimensional mapping with EnSite Fusion™," *J. Interv. Card. Electrophysiol.*, vol. 30, no. 1, pp. 37-44, Jan. 2011.
- [35] E. J. Shepherd, S. A. Gall, and S. S. Furniss, "Interatrial septal puncture without the use of fluoroscopy—reducing ionizing radiation in left atrial ablation procedures," *J. Interv. Card. Electrophysiol.*, vol. 22, no. 3, pp. 183-187, Sep. 2008.
- [36] A. G. Unnithan, B. C. Dexter, I. H. Law, and N. H. Von Bergen, "Limiting left-sided catheter dwelling time using 3-D NavX to mark and reaccess the left atrium via prior transeptal puncture site," *J. Interv. Card. Electrophysiol.*, vol. 40, no. 2, pp. 125-128, Aug. 2014.
- [37] N. Pavlović, T. Reichlin, M. Kühne, S. Knecht, S. Osswald, and C. Sticherling, "Fluoroscopy-free recrossing of the interatrial septum during left atrial ablation procedures," *J. Interv. Card. Electrophysiol.*, vol. 41, no. 3, pp. 261-266, Dec. 2014.
- [38] L. Capulzini, G. Paparella, A. Sorgente, C. de Asmundis, G. B. Chierchia, A. Sarkozy, A. Muller-Burri, Y. Yazaki, M. Roos, and P. Brugada, "Feasibility, safety, and outcome of a challenging transeptal puncture facilitated by radiofrequency energy delivery: a prospective single-centre study," *Europace*, vol. 12, no. 5, pp. 662-667, May 2010.
- [39] T.-G. Wu, L.-X. Wang, S.-W. Chen, Z.-Q. Lin, C.-J. Yan, and L.-P. Huang, "Value of Radiographic Esophageal Imaging in Determining an Optimal Atrial Septal Puncture Site for Percutaneous Balloon Mitral Valvuloplasty," *Med. Princ. Pract.*, vol. 17, no. 4, pp. 280-283, 2008.
- [40] S. Gafoor, P. Schulz, L. Heuer, P. Matic, J. Franke, S. Bertog, M. Reinartz, L. Vaskelyte, I. Hofmann, and H. Sievert, "Use of EchoNavigator, a Novel Echocardiography-Fluoroscopy Overlay System, for Transeptal Puncture and Left Atrial Appendage Occlusion," *J. Interv. Cardiol.*, vol. 28, no. 2, pp. 215-217, Apr. 2015.
- [41] Y. Wang, R. K. Chen, B. L. Tai, P. W. McLaughlin, and A. J. Shih, "Optimal needle design for minimal insertion force and bevel length," *Med. Eng. Phys.*, vol. 36, no. 9, pp. 1093-1100, 2014.
- [42] M. D. Angelica and Y. Fong, "Heart Valve Structure and Function in Development and Disease," *October*, vol. 141, no. 4, pp. 520-529, 2008.
- [43] H. B. Grotenhuis and A. De Roos, "Structure and function of the aorta in inherited and congenital heart disease and the role of MRI," *Heart*, vol. 97, no. 1, p. 66-74., 2011.
- [44] S. Standing, *Gray's Anatomy: The Anatomical Basis of Clinical Practice*, vol. 2. 2008.
- [45] R. E. Klabunde, "Cardiovascular Physiology Concepts," *Lippincott Williams & Wilkins*, p. 256, 2004.
- [46] S. P. Nolan, S. H. Dixon, R. D. Fisher, and A. G. Morrow, "The influence of atrial contraction and mitral valve mechanics on ventricular filing. A study of instantaneous mitral valve flow in vivo.," *Am. Heart J.*, vol. 77, no. 6, pp. 784-791, 1969.
- [47] S. P. Pagel, F. Kehl, M. Gare, A. D. Hettrick, R. J. Kersten, and C. D. Wartier, "Mechanical Function of the Left Atrium," *Anesthesiology*, vol. 98, no. 4, pp. 975-994, 2003.
- [48] Y. Ishida, J. S. Meisner, K. Tsujioka, J. I. Gallo, C. Yoran, R. W. Frater, and E. L. Yellin, "Left ventricular filling dynamics: influence of left ventricular relaxation and left atrial pressure.," *Circulation*, vol. 74, no. 1, pp. 187-196, 1986.
- [49] R. H. Anderson, S. Webb, and N. A. Brown, "Clinical anatomy of the atrial septum with reference to its developmental components," *Clinical Anatomy*, vol. 12, no. 5. pp. 362-374, 1999.
- [50] S. Y. Ho and K. P. McCarthy, "Anatomy of the left atrium for interventional electrophysiologists," *PACE - Pacing and Clinical Electrophysiology*, vol. 33, no. 5. pp. 620-627, 2010.
- [51] D. A. Bloomfield, "The Limbic Ledge," *Circulation*, vol. XXXI, pp. 103-108, 1965.
- [52] D. Burkhoff, H. Cohen, C. Brunckhorst, and W. W. O'Neill, "A randomized multicenter clinical study to evaluate the safety and efficacy of the TandemHeart percutaneous ventricular assist device versus conventional therapy with intraaortic balloon pumping for treatment of cardiogenic shock," *Am. Heart J.*, vol. 152, no. 3, 2006.
- [53] "human heart on Scratch." [Online]. Available: <https://scratch.mit.edu/projects/76698852/>. [Accessed: 28-Jun-2017].
- [54] P. Morais, J. L. Vilaça, J. Ector, J. D'hooge, and J. M. R. S. Tavares, "Novel Solutions Applied in Transeptal Puncture: A Systematic Review," *J. Med. Device.*, vol. 11, no. 1, p. 10801, 2017.
- [55] D. Lloyd-Jones, R. J. Adams, T. M. Brown, M. Carnethon, S. Dai, G. De Simone, T. B. Ferguson, E.

- Ford, K. Furie, C. Gillespie, A. Go, K. Greenlund, N. Haase, S. Hailpern, P. M. Ho, V. Howard, B. Kissela, S. Kittner, D. Lackland, L. Lisabeth, A. Marelli, M. M. McDermott, J. Meigs, D. Mozaffarian, M. Mussolino, G. Nichol, V. L. Roger, W. Rosamond, R. Sacco, P. Sorlie, R. Stafford, T. Thom, S. Wasserthiel-Smoller, N. D. Wong, and J. Wylie-Rosett, "Heart disease and stroke statistics-2010 update: A report from the American Heart Association," *Circulation*, vol. 121, no. 7, pp. 46-215, 2010.
- [56] J. Jayender, R. V. Patel, G. F. Michaud, and N. Hata, "Optimal transeptal puncture location for robot-assisted left atrial catheter ablation," *Int. J. Med. Robot. Comput. Assist. Surg.*, vol. 7, no. 2, pp. 193-201, 2011.
- [57] I. Adeniran, D. H. MacIver, C. J. Garratt, J. Ye, J. C. Hancox, and H. Zhang, "Effects of Persistent Atrial Fibrillation-Induced Electrical Remodeling on Atrial Electro-Mechanics - Insights from a 3D Model of the Human Atria," *PLoS One*, vol. 10, no. 11, p. e0142397, 2015.
- [58] P. Kakar, C. J. Boos, and G. Y. H. Lip, "Management of atrial fibrillation," *Vascular Health and Risk Management*, vol. 3, no. 1. pp. 109-116, 2007.
- [59] E. J. Benjamin, P. A. Wolf, R. B. D'Agostino, H. Silbershatz, W. B. Kannel, and D. Levy, "Impact of atrial fibrillation on the risk of death: the Framingham Heart Study.," *Circulation*, vol. 98, no. 10, pp. 946-952, 1998.
- [60] R. H. Falk, "Atrial fibrillation.," *N. Engl. J. Med.*, vol. 344, no. 14, pp. 1067-78, 2001.
- [61] R. H. Falk, "Etiology and complications of atrial fibrillation: insights from pathology studies.," *Am. J. Cardiol.*, vol. 82, no. 8A, p. 10N-17N, 1998.
- [62] P. C. Kahr, I. Piccini, L. Fabritz, B. Greber, H. Schöler, H. H. Scheld, A. Hoffmeier, N. A. Brown, and P. Kirchhof, "Systematic analysis of gene expression differences between left and right atria in different mouse strains and in human atrial tissue," *PLoS One*, vol. 6, no. 10, 2011.
- [63] I. A. Khan, "Atrial stunning: Determinants and cellular mechanisms," *Am. Heart J.*, vol. 145, no. 5, pp. 787-794, 2003.
- [64] I. A. Khan, "Atrial stunning: Basics and clinical considerations," *International Journal of Cardiology*, vol. 92, no. 2-3. pp. 113-128, 2003.
- [65] J. Ausma, M. Wijffels, F. Thoné, L. Wouters, M. Allessie, and M. Borgers, "Structural changes of atrial myocardium due to sustained atrial fibrillation in the goat.," *Circulation*, vol. 96, no. 9, pp. 3157-63, 1997.
- [66] D. R. Van Wagoner, a L. Pond, M. Lamorgese, S. S. Rossie, P. M. McCarthy, and J. M. Nerbonne, "Atrial L-type Ca<sup>2+</sup> currents and human atrial fibrillation.," *Circ. Res.*, vol. 85, no. 5, pp. 428-436, 1999.
- [67] R. F. Bosch, X. Zeng, J. B. Grammer, K. Popovic, C. Mewis, and V. Kühnkamp, "Ionic mechanisms of electrical remodeling in human atrial fibrillation.," *Cardiovasc. Res.*, vol. 44, no. 1, pp. 121-131, 1999.
- [68] a J. Workman, K. a Kane, and a C. Rankin, "The contribution of ionic currents to changes in refractoriness of human atrial myocytes associated with chronic atrial fibrillation.," *Cardiovasc. Res.*, vol. 52, no. 2, pp. 226-235, 2001.
- [69] H. M. W. Van Der Velden and H. J. Jongasma, "Cardiac gap junctions and connexins: Their role in atrial fibrillation and potential as therapeutic targets," *Cardiovascular Research*, vol. 54, no. 2. pp. 270-279, 2002.
- [70] D. Dobrev and U. Ravens, "Remodeling of cardiomyocyte ion channels in human atrial fibrillation.," *Basic Res. Cardiol.*, vol. 98, no. 3, pp. 137-148, 2003.
- [71] E. Wettwer, O. Hála, T. Christ, J. F. Heubach, D. Dobrev, M. Knaut, A. Varró, and U. Ravens, "Role of IK<sub>ur</sub> in controlling action potential shape and contractility in the human atrium: Influence of chronic atrial fibrillation," *Circulation*, vol. 110, no. 16, pp. 2299-2306, 2004.
- [72] M. G. De La Fuente, A. Barana, R. Gómez, I. Amorós, P. Dolz-Gaitón, S. Sacristán, F. Atienza, A. Pita, Á. Pinto, F. Fernández-Avilés, R. Caballero, J. Tamargo, and E. Delpón, "Chronic atrial fibrillation up-regulates  $\beta$ 1-Adrenoceptors affecting repolarizing currents and action potential duration," *Cardiovasc. Res.*, vol. 97, no. 2, pp. 379-388, 2013.
- [73] B. Schwagten, L. Jordaens, M. Rivero-Ayerza, Y. Van Belle, P. Knops, A. Thornton, and T. Szili-Torok, "A randomized comparison of transeptal and transaortic approaches for magnetically guided ablation of left-sided accessory pathways," *PACE - Pacing Clin. Electrophysiol.*, vol. 33, no. 11, pp. 1298-1303, 2010.
- [74] C. E. Ruiz, H. Cohen, R. Del Valle-Fernandez, V. Jelnin, G. Perk, and I. Kronzon, "Closure of prosthetic paravalvular leaks: A long way to go," *European Heart Journal, Supplement*, vol. 12,

- no. SUPPL. E. 2010.
- [75] A. Vahanian and I. F. Palacios, "Percutaneous Approaches to Valvular Disease," *Circulation*, vol. 109, no. 13, pp. 1572-1579, 2004.
- [76] C. Cope, "Technique for transseptal catheterization of the left atrium; preliminary report.," *J. Thorac. Surg.*, 1959.
- [77] Y. Yao, L. Ding, W. Chen, J. Guo, J. Bao, R. Shi, W. Huang, S. Zhang, and T. Wong, "The training and learning process of transseptal puncture using a modified technique.," *Eur. Eur. pacing, arrhythmias, Card. Electrophysiol. J. Work. groups Card. pacing, arrhythmias, Card. Cell. Electrophysiol. Eur. Soc. Cardiol.*, vol. 15, no. 12, pp. 1784-1790, 2013.
- [78] S. Fromentin, J. F. Sarrazin, J. Champagne, I. Nault, F. Philippon, F. Molin, L. Blier, and G. O'Hara, "Prospective comparison between conventional transseptal puncture and transseptal needle puncture with radiofrequency energy," *J. Interv. Card. Electrophysiol.*, vol. 31, no. 3, pp. 237-242, 2011.
- [79] L. J. Sweeney and G. C. Rosenquist, "The normal anatomy of the atrial septum in the human heart," *Am. Heart J.*, vol. 98, no. 2, pp. 194-199, 1979.
- [80] J. Fish, *A First Course in Finite Elements*. USA: John Wiley and Sons Ltd, 2007.
- [81] D. Systemes, *Abaqus Theory Guide 6.14*. Dassault Systèmes Simulia Corp., Providence, RI, USA, 2014.
- [82] J. Votano, M. Parham, and L. Hall, *The Finite Element Method and Applications in Engineering Using ANSYS*. Springer, 2004.
- [83] T. Stolarski, Y. Nakasone, and S. Yoshimoto, *Engineering Analysis With ANSYS Software*. Elsevier Butterworth-Heinemann LinacreHouse, JordanHill,Oxford, 2006.
- [84] G. Qiu, S. Henke, and J. Grabe, "Applications of Coupled Eulerian-Lagrangian Method to Geotechnical Problems with Large Deformations," *SIMULIA Cust. Conf.*, no. 2001, pp. 1-16, 2009.
- [85] G. Qiu, S. Henke, and J. Grabe, "Application of a Coupled Eulerian-Lagrangian approach on geomechanical problems involving large deformations," *Comput. Geotech.*, vol. 38, no. 1, pp. 30-39, 2011.
- [86] A. Anup, "A coupled Eulerian-Lagrangian extended finite element formulation for moving interface problems and damage transport in hyperelastic media," Vanderbilt University, 2014.
- [87] A. Sillem, "Feasibility study of a tire hydroplaning simulation in a monolithic finite element code using a coupled Eulerian-Lagrangian method," Delft University of Technology, 2008.
- [88] R. Babar and V. Katkar, "Simulation of fuel tank slosh test - Coupled Eulerian-Lagrangian Approach," *Tata Technol. TATA Mot. Ltd. Pimpri, Pune*, vol. 91-20-6613, pp. 1-10, 2010.
- [89] D. Harrild and C. Henriquez, "A computer model of normal conduction in the human atria.," *Circ. Res.*, vol. 87, no. 7, pp. E25-E36, 2000.
- [90] G. Seemann, C. Höper, F. B. Sachse, O. Dössel, A. V Holden, and H. Zhang, "Heterogeneous three-dimensional anatomical and electrophysiological model of human atria.," *Philos. Trans. A. Math. Phys. Eng. Sci.*, vol. 364, no. 1843, pp. 1465-1481, 2006.
- [91] S. Tungjitkusolmun, E. J. Woo, H. Cao, J. Z. Tsai, V. R. Vorperian, and J. G. Webster, "Thermal-electrical finite element modelling for radio frequency cardiac ablation: effects of changes in myocardial properties.," *Med. Biol. Eng. Comput.*, vol. 38, no. 5, pp. 562-568, 2000.
- [92] D. Harrild and C. Henriquez, "A computer model of normal conduction in the human atria," *Circ. Res.*, 2000.
- [93] H. M. Wang, H. Gao, X. Y. Luo, C. Berry, B. E. Griffith, R. W. Ogden, and T. J. Wang, "Structure-based finite strain modelling of the human left ventricle in diastole," *Int. j. numer. method. biomed. eng.*, vol. 29, no. 1, pp. 83-103, 2013.
- [94] H. Wen, E. Bennett, N. Epstein, and J. Plehn, "Magnetic resonance imaging assessment of myocardial elastic modulus and viscosity using displacement imaging and phase-contrast velocity mapping," *Magn. Reson. Med.*, vol. 54, no. 3, pp. 538-548, 2005.
- [95] K. Spiegel, W. Schiller, T. Schmidt, A. Welz, D. Liepsch, and H. Oertel, "Numerical Simulation of the Left Ventricle and Atrium as Reference for Pathological Hearts," in *Biomechanics*, 2007.
- [96] E. Soudah, R. Rossi, S. Idelsohn, and E. O'ate, "A reduced-order model based on the coupled 1D-3D finite element simulations for an efficient analysis of hemodynamics problems," *Comput. Mech.*, vol. 54, no. 4, pp. 1013-1022, 2014.
- [97] M. W. Krueger, G. Seemann, K. Rhode, D. U. J. Keller, C. Schilling, A. Arujuna, J. Gill, M. D. O'Neill, R. Razavi, and O. Dossel, "Personalization of atrial anatomy and electrophysiology as a basis for clinical modeling of radio-frequency ablation of atrial fibrillation," *IEEE Trans. Med.*

- Imaging*, vol. 32, no. 1, pp. 73-84, 2013.
- [98] N. Smith, a. de Vecchi, M. McCormick, D. Nordsletten, O. Camara, a. F. Frangi, H. Delingette, M. Sermesant, J. Relan, N. Ayache, M. W. Krueger, W. H. W. Schulze, R. Hose, I. Valverde, P. Beerbaum, C. Staicu, M. Siebes, J. Spaan, P. Hunter, J. Weese, H. Lehmann, D. Chapelle, and R. Rezavi, "euHeart: personalized and integrated cardiac care using patient-specific cardiovascular modelling," *Interface Focus*, vol. 1, no. 3, pp. 349-364, 2011.
- [99] C. Chnafa, S. Mendez, F. Nicoud, R. Moreno, S. Nottin, and I. Schuster, "Image-based patient-specific simulation: a computational modelling of the human left heart haemodynamics," *\Cmbbe*, vol. 15(supp1), no. May 2015, pp. 74-75, 2012.
- [100] B. Baillargeon, N. Rebelo, D. D. Fox, R. L. Taylor, and E. Kuhl, "The living heart project: A robust and integrative simulator for human heart function," *Eur. J. Mech. A/Solids*, vol. 48, no. 1, pp. 38-47, 2014.
- [101] T. Mansi, I. Voigt, E. A. Mengue, R. Ionasec, B. Georgescu, T. Noack, J. Seeburger, and D. Comaniciu, "Towards patient-specific finite-element simulation of mitralclip procedure," in *Lecture Notes in Computer Science (including subseries Lecture Notes in Artificial Intelligence and Lecture Notes in Bioinformatics)*, 2011, vol. 6891 LNCS, no. PART 1, pp. 452-459.
- [102] M. Stevanella, F. Maffessanti, C. A. Conti, E. Votta, A. Arnoldi, M. Lombardi, O. Parodi, E. G. Caiani, and A. Redaelli, "Mitral Valve Patient-Specific Finite Element Modeling from Cardiac MRI: Application to an Annuloplasty Procedure," *Cardiovasc. Eng. Technol.*, vol. 2, no. 2, pp. 66-76, 2011.
- [103] Q. Wang, E. Sirois, and W. Sun, "Patient-specific modeling of biomechanical interaction in transcatheter aortic valve deployment," *J. Biomech.*, vol. 45, no. 11, pp. 1965-1971, 2012.
- [104] S. Morganti, M. Conti, M. Aiello, A. Valentini, A. Mazzola, A. Reali, and F. Auricchio, "Simulation of transcatheter aortic valve implantation through patient-specific finite element analysis: Two clinical cases," *J. Biomech.*, vol. 47, no. 11, pp. 2547-2555, 2014.
- [105] A. Daoudi, S. Mahmoudi, and M. Chikh, "Automatic segmentation of the left atrium on CT images," , *O. Camara, T. Mansi, M. Pop, ...*, 2014.
- [106] A. Haak, B. Ren, H. W. Mulder, G. Vegas-S?nchez-Ferrero, G. van Burken, A. F. W. van der Steen, M. van Stralen, J. P. W. Pluim, T. van Walsum, and J. G. Bosch, "Improved segmentation of multiple cavities of the heart in wideview 3-D transesophageal echocardiograms," *Ultrasound Med. Biol.*, vol. 41, no. 7, pp. 1991-2000, 2015.
- [107] N. Almeida, D. Barbosa, B. Heyde, R. O. Mada, D. Friboulet, O. Bernard, E. Samset, and J. D'hooge, "Semi-automatic left-atrial segmentation from volumetric ultrasound using B-spline explicit active surfaces," *IEEE Int. Ultrason. Symp. Proc.*, vol. 978-1-4799, pp. 612-615, 2014.
- [108] D. Barbosa, T. Dietenbeck, J. Schaerer, J. D'hooge, D. Friboulet, and O. Bernard, "B-spline explicit active surfaces: an efficient framework for real-time 3-D region-based segmentation.," *IEEE Trans. Image Process.*, vol. 21, no. 1, pp. 241-51, 2012.
- [109] S. Queirós, D. Barbosa, B. Heyde, P. Morais, J. L. Vilaça, D. Friboulet, O. Bernard, and J. D'hooge, "Fast automatic myocardial segmentation in 4D cine CMR datasets," *Med. Image Anal.*, vol. 18, no. 7, pp. 1115-1131, 2014.
- [110] Y. Zheng, A. Barbu, B. Georgescu, M. Scheuering, and D. Comaniciu, "Four-chamber heart modeling and automatic segmentation for 3-D cardiac CT volumes using marginal space learning and steerable features," *IEEE Trans. Med. Imaging*, vol. 27, no. 11, pp. 1668-1681, 2008.
- [111] J. Margeta, K. McLeod, A. Criminisi, and N. Ayache, "Decision Forests for Segmentation of the Left Atrium from 3D MRI," Springer Berlin Heidelberg, 2014, pp. 49-56.
- [112] M. A. Zuluaga, M. J. Cardoso, M. Modat, and S. Ourselin, "Multi-atlas Propagation Whole Heart Segmentation from MRI and CTA Using a Local Normalised Correlation Coefficient Criterion," Springer Berlin Heidelberg, 2013, pp. 174-181.
- [113] H. A. Kirişli, M. Schaap, S. Klein, S. L. Papadopoulou, M. Bonardi, C. H. Chen, A. C. Weustink, N. R. Mollet, E. J. Vonken, R. J. van der Geest, T. van Walsum, and W. J. Niessen, "Evaluation of a multi-atlas based method for segmentation of cardiac CTA data: a large-scale, multicenter, and multivendor study," *Med. Phys.*, vol. 37, no. 12, pp. 6279-6291, 2010.
- [114] O. Ecabert, J. Peters, M. J. Walker, T. Ivanc, C. Lorenz, J. von Berg, J. Lessick, M. Vembar, and J. Weese, "Segmentation of the heart and great vessels in CT images using a model-based adaptation framework," *Med. Image Anal.*, vol. 15, no. 6, pp. 863-876, 2011.
- [115] K. Cleary and T. M. Peters, "Image-Guided Interventions: Technology Review and Clinical Applications," *Annu. Rev. Biomed. Eng.*, vol. 12, no. 1, pp. 119-142, 2010.

- [116] M. Jeevan, R. Jebaraj, and R. Krishnakumar, "In-vitro validation of image guided surgery system with 3d pre-operative visualization for atrial transseptal puncture," in *Proceedings of the International Conference on Information Visualisation*, 2014, pp. 342-345.
- [117] C. R. Hatt, A. K. Jain, V. Parthasarathy, A. Lang, and A. N. Raval, "MRI-3D ultrasound-X-ray image fusion with electromagnetic tracking for transendocardial therapeutic injections: In-vitro validation and in-vivo feasibility," *Comput. Med. Imaging Graph.*, vol. 37, no. 2, pp. 162-173, 2013.
- [118] P. Lang, P. Seslija, D. Bainbridge, G. M. Guiraudon, D. L. Jones, M. W. Chu, D. W. Holdsworth, and T. M. Peters, "Accuracy assessment of fluoroscopy-transesophageal echocardiography registration BT - Medical Imaging 2011: Visualization, Image-Guided Procedures, and Modeling, February 13, 2011 - February 15, 2011," vol. 7964, p. The Society of Photo-Optical Instrumentation Engin, 2011.
- [119] R. J. Housden, M. Basra, Y. Ma, A. P. King, R. Bullens, N. Child, J. Gill, C. A. Rinaldi, V. Parish, and K. S. Rhode, "Three-modality registration for guidance of minimally invasive cardiac interventions," *Lect. Notes Comput. Sci. (including Subser. Lect. Notes Artif. Intell. Lect. Notes Bioinformatics)*, vol. 7945 LNCS, pp. 158-165, 2013.
- [120] X. Huang, J. Moore, G. Guiraudon, D. L. Jones, D. Bainbridge, J. Ren, and T. M. Peters, "Dynamic 2D ultrasound and 3D CT image registration of the beating heart," *IEEE Trans. Med. Imaging*, vol. 28, no. 8, pp. 1179-1189, 2009.
- [121] G. Gao, G. Penney, Y. Ma, N. Gogin, P. Cathier, A. Arujuna, G. Morton, D. Caulfield, J. Gill, C. Aldo Rinaldi, J. Hancock, S. Redwood, M. Thomas, R. Razavi, G. Gijbsbers, and K. Rhode, "Registration of 3D trans-esophageal echocardiography to X-ray fluoroscopy using image-based probe tracking," *Med. Image Anal.*, vol. 16, no. 1, pp. 38-49, 2012.
- [122] P. Lang, M. Rajchl, F. Li, and T. M. Peters, "Towards model-enhanced real-time ultrasound guided cardiac interventions," in *Proceedings - 2011 International Conference on Intelligent Computation and Bio-Medical Instrumentation, ICBMI 2011*, 2011, pp. 89-92.
- [123] S. Grbic, C. Gesell, R. Ionasec, and M. John, "Model-based fusion of ct and non-contrasted 3d c-arm ct: application to transcatheter valve therapies," *IEEE*, vol. 978-1-4577, pp. 1192-1195, 2012.
- [124] R. Liao, S. Miao, and Y. Zheng, "Automatic and efficient contrast-based 2-D/3-D fusion for transcatheter aortic valve implantation (TAVI)," *Comput. Med. Imaging Graph.*, vol. 37, no. 2, pp. 150-161, 2013.
- [125] A. Brost, A. Wimmer, R. Liao, J. Hornegger, and N. Strobel, "Catheter tracking: Filter-based vs. learning-based," in *Lecture Notes in Computer Science (including subseries Lecture Notes in Artificial Intelligence and Lecture Notes in Bioinformatics)*, 2010, vol. 6376 LNCS, pp. 293-302.
- [126] S. De Buck, J. Ector, a La Gerche, F. Maes, and H. Heidbuchel, "Toward image-based catheter tip tracking for treatment of atrial fibrillation," *CI2BM09 - MICCAI Work. Cardiovasc. Interv. Imaging Biophys. Model.*, 2009.
- [127] X. Wu, J. Housden, Y. Ma, B. Razavi, K. Rhode, and D. Rueckert, "Fast catheter segmentation from echocardiographic sequences based on segmentation from corresponding X-ray fluoroscopy for cardiac catheterization interventions," *IEEE Trans. Med. Imaging*, vol. 34, no. 4, pp. 861-876, 2015.
- [128] C. B. Moyer, P. T. Norton, J. D. Ferguson, and J. W. Holmes, "Changes in Global and Regional Mechanics Due to Atrial Fibrillation: Insights from a Coupled Finite-Element and Circulation Model," *Ann. Biomed. Eng.*, vol. 43, no. 7, pp. 1600-1613, 2015.
- [129] S. Maas, B. Ellis, and G. Ateshian, "FEBio: finite elements for biomechanics," *J. Biomech. Eng.*, vol. 134, no. 11005-4, pp. 1-10, 2012.
- [130] C. B. Moyer, P. A. Helm, C. J. Clarke, L. P. Budge, C. M. Kramer, J. D. Ferguson, P. T. Norton, and J. W. Holmes, "Wall-motion based analysis of global and regional left atrial mechanics," *IEEE Trans. Med. Imaging*, vol. 32, no. 10, pp. 1765-1776, 2013.
- [131] S. Y. Ho, R. H. Anderson, and D. Sánchez-Quintana, "Atrial structure and fibres: Morphologic bases of atrial conduction," *Cardiovasc. Res.*, vol. 54, no. 2, pp. 325-336, 2002.
- [132] J. Zhao, T. D. Butters, H. Zhang, I. J. Legrice, G. B. Sands, and B. H. Smaill, "Image-based model of atrial anatomy and electrical activation: A computational platform for investigating atrial arrhythmia," *IEEE Trans. Med. Imaging*, vol. 32, no. 1, pp. 18-27, 2013.
- [133] S. Y. Ho, D. Sanchez-Quintana, J. A. Cabrera, and R. H. Anderson, "Anatomy of the Left Atrium: Implications for Radiofrequency Ablation of Atrial Fibrillation," *J Cardiovasc Electrophysiol*, vol.

- 10, pp. 1525-1533, 1999.
- [134] D. Schwartzman, J. Lacomis, and W. G. Wigginton, "Characterization of left atrium and distal pulmonary vein morphology using multidimensional computed tomography," *J. Am. Coll. Cardiol.*, vol. 41, no. 8, pp. 1349-1357, 2003.
- [135] A. Guyton, A. Lindsey, and B. Abernathy, "Venous return at various right atrial pressures and the normal venous return curve," *Am. J.*, 1957.
- [136] M. Raghavan, B. Ma, and M. Fillinger, "Non-invasive determination of zero-pressure geometry of arterial aneurysms," *Ann. Biomed. Eng.*, 2006.
- [137] J. Alexander, K. Sunagawa, and N. Chang, "Instantaneous pressure-volume relation of the ejecting canine left atrium.," *Circ. Res.*, 1987.
- [138] C. Tobón, C. A. Ruiz-Villa, E. Heidenreich, L. Romero, F. Hornero, and J. Saiz, "A Three-Dimensional Human Atrial Model with Fiber Orientation. Electrograms and Arrhythmic Activation Patterns Relationship," *PLoS One*, vol. 8, no. 2, 2013.
- [139] S. Y. Ho and D. Sánchez-Quintana, "The importance of atrial structure and fibers," *Clin. Anat.*, vol. 22, no. 1, pp. 52-63, 2009.
- [140] G. I. Cohen, M. White, R. A. Sochowski, A. L. Klein, P. D. Bridge, W. J. Stewart, and K. L. Chan, "Reference values for normal adult transesophageal echocardiographic measurements," *J. Am. Soc. Echocardiogr.*, vol. 8, no. 3, pp. 221-230, 1995.
- [141] a Nygren, C. Fiset, L. Firek, J. W. Clark, D. S. Lindblad, R. B. Clark, and W. R. Giles, "Mathematical model of an adult human atrial cell: the role of K<sup>+</sup> currents in repolarization.," *Circ. Res.*, vol. 82, no. 1, pp. 63-81, 1998.
- [142] J. Feng, L. Yue, Z. Wang, and S. Nattel, "Ionic mechanisms of regional action potential heterogeneity in the canine right atrium.," *Circ. Res.*, vol. 83, no. 5, pp. 541-551, 1998.
- [143] R. Wilders, M. Wagner, D. Golod, R. Kumar, and Y. Wang, "Effects of anisotropy on the development of cardiac arrhythmias associated with focal activity," *Pflügers Arch.*, 2000.
- [144] D. M. Harrild, C. S. Henriquez, and T. H. Atria, "CS, "A Computer Model of Normal Conduction," *Hum. Atria*," *Circ Res*, vol 87, pp. 25-36, 2000.
- [145] C. Corrado, J. Whitaker, H. Chubb, S. William, M. Wright, J. Gill, M. O'Neill, and S. Niederer, "Personalized models of human atrial electrophysiology derived from endocardial electrograms.," *IEEE Trans. Biomed. Eng.*, vol. 9294, no. c, pp. 1-8, 2016.
- [146] M. Potse, B. Dubé, J. Richer, and A. Vinet, "A comparison of monodomain and bidomain reaction-diffusion models for action potential propagation in the human heart," *IEEE Trans.*, 2006.
- [147] M. Ethier and Y. Bourgault, "Semi-implicit time-discretization schemes for the bidomain model," *SIAM J. Numer. Anal.*, 2008.
- [148] R. Aliev and A. Panfilov, "A simple two-variable model of cardiac excitation," *Chaos, Solitons & Fractals*, 1996.
- [149] C. Mitchell and D. Schaeffer, "A two-current model for the dynamics of cardiac membrane," *Bull. Math. Biol.*, 2003.
- [150] D. Schaeffer, J. Cain, D. Gauthier, and S. Kalb, "An ionically based mapping model with memory for cardiac restitution," *Bull. Math.*, 2007.
- [151] S. P. DiMaio and S. E. Salcudean, "Needle insertion modeling and simulation," *IEEE Trans. Robot. Autom.*, vol. 2, pp. 2098-2105, 2003.
- [152] L. Kohn, J. Corrigan, and M. Donaldson, *To err is human: building a safer health system*. 2000.
- [153] B. Maurin, L. Barbe, B. Bayle, and P. Zanne, "In vivo study of forces during needle insertions," *Proc.*, 2004.
- [154] A. E. Kerdok, S. M. Cotin, M. P. Ottensmeyer, A. M. Galea, R. D. Howe, and S. L. Dawson, "Truth cube: establishing physical standards for soft tissue simulation.," *Med. Image Anal.*, vol. 7, no. 3, pp. 283-91, Sep. 2003.
- [155] S. DiMaio and S. Salcudean, "Interactive simulation of needle insertion models," *IEEE Trans. Biomed.*, 2005.
- [156] S. P. DiMaio and S. E. Salcudean, "Needle Steering and Motion Planning in Soft Tissues," *IEEE Trans. Biomed. Eng.*, vol. 52, no. 6, pp. 965-974, Jun. 2005.
- [157] S. P. DiMaio and S. E. Salcudean, "Needle steering and model-based trajectory planning," *Med. Image Comput. Comput. Interv. - Miccai 2003, Pt 1*, vol. 2878, pp. 33-40, 2003.
- [158] R. Alterovitz, J. Pouliot, R. Taschereau, I.-C. J. Hsu, and K. Goldberg, "Simulating needle insertion and radioactive seed implantation for prostate brachytherapy.," *Stud. Health Technol.*

- Inform.*, vol. 94, pp. 19-25, 2003.
- [159] R. Alterovitz, K. Goldberg, and J. Pouliot, "Needle insertion and radioactive seed implantation in human tissues: Simulation and sensitivity analysis," *IEEE*, vol. 0-7803-773, pp. 1793-1799, 2003.
- [160] R. Alterovitz and K. Goldberg, "Comparing algorithms for soft tissue deformation: accuracy metrics and benchmarks," *Rapp. Tech. UC Berkeley Alpha Lab*, 2002.
- [161] T. A. Krouskop, T. M. Wheeler, F. Kallel, B. S. Garra, and T. Hall, "Elastic moduli of breast and prostate tissues under compression.," *Ultrason. Imaging*, vol. 20, no. 4, pp. 260-74, Oct. 1998.
- [162] Y. Fung, *Biomechanics: mechanical properties of living tissues*. 2013.
- [163] K. Parker, S. Huang, and R. Musulin, "Tissue response to mechanical vibrations for 'sonoelasticity imaging,'" *Ultrasound Med.*, 1990.
- [164] A. Nava, E. Mazza, F. Kleinermann, and N. Avis, "Determination of the mechanical properties of soft human tissues through aspiration experiments," *MICCAI*, vol. LNCS 2878, pp. 222-229, 2003.
- [165] S. P. Dimaio, "Modelling, Simulation and Planning of Needle Motion in Soft Tissues," the university of british columbia, 2003.
- [166] P. S. Calhoun, B. S. Kuszyk, D. G. Heath, J. C. Carley, and E. K. Fishman, "Volume rendering of peripancreatic vasculature using biphasic spiral CT data," *Acad. Radiol.*, vol. 3, no. 12, p. 1057, 1996.
- [167] W. McAlpine, *Heart and coronary arteries: an anatomical atlas for clinical diagnosis, radiological investigation, and surgical treatment*. 2012.
- [168] C. Stöllberger, G. Ernst, E. Bonner, J. Finsterer, and J. Slany, "Left atrial appendage morphology: comparison of transesophageal images and postmortem casts.," *Z. Kardiol.*, vol. 92, no. 4, pp. 303-8, Apr. 2003.
- [169] D. Sánchez-Quintana, J. A. Cabrera, V. Climent, J. Farré, M. C. de Mendonça, and S. Y. Ho, "Anatomic relations between the esophagus and left atrium and relevance for ablation of atrial fibrillation.," *Circulation*, vol. 112, no. 10, pp. 1400-5, Sep. 2005.
- [170] T. R. Kucklick, "The medical device R & D handbook," *Med. device R&D Handb.*, p. xix, 482 [6] of plates, 2013.
- [171] M. Towler, W. McGregor, and G. Rodeheaver, "Influence of cutting edge configuration on surgical needle penetration forces," *J.*, 1988.
- [172] J. Joslin, "Blood collection techniques in exotic small mammals," *J. Exot. Pet Med.*, 2009.
- [173] "Hypodermic needle," 1953.
- [174] A. Okamura, C. Simone, and M. Leary, "Force modeling for needle insertion into soft tissue," , *IEEE Trans.*, 2004.
- [175] D. van Gerwen and J. Dankelman, "Needle-tissue interaction forces-A survey of experimental data," *Med. Eng.*, 2012.
- [176] T. Podder, D. Clark, J. Sherman, and D. Fuller, "Effects of tip geometry of surgical needles: an assessment of force and deflection," *IFMBE*, 2005.
- [177] T. Podder, J. Sherman, D. Rubens, E. Messing, J. Strang, W.-S. Ng, and Y. Yu, "Methods for prostate stabilization during transperineal LDR brachytherapy," *Phys. Med. Biol.*, vol. 53, no. 6, pp. 1563-1579, Mar. 2008.
- [178] L. Arendt-Nielsen, H. Egekvist, and P. Bjerring, "Pain following controlled cutaneous insertion of needles with different diameters," *Somatosens. Mot. Res.*, vol. 23, no. 1-2, pp. 37-43, Jan. 2006.
- [179] N. Abolhassani, R. V. Patel, and F. Ayazi, "Minimization of needle deflection in robot-assisted percutaneous therapy," *Int. J. Med. Robot. Comput. Assist. Surg.*, vol. 3, no. 2, pp. 140-148, Jun. 2007.
- [180] M. D. O'Leary, C. Simone, T. Washio, K. Yoshinaka, and A. M. Okamura, "Robotic needle insertion: effects of friction and needle geometry," *IEEE*, vol. 0-7803-773, pp. 1774-1780, 2003.
- [181] S. Misra, K. Reed, and A. Douglas, "Needle-tissue interaction forces for bevel-tip steerable needles," *IEEE-EMBS Int. Conf. Biomed. Robot. Biomechatronics*, vol. 978-1-4244, pp. 224-231, 2008.
- [182] "Layers of the Heart - Anatomy and Pathology | Kenhub." [Online]. Available: <https://www.kenhub.com/en/library/anatomy/layers-of-the-heart>. [Accessed: 18-Apr-2017].
- [183] "Cardiac Muscle Tissue | Interactive Anatomy Guide." [Online]. Available: [http://www.innerbody.com/image\\_musc01/musc71.html](http://www.innerbody.com/image_musc01/musc71.html). [Accessed: 18-Apr-2017].
- [184] M. J. Oldfield, D. Dini, G. Giordano, and F. Rodriguez Y Baena, "Detailed finite element modelling of deep needle insertions into a soft tissue phantom using a cohesive approach,"

- Comput. Methods Biomech. Biomed. Engin.*, vol. 16, no. 5, pp. 530-43, 2013.
- [185] I. V. Ogneva, D. V. Lebedev, and B. S. Shenkman, "Transversal stiffness and young's modulus of single fibers from rat soleus muscle probed by atomic force microscopy," *Biophys. J.*, vol. 98, no. 3, pp. 418-424, 2010.
- [186] J. T. Hing, A. D. Brooks, and J. P. Desai, "Reality-based needle insertion simulation for haptic feedback in prostate brachytherapy," *Proc. - IEEE Int. Conf. Robot. Autom.*, vol. 2006, no. May, pp. 619-624, 2006.